

**Water in the Earth's Interior:**  
Thermodynamics and kinetics of hydrogen  
incorporation in olivine and wadsleyite

Von der Fakultät für Biologie, Chemie und Geowissenschaften der  
Universität Bayreuth

Zur Erlangung der Würde eines  
**Doktors der Naturwissenschaften**  
**-Dr.rer.nat.-**

genehmigte Dissertation

vorgelegt von

**Sylvie Demouchy**  
Aus Marseille (Frankreich)



Die vorliegende Arbeit wurde von Oktober 2000 bis Juli 2004 am Bayerisches Geoinstitut der Universität Bayreuth unter Leitung von Prof. Dr. Steve Mackwell und Prof. Dr. Hans Keppler angefertigt.

Vollständiger Abdruck der von der Fakultät für Biologie, Chemie und Geowissenschaften der Universität Bayreuth genehmigten Dissertation zur Erlangung des akademischen Grades eines Doktors der Naturwissenschaften (Dr. Rer. Nat.)

**Datum der Einreichung der Arbeit am 01.06.2004**

**Datum des wissenschaftlichen Kolloquium am 27.07. 2004**

*Prüfungsausschuss*

Vorsitzender Prof. Dr. K. Bitzer  
Erstgutachter Prof. Dr. S. Mackwell  
Zweitgutachter Prof. Dr. F. Seifert  
Prof. Dr. P. Morys  
PD. Dr. F. Langenhorst

Amtierender Dekan: Prof. Dr. O. Meyer



# **Water in the Earth's Interior:**

## Thermodynamics and kinetics of hydrogen incorporation in olivine and wadsleyite

Von der Fakultät für Biologie, Chemie und Geowissenschaften der  
Universität Bayreuth

Zur Erlangung der Würde eines  
**Doktors der Naturwissenschaften**  
**-Dr.rer.nat.-**

genehmigte Dissertation

vorgelegt von

**Sylvie Demouchy**  
Aus Marseille (Frankreich)

Bayreuth, 2004



## *Danksagung*

The author would like to thank Prof. Dr. S. Mackwell, Prof. Dr. H. Keppler and Prof. Dr. F. Seifert at Bayerisches Geoinstitut in Bayreuth University; Dr. Kate Wright and Andrew Walker at the Royal Institution in London (U.K.); Dr. Etienne Deloule at the CRPG in Nancy (France) and finally the european TMR Hydrospec network and an additional DFG grant for funding.



# Table of Contents

<b>Summary</b> .....	I
<b>Zusammenfassung</b> .....	IV
<b>1. Introduction</b> .....	1
1.1 Water in the Earth's interior: solubility and mobility .....	1
1.2. Olivine .....	6
1.2.1. Crystal chemistry.....	6
1.2.2. Hydrous defects.....	8
1.3. Wadsleyite.....	12
1.3.1. Crystal chemistry.....	13
1.3.2. Hydrous defects.....	15
1.4. Aim of this thesis.....	16
<b>2. Experimental methods</b> .....	19
2.1. Starting materials and sample preparations .....	19
2.2 Chemical composition.....	21
2.3. High pressure apparatus.....	23
2.3.1. Piston-cylinder apparatus.....	23
2.3.2. TZM rapid-quench cold-seal vessel.....	27
2.3.3. Multi-anvil press.....	28
2.4. Infrared analysis.....	32
2.4.1. Spectrometer and measurement parameters.....	32
2.4.2. Calculation of water content using infrared spectroscopy.....	35
2.5. Secondary ion mass spectrometry.....	38
2.6. Transmission electron microscopy.....	42
<b>3. Analysis of Diffusion</b> .....	43
3.1. Theory of diffusion - Fick's laws -.....	43
3.2. Diffusion in one dimension within a finite slab from an infinite source...44	
3.3. Mechanisms of diffusion.....	45

3.4. Ionic diffusion in olivine.....	48
3.5. Hydrogen diffusion in olivine.....	49
3.6. Hydrogen diffusion in a crystalline aggregate.....	51
<b>4. Results.....</b>	<b>53</b>
<b>4.1. Hydrogen diffusion in olivine.....</b>	<b>53</b>
4.1.1. Introduction.....	53
4.1.2. Results and discussion.....	53
4.1.3. Conclusions.....	65
<b>4.2. Hydrogen diffusion in forsterite.....</b>	<b>67</b>
4.2.1. Introduction.....	67
4.2.2. Infrared spectra and water contents.....	68
4.2.3. Diffusion rate and anisotropy.....	72
4.2.4. Discussion.....	75
4.2.5. Conclusions.....	79
<b>4.3. Dehydration profiles in mantle-derived olivine.....</b>	<b>81</b>
4.3.1. Introduction.....	81
4.3.2. Geological setting and sample characterization.....	81
4.3.3. Infrared spectra and water contents.....	85
4.3.4. Diffusion profiles in olivine.....	93
4.3.5. Mössbauer analysis.....	99
4.3.5. Discussion and implications for the upper mantle.....	101
4.3.6. Conclusions.....	105
<b>4.4. Temperature and pressure-dependence of water solubility in iron-free wadsleyite.....</b>	<b>107</b>
4.4.1. Introduction.....	107
4.4.2. Results.....	109
4.4.3. Discussion.....	117
4.4.4. Conclusions.....	123

<b>4.5. Computer simulation of hydrous defects in iron-free wadsleyite.....</b>	<b>125</b>
4.5.1. Introduction.....	125
4.5.2. Modelling solids and simulation of defects.....	125
4.5.3. Hydrous defects.....	132
4.5.4. Results.....	133
4.5.5. Discussion .....	136
4.5.6. Conclusions.....	139
<b>5. Conclusion.....</b>	<b>141</b>
<b>6. References.....</b>	<b>143</b>

## **Appendix**

Appendix 1: Kröger-Vink notation used for point defects .....	Appendix-i
Appendix 2: X-ray diffraction patterns for forsterite.....	Appendix-iii
Appendix 3: TEM documentation.....	Appendix-iv
Appendix 4: GULP results.....	Appendix-v

## **Erklärung**

## Abstract

### (1) Hydrogen diffusion in olivine

The kinetics of hydration of dry single crystals of San Carlos olivine was determined by performing experiments under water-saturated conditions. The experiments were performed at 1.5 GPa, 1000°C for 5 hours in a piston cylinder apparatus, or at 0.2 GPa, 900°C, for 1 and 20 hours in TZM cold-seal vessels. Polarized Fourier-transform infrared spectrometry (FTIR) was employed to quantify the hydroxyl distributions in the samples after the experiments. The new data obtained show a strong anisotropy of diffusion, with the diffusion coefficient  $\tilde{D}_{[100]} > \tilde{D}_{[010]} > \tilde{D}_{[001]}$  at 900°C for short duration experiments. This initial mechanism of diffusion possibly involved a redox-exchange between proton and polaron. After longer duration experiment, the anisotropy of diffusion is different with  $\tilde{D}_{[001]} > \tilde{D}_{[010]} \approx \tilde{D}_{[100]}$ . For this second stage of diffusion a model of hydrogen-metal vacancy associated defects is proposed, where the vacancies are the slower diffusing species with the diffusion laws:

$$D_{V_{Me}} [100], [010] = 10^{-(5.6 \pm 3.2)} \exp [-(175 \pm 76)/RT]$$
$$D_{V_{Me}} [001] = 10^{-(1.4 \pm 0.5)} \exp [-(258 \pm 31)/RT]$$

### (2) Hydrogen diffusion in forsterite

The kinetics of hydration linked to magnesium-vacancy diffusion within dry synthetic forsterite single crystals was determined by performing similar experiments and analyses as in the previous section. The experiments were performed at 1.5 GPa, 1000°C for 3 hours in piston cylinder apparatus, or at 0.2 GPa, 900-1110°C, for 3-20 hours in TZM cold-seal vessels. The chemical diffusion coefficients are marginally slower than in iron-bearing olivine for the same diffusion process, but the anisotropy of diffusion is the same, with the [001] axis the fastest direction of diffusion and [100] the slowest. Fits of the diffusion data to an Arrhenius law yield similar activation energies for each of the crystallographic axes; a global fit to all the diffusion data gave an activation energy around  $211 \pm 18 \text{ kJmol}^{-1}$ . Thus hydration likely occurs by coupled diffusion of protons and octahedrally coordinated metal vacancies. The

diffusion rates are fast enough to modify water contents within xenoliths ascending from the mantle but they are probably too slow to permit a total equilibration in a new dry or wet environment.

### **(3) Dehydration profiles in natural mantle-derived olivine within basalt**

First evidence for water diffusion in a natural mantle-derived olivine are presented from peridotite samples incorporated in basalt. The samples are olivine crystals within lherzolite xenoliths from the Quaternary alkali basalts of the Pali-Aike volcanic field in Patagonia.

Water content and distribution was studied using unpolarized and polarized FTIR spectrometry and analyses shows that olivine, Cr-diopside and orthopyroxene contain a significant amount of water, with up to 13 wt ppm H<sub>2</sub>O for olivine and up to 250 wt ppm H<sub>2</sub>O in the pyroxenes. In contrast, analysis of optically clear-parts of small garnet crystals indicates that they are dry.

Oriented Infrared profiles show that olivine grains larger than 0.5 mm have hydroxyl-depleted rims. These water concentration profiles suggest that partial dehydration occurred during the ascent of the xenolith-bearing magma to the Earth's surface, confirming that dehydration is occurring in the nature. From a combination of analyses of natural xenoliths with experimental diffusion works, ascent duration of the host magma is estimated to several hours, suggesting a fast rise up to the surface.

### **(4) Temperature and pressure dependence of water solubility in iron-free wadsleyite**

Previous experimental studies indicate that the maximum solubility of water in wadsleyite may vary as a function of pressure and temperature. Therefore wadsleyite samples were synthesized using a multi-anvil press. One series of experiments were performed at a fixed pressure of 15 GPa and at various temperatures and in a second series the temperature was fixed at 1200°C and pressure was varied from 13 to 18 GPa. The starting material corresponds to a composition of Mg<sub>2</sub>SiO<sub>4</sub> + 5wt% H<sub>2</sub>O. The water content was quantified by ion probe (SIMS). Results show that at 15 GPa, the water concentration decreases significantly with increasing temperature from 2.5 wt% H<sub>2</sub>O at 900°C down to 0.93 wt% H<sub>2</sub>O at 1400°C; the corresponding wadsleyite

Mg/Si ratios increase from 1.79 to 1.93 over this temperature range. Up to 17 GPa, no significant effect of pressure on the water content was observed. These results confirm the substitution mechanism previously proposed with  $\text{Mg} = 2\text{H}$ . Moreover, together with previous results on ringwoodite, these data imply a strong decrease of the water partition coefficient  $D_{\text{wadsleyite/ringwoodite}}^{\text{water}}$  between wadsleyite and ringwoodite with temperature.

### **(5) Computer simulation on hydrous point defect in iron-free wadsleyite**

The general utility lattice program (GULP), a semi-empirical method, was used to simulate the formation of point defects (Mott-Littleton method) in wadsleyite and especially hydrogen incorporation and their corresponding infrared frequencies. Various defects were under consideration such as: vacancies on all the different oxygen and magnesium sites and, for the first time, on the silicon. Furthermore, hydrated associated defects such as interstitial proton bonded to oxygen, hydroxyl(s) incorporated within magnesium vacancies and hydrated silicon vacancies were studied. Among of simulated defect, O1 is the most favourable site to attach hydrogen atom, in particular in association with a vacancy on Mg3. The calculated FTIR frequencies are too high as compared with experimental spectra. GULP permits a rapid evaluation of defect energies but unfortunately, does not provided yet satisfying infrared frequencies for embedded hydroxyl groups.

## Zusammenfassung

### (1) Diffusion von Wasserstoff in Olivin

Die Kinetik der Hydrierung von wasserfrei Olivin-Einkristallen wurde mit Hilfe von Experimenten unter wassergesättigten Bedingungen untersucht. Die Experimente wurden bei 1.5 GPa und 1000°C für 5 h in der Stempel-Zylinder-Apparatur, sowie bei 0.2 GPa und 900°C zwischen 1 und 20 h in TzM-Autoklaven durchgeführt. Die Hydroxylgehalte der experimentellen Proben wurden mit polarisierter Fouriertransform Infrarospektroskopie (FTIR) gemessen. Die ermittelten Diffusionskoeffizienten zeigten eine starke Anisotropie, wobei nach kurzen Experimenten (bei 900°C) die Diffusion von Wasserstoff in Richtung [100] schneller war als in [010], und diese wiederum schneller als in [001]. Nach längeren Experimenten änderte sich die Anisotropie, so dass [001] zur schnellsten Diffusionsrichtung für Wasserstoff wurde, während die Diffusion in [100] und [010] ungefähr gleich langsam verlief. Unter der Annahme, dass die Diffusion von Wasserstoff an Leerstellen der Metallionen gekoppelt ist, ergibt dies:

$$D_{V_{Me}} [100], [010] = 10^{-(5.6 \pm 3.2)} \exp [-(175 \pm 76)/RT]$$

$$D_{V_{Me}} [001] = 10^{-(1.4 \pm 0.5)} \exp [-(258 \pm 31)/RT]$$

### (2) Diffusion von Wasserstoff in Forsterit

Die Kinetik der Hydrierung durch Diffusion über Magnesium-Leerstellen in trockenen, synthetischen Forsterit-Einkristallen wurde in Experimenten unter wassergesättigten Bedingungen untersucht. Die Experimente wurden bei 1.5 GPa, 1000°C und 3 Stunden Dauer in Stempel-Zylinder-Apparaten sowie bei 0.2 GPa, 900-1110°C, für 3 bis 20 Stunden in den TzM-Autoklaven durchgeführt. Die chemischen Diffusionskoeffizienten sind niedriger als in natürlichen eisenhaltigen Olivinen für den gleichen Diffusionsmechanismus, aber die Anisotropie der Diffusion ist dieselbe, mit [001] als schnellster Richtung der Diffusion und [100] als der langsamsten Richtung. Die Anpassung einer Arrheniusbeziehung an die Diffusionsdaten erbrachte eine ähnliche Aktivierungsenergie für jede der kristallographischen Achsen; eine globale Anpassung an alle Diffusionsdaten resultierte in einer Aktivierungsenergie

von  $211 \pm 18 \text{ kJmol}^{-1}$ , in akzeptabler Übereinstimmung mit den vorhergehenden Resultaten für natürlichen Olivin. Die ermittelten Diffusionsraten sind schnell genug, um die Wassergehalte von Xenolithen des Erdmantels während ihres Aufstiegs zur Erdoberfläche zu ändern, aber sie sind wahrscheinlich zu langsam, um eine komplette Equilibrierung mit der neuen (trockenen oder feuchten) Umgebung zu erreichen.

### **(3) Dehydrationsprofile in natürlichen Olivin aus Peridotit-Xenolithen in Basalt**

Der Wassergehalt von xenolith-Mineralien (quaternäre Alkalibasalte, Pali-Aike Vulkanfeld in Südamerika) wurde orts aufgelöst mit unpolarisierter und polarisierter FTIR untersucht. Diese Messungen zeigen, dass Olivin, Chrom-diopsid und Orthopyroxen bedeutende Mengen an Wasser enthalten, wobei in den Olivinen bis 13 wt ppm  $\text{H}_2\text{O}$  und in den Pyroxenen bis 250 wt ppm  $\text{H}_2\text{O}$  gemessen wurden. Granatkristallen waren dagegen wasserfrei.

Durch orientierte Infrarotprofile kann gezeigt werden, dass die Hydroxylkonzentrationen zu den Rändern von grösseren Olivinkörnern ( $> 0.5 \text{ mm}$ ) hin abnehmen. Diese Abreicherung von Hydroxylionen zum Rand deutet darauf hin, dass während des Aufstiegs des Xenoliths zur Erdoberfläche eine teilweise Dehydratisierung auftrat und sie bestätigen gleichzeitig, dass ein solcher Effekt tatsächlich in der Natur auftritt. Durch die Kombination von Analysen der natürlichen Xenolithe mit experimentellen Diffusionsdaten konnte eine Aufstiegszeit von einigen Stunden für den Xenolithen abgeschätzt werden, d.h. der Aufstieg des Magmas bis zur Oberfläche erfolgt relativ rasch.

### **(4) Der Effekt von Temperatur und Druck auf die Löslichkeit von Wasser in Fe-freiem Wadsleyit**

Um diesen Effekt zu quantifizieren, wurden Proben von Wadsleyit mit einer Vielstempelpresse synthetisiert, wobei in einer Untersuchungsreihe der Druck mit 15 GPa festgelegt und die Temperatur variiert wurde, und in einer zweiten Reihe die Temperatur bei  $1200^\circ\text{C}$  fixiert und der Druck zwischen 13 bis 18 GPa verändert wurde. Das Ausgangsmaterial entsprach einer Zusammensetzung von  $\text{Mg}_2\text{SiO}_4 + 5\text{wt}\% \text{H}_2\text{O}$ . Der Wassergehalt wurde mit Hilfe einer Ionenmikrosonde (SIMS)

quantitativ bestimmt. Die Resultate zeigen, dass sich die Wasserkonzentration bei 15 GPa von 2.5 wt% H<sub>2</sub>O bei 900°C auf 0.93 wt% H<sub>2</sub>O bei 1400°C verringert. Die Mg/Si Verhältnisse im Wadsleyit erhöhten sich entsprechend von 1.79 zu 1.93 in diesem Temperaturintervall. Dagegen konnte kein signifikanter Einfluss des Druckes auf die Wasserlöslichkeit bei 1200°C festgestellt werden. Die gewonnenen Daten am Ringwoodit deuten weiterhin auf eine starke Abnahme des Wasser Verteilungskoeffizienten,  $D_{\text{wadsleyite/ringwoodite}}^{\text{water}}$ , zwischen Wadsleyit und Ringwoodit mit steigender Temperatur hin.

#### **(4) Computermodellierung von Wasserstoff Punktdefekten in Fe-freiem Wadsleyit**

Das General Utility Lattice Program (GULP) wurde eingesetzt, um die Bildung verschiedener Punktdefekte in Wadsleyit mit der halb-empirische Mott-Littleton Methode zu simulieren. Dabei wurde insbesondere der an Leerstellen gebundene Einbau von Wasserstoff und die damit verbundenen Infrarotfrequenzen modelliert. Verschiedene Defekte wurden in Erwägung gezogen: Leerstellen sowohl auf allen Sauerstoff- und Magnesiumpositionen, als auch auf Siliziumgitterplätzen. Ausserdem wurden mit der Hydrierung verbundene Punktdefekte simuliert. Die Hydrierung des Sauerstoffs auf der O1 Position ist der energetisch günstigste Punktdefekt des Wasserstoffs, insbesondere in Verbindung mit einer Leerstelle auf der Mg3 Position. Die errechneten FTIR Frequenzen sind verglichen mit experimentellen Spektren zu hoch.

# 1. Introduction

## 1.1 Water in Earth's interior: solubility and mobility

Water is perhaps the most important substance in the biosphere but its influence in geological systems can also be dramatic even at relatively small concentrations. The Earth's interior could store an amount of water equivalent to three times the world's oceans. Water is usually present in mantle minerals as trace amounts of hydroxyl groups. During the last decades, the presence of water in Earth's mantle has been proposed and demonstrated essentially using Fourier-transform infrared spectroscopy FTIR (Wilkins and Sabine, 1973; Beran and Zemann, 1986; Miller et al., 1987; Thomson, 1992; Gasparik, 1993; Sykes et al. 1994). Ingrin and Skogby (2000) present a review of results from investigations on natural samples and from experimental studies. Experimental studies on the solubility of water in nominally anhydrous minerals (NAMs) have been carried out for: *olivine* (Bai and Kohlstedt 1992, 1993; Kohlstedt and Mackwell 1999; Kohlstedt et al., 1996; Zhao et al., 2004), *pyroxenes* (Skogby and Rossman, 1990; Skogby et al. 1994; Bell et al. 1995; Bromiley and Keppler, 2004; Mierdel and Keppler, 2004) and *garnet* (Wang and Li 1999; Lu and Keppler, 1997, Blanchard and Ingrin, 2004). Table 1.1 presents water contents observed within NAMs of the upper mantle.

In this area of research, the main improvements have been due to experimental techniques, which allow investigation of hydrogen incorporation in the NAMs under various conditions and for a range of bulk compositions. In particular, experiments under lower mantle conditions have been experimentally challenging.

Smyth (1987) predicted that wadsleyite, the most abundant mineral in the upper transition zone, could contain several weight percent of water. McMillan et al. (1991, 1996) and Kohlstedt et al. (1996) experimentally confirmed this prediction. Bolfan-Casanova (2000, Bolfan-Casanova et al., 2000, 2002a, 2002b and 2003) has contributed essential data on the distribution of water within lower mantle minerals from partitioning experiments. These data suggest a nearly dry lower mantle and a water-rich transition zone. Water within the lower mantle and in Mg-perovskite could have major consequences on mantle dynamics. For this reason, water solubility in

perovskite and magnesiowüstite is still an important topic of debate (Williams and Hemley, 2001; Murakani et al., 2002; Litasov et al., 2003). Table 1.1 and Fig. 1.1 present actual water concentrations and water solubilities for minerals of the Earth mantle.

**Table 1.1** Range of water content in nominally anhydrous minerals from the Earth's mantle. Water contents for the upper mantle minerals are derived from FTIR measurements on xenolith samples (Ingrin and Skogby, 2000). In addition, experimental data on water solubilities in the mantle minerals.

Mineral	Water content <sup>§</sup> In natural sample (wt ppm H <sub>2</sub> O)	Water solubility <sup>§</sup> (wt ppm H <sub>2</sub> O)	T °C	P GPa	Ref.
Olivine	0 to ~140	1,510	1100	12	Kohlstedt et al. 1996
Clinopyroxene	up to ~1300	229 ± 20	1100	4	Bromiley et al. 2004
Orthopyroxene	60-650	867 ± 35	1100	7.5	Rauch and Keppler 2002
Garnet	0 to ~200	199	1000	10	Lu and Keppler, 1997
Wadsleyite		~ 23,000	1100	15	Kohlstedt et al. 1996
Ringwoodite		26,200	1100	19.5	Kohlstedt et al. 1996

§ Observed within mantle peridotite xenoliths (Ingrin and Skogby, 2000),

§ Resulting from experimental studies.

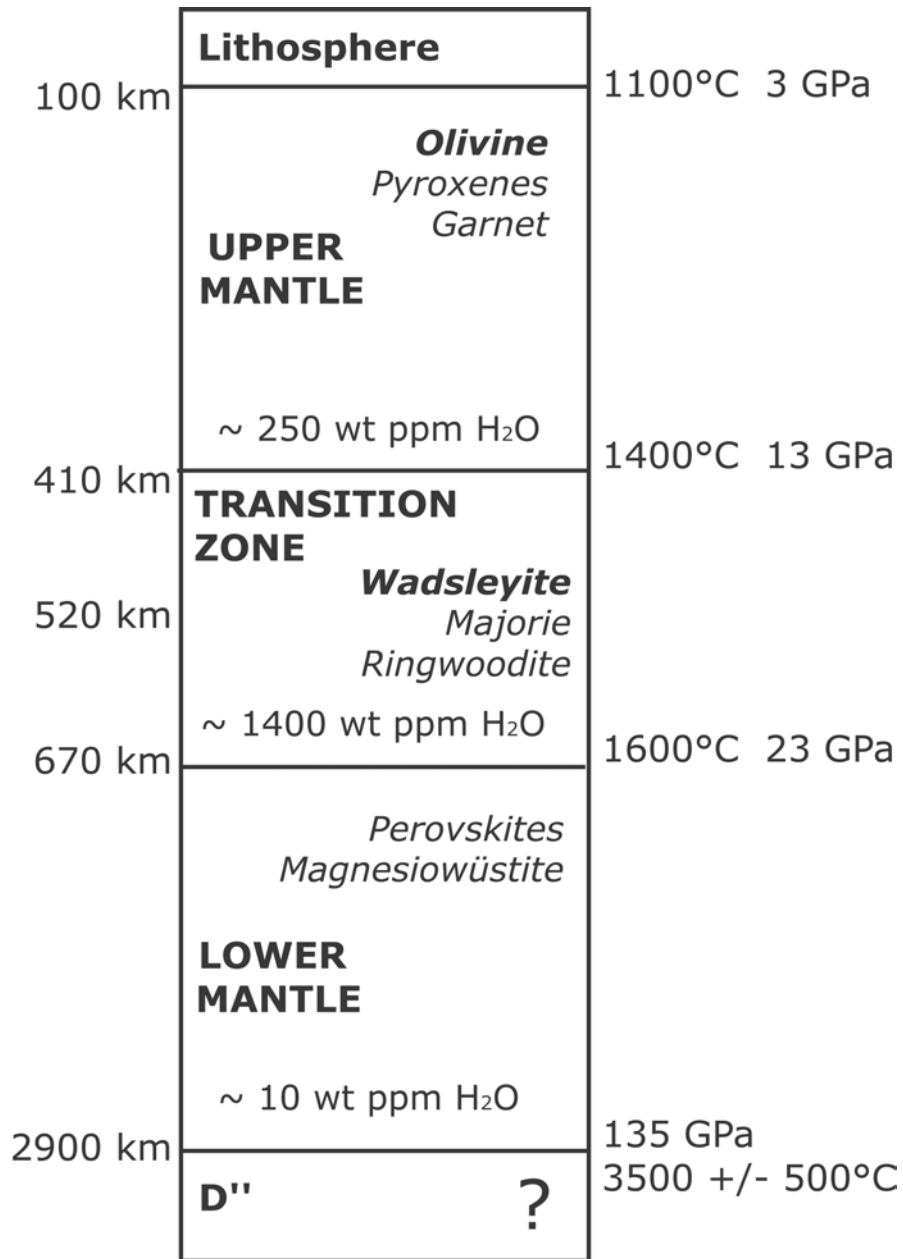


**Figure 1.1.** Schematic draw of the Earth's mantle showing the mineralogy and water capacity of the Earth's mantle (pyrolite composition) (redrawn from Bolfan-Casanova, 2000).

The presence of water has a considerable effect on the physical and chemical properties of the Earth's mantle minerals. Properties and processes influenced by water are *deformation and rheology* (Chopra and Paterson, 1984, Mackwell et al., 1988, 1985, 2000; Karato 1986), *melting and magma genesis* (Arndt et al., 1998; Gaetani and Grove, 1998; Hirth and Kohlstedt, 1993; Inoue, 1994; Sobolev and Chaussidon, 1996) *seismic velocities* (Bercovici and Karato 2003; Karato and Jung 1998) and *electrical conductivities* (Karato, 1990; Xu, 1998; 2000; Wanamaker and Duba, 1993; Hirsch and Shankland, 1993; Hirsch et al., 1993). Bahr and Simpson (2002) recently proposed a link between the anisotropy of water diffusion and deformation of the uppermost mantle (Bahr and Simpson, 2002 ; Simpson 2002a, 2002b ; Gatzmeier, 2003). In particular, transport properties such as *rheology* and *electrical conductivity* are extremely sensitive to OH defects. Such point defects also diffuse in response to changes in the thermochemical environment (Philibert, 1991); Crank 1975) and thus modify physical and chemical properties.

Mackwell and Kohlstedt (1990) and Kohlstedt and Mackwell (1998, 1999) demonstrated that hydrogen incorporation in olivine occurs by redox exchange during experiments at low temperatures for short experimental durations. This process only permits the incorporation of limited concentrations of water-derived species. At higher temperatures and/or longer experimental durations, additional hydrogen is incorporated by a second process that involves defect associates of protons and intrinsic defects, assumed to be metal vacancies by Kohlstedt and Mackwell (1998).

The diffusion of hydrogen in other NAMs such as enstatite, diopside and garnet has been studied as well. Table 1.2 presents the range of diffusivities obtained by hydration or dehydration experiments at 1000°C. Investigating the kinetics of such processes is necessary to evaluate the consequences of water incorporation (or extraction) on a geological scale and its consequences for magmatic processes.

The present study focuses on olivine and on wadsleyite, one of its high-pressure polymorphs. Before discussing in detail the nature of this work, the structure of olivine and wadsleyite will be briefly presented.

**Table 1.2** Hydrogen diffusivity in nominally anhydrous minerals from the upper mantle.

Mineral	D in m <sup>2</sup> /s at 1000°C			Ref.
	[100]	[010]	[001]	
Olivine (1 <sup>st</sup> process)	1.6 10 <sup>-10</sup>	6.2 10 <sup>-12</sup>	4.3 10 <sup>-12</sup>	Kohlstedt and Mackwell, 1998
Olivine (2 <sup>nd</sup> process)			8.3 10 <sup>-13</sup>	Kohlstedt and Mackwell, 1998
Clinopyroxene (Cr-diopside)	3.0 10 <sup>-10</sup>		2.1 10 <sup>-10</sup>	Carpenter-Wood et al. 1990
	<i>unpolarized</i> 1.4. 10 <sup>-12</sup>			Hercule and Ingrin, 1999
Orthopyroxene (enstatite)	1.6 10 <sup>-12</sup>	6.7 10 <sup>-11</sup>	6.7 10 <sup>-11</sup>	Carpenter-Wood, 2001
	1.1 10 <sup>-12</sup>	1.1 10 <sup>-12</sup>	3.3 10 <sup>-11</sup>	Stalder and Skogby, 2003
Garnet (pyrope)	6.7. 10 <sup>-11</sup>			Blanchard and Ingrin (2004 in press)
	1.2. 10 <sup>-11</sup>			Wang et al., 1996

## 1.2. Olivine

Mg-rich olivine is a common mineral of mafic and ultramafic rocks, and is generally considered to be the major constituent of the Earth's upper mantle (40-80% in volume) with a composition close to  $(\text{Mg}_{0.9}\text{Fe}_{0.1})_2\text{SiO}_4$  based on analyses of olivine in mantle xenoliths.

### 1.2.1. Crystal-chemistry

Olivine is an orthosilicate (Deer et al., 1997), and a solid solution between the two end-members *forsterite*,  $\text{Mg}_2\text{SiO}_4$  ( $\text{Fo}_{100}\text{Fa}_0$ ) and *fayalite*,  $\text{Fe}_2\text{SiO}_4$  ( $\text{Fo}_0\text{Fa}_{100}$ ). Olivine crystallizes in the orthorhombic symmetry (space group: *Pbnm*). Table 1.3 presents the important crystallographic parameters. The structure consists of independent  $\text{SiO}_4$  tetrahedra linked by divalent cations (M1 and M2) in sixfold co-ordination (Fig 1.2). The oxygen anions lie in sheets nearly parallel to (001) and are arranged in approximately hexagonal close-packing (Fig.1.3). Each oxygen atom is bonded to one silicon and three octahedrally co-ordinated cations. However, since the oxygen atoms are not perfectly close-packed, the M1 and M2 polyhedra are not regular, with the M2 site slightly larger than M1 site. The M1 site shares edges to form a band parallel to the [001] axis. These bands are connected to the next one in the upper layer by the M2 octahedral sites. There is apparently no complete ordering in the Mg/Fe<sup>2+</sup> distribution between the M1 and M2 site, but Fe<sup>2+</sup> has a preference for the M1 site. M1 and M2 may also be occupied by other cations such as Ni<sup>2+</sup>, Mn<sup>2+</sup>, Ca<sup>2+</sup> (CaMgSiO<sub>4</sub>, monticellite), Cr<sup>3+</sup> (Deer et al., 1997) or B<sup>3+</sup> (Sykes et al, 1994). In particular, xenolithic olivines are well-known to contain a small amount of nickel (Frey and Prinz, 1976). The high-pressure and high-temperature polymorphs of olivine are wadsleyite  $\beta$ -(Mg, Fe)<sub>2</sub>SiO<sub>4</sub> and ringwoodite  $\gamma$ -(Mg, Fe)<sub>2</sub>SiO<sub>4</sub>. Wadsleyite crystal-chemistry and potential hydrous defects are discussed in section 1.4.

**Table 1.3** Lattice constants and densities of olivines from (Deer et al., 1997).

	Forsterite	Mantle olivine	Fayalite
Chemical formula	$\text{Mg}_2\text{SiO}_4$	$(\text{Mg}_{0.9}\text{Fe}_{0.1})_2\text{SiO}_4$	$\text{Fe}_2\text{SiO}_4$
a Å	4.7540	4.755	4.8211
b Å	10.197	10.21	10.4779
c Å	5.9806	5.985	6.0889
Density $\text{g/cm}^3$	3.222	~ 3.4	4.392

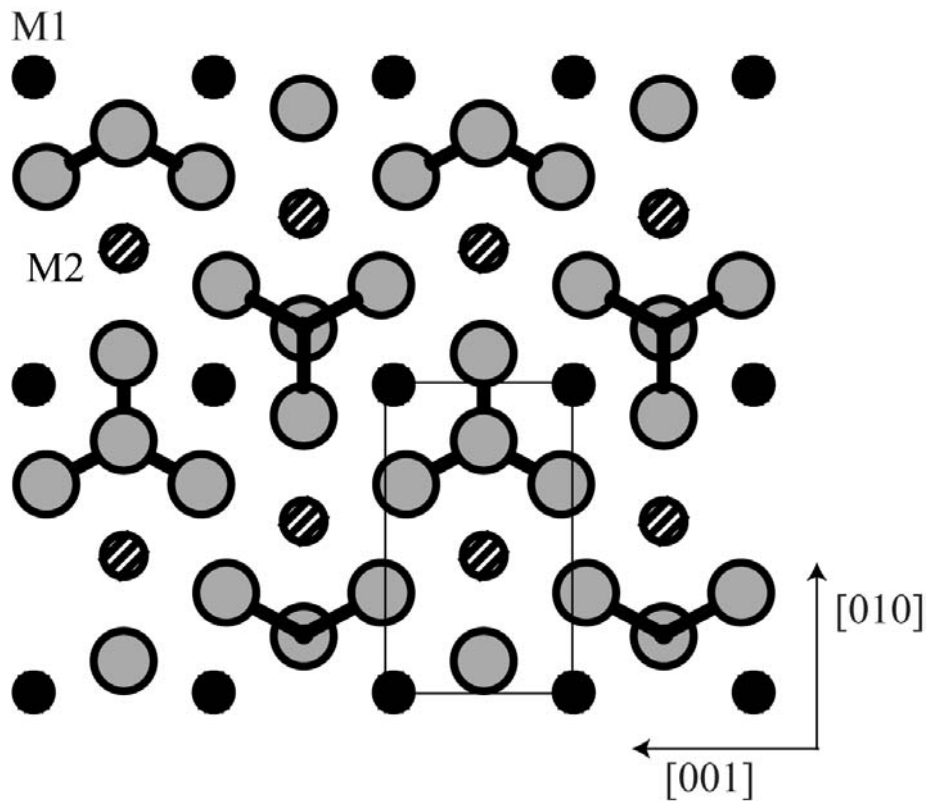


**Figure 1.2.** Idealized forsterite structure projected on (100) (redraw from Deer et al., 1997). Si atoms are at the center of the tetrahedrons. *Small black circle* Si ; *large gray circle*, oxygen ; *black circle*, M1 ; *diagonally hatched circle*, M2.

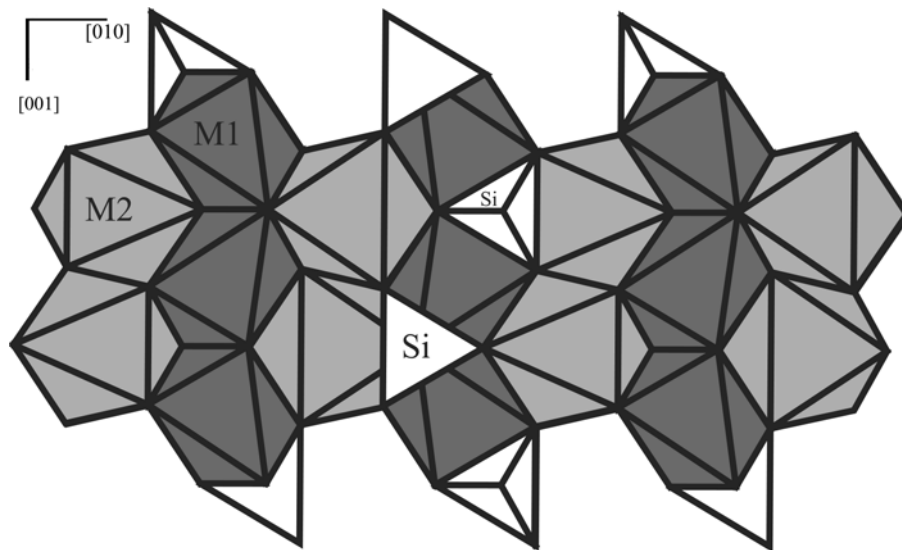


**Figure 1.3.** Forsterite structure perpendicular to (100) showing the approximately hexagonal close-packing structure (redraw from Deer et al., 1997).

### 1.2.2. Hydrous defects

Infrared spectroscopic measurements show that natural olivine, a nominally anhydrous mineral, can contain “water”. This “water” may occur as H<sub>2</sub>O in hydrous minerals included as separate phases in the olivine structure or as water-rich fluid/glass/melt inclusions or as hydroxyl point defects dissolved in the crystal structure (Miller et al., 1987; Beran and Putnis, 1983). Natural olivine crystal can contain up to 220 wt ppm H<sub>2</sub>O, (Bell et al. 2003). Experimental studies have shown that the point defect solubility of water in olivine increases with increasing water fugacity (Bai and Kohlstedt, 1992; Kohlstedt et al., 1996). In addition there is some influence of temperature (Zhao et al., 2004), redox conditions (Bai and Kohlstedt, 1992) and iron content (Zhao et al., 2004) on water solubility.

Olivine can contain lamellae of hydrous magnesium silicates such as talc, serpentine, or humites, which have a crystal structure similar to olivine. In this case, extra bands will be visible in infrared spectra in the 3710-3300  $\text{cm}^{-1}$  wavenumber range. Details of such bands are reported in Table 1.4.

**Table 1.4.** Principal hydrous minerals, which can be included in olivine as structural hydrous lamellae (from Miller et al., 1997).

Mineral	Chemical composition	(OH) infrared band position in $\text{cm}^{-1}$
Serpentine	$\text{Mg}_3[\text{Si}_2\text{O}_5](\text{OH})_4$	3709
		3685
		3645
Talc	$\text{Mg}_6[\text{Si}_8\text{O}_{10}](\text{OH})_4$	3675
		3678
		3662
Humite group (n=1, 2, 3 and 4 for norbergite, chondrodite, humite and clinohumite, respectively)	$(n \text{ Mg}_2\text{SiO}_4) \cdot [\text{Mg}(\text{OH},\text{F})_2]$	3580
		3559
		3558
		3598

Olivine may also contain fluid, glass or melt inclusions. In this case, the infrared bands in the OH region yield a large and isotropic broad band similar to the hydroxyl group feature in hydrous melts (Ihinger et al, 1994). The use of polarized infrared radiation makes it possible to discriminate between pleochroic  $\text{OH}^-$  fixed in the structure and hydrous inclusions.

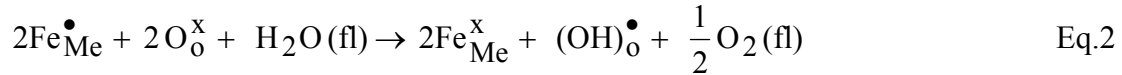
Finally, olivine can incorporate hydrogen as point defects within the structure. The nonstoichiometry resulting from point defects occurring in olivine is well recognized (Nakamura and Schmalzried, 1983; Tsai and Dieckmann, 1997; 2002; Smyth and Stocker, 1975; Beran and Putnis, 1983). Basically, (1) hydrogen in olivine is always bonded to an oxygen atom to form a hydroxyl group and (2) this hydrogen atom may partially substitute either for a divalent cation (e.g., Mg) or for a silicon

atom. However it is still difficult to quantify the defect populations. Polarons and protons can be incorporated in the olivine structure at a level around the 100 at. ppm level at low pressure (Nakamura and Schmalzried, 1983; Tsai and Dieckmann, 1997). A polaron ( $h^\bullet$ ) is a hole or an electron-deficient (Serway et al., 1997). Hydrogen can be incorporated in olivine by major defect associations formed by various reactions (Mackwell and Kohlstedt, 1990). Incorporation reactions are presented here using the Kröger-Vink notation (Kröger and Vink, 1956, see also appendix 1).

1. Redox-exchange reaction, which involves polarons (electron hole,  $h^\bullet$ ) as,



or



with the associated defect  $Fe_{Me}^\bullet = \{Fe_{Me}^x, h^\bullet\}$ .

2. An association of defects formed between a proton and a metal vacancy,



3. An association of defects formed between a proton and a silicon vacancy is also possible as,



Brodholt and Refson, (2000) performed an *ab initio* calculation in order to quantify the activation energy for these two last reactions in end-member forsterite. Assuming the existence of both Si and Mg vacancies, protons will initially populate Si vacancies until there are three protons in each vacancy. Afterwards, the addition of one more proton is energetically unfavorable in comparison to incorporation by occupying the Mg vacancy. Therefore, the next proton will occupy a Mg vacancy. Further computer calculations are in progress for hydrous defects in iron-bearing olivine (Andrew Walker and Kate Wright, person. comm.).

The presence of hydrogen is detectable by infrared spectroscopy as a series of OH absorption bands, which occurs in the 3800 to 3000  $\text{cm}^{-1}$  wavenumber range when they are incorporated in minerals (Aines and Rossman, 1984). As a reference, general positions of water and hydroxyl vibrational modes (as gas and liquid state) are presented in Table 1.5 (Siesler et al., 2002; Ihinger et al., 1994 ; Aines and Rossman, 1984). In San Carlos olivine (an anisotropic solid), the orientation of the O-H dipole has a major component parallel to the [100] direction. In contrary, the O-H dipole in forsterite appears to be mainly oriented parallel to the [001] direction. In both case, the strong anisotropic behavior of hydroxyl bands means that polarized measurements are necessary to quantify water contents.

The number, variety and wavenumber position of the infrared bands are indicative of differences in the lattice environment. In previous studies the infrared bands have been assigned to certain defects mostly on band anisotropy and frequency (e.g., Beran and Putnis, 1983; Freund and Oberheuser, 1986). In the recent work from Matveev et al. (2001) hydroxyl bands between 3380-3285  $\text{cm}^{-1}$  were assigned as hydrogen linked to divalent metal vacancies whereas hydroxyl bands at higher-frequencies 3640-3430  $\text{cm}^{-1}$  and at 3295  $\text{cm}^{-1}$  were attributed to hydrogen substitution in tetrahedral (silicon) sites. Many of these infrared bands have been assigned to both types of hydrous point defects in olivine. However, precise band assignments are still uncertain.

Hydration experiments at high-pressure and high-temperature on olivine and forsterite are thus an approach to study nonstoichiometry by decorating other point defects with hydrogen.

**Table 1.5** General position of OH vibrational modes in H<sub>2</sub>O, as gaseous phase from Siesler et al., (2002) and Ihinger et al., (1994), and as liquid phase at room temperature (296-308 K) from Aines and Rossman, (1984).

Wavenumber	Species	vibration mode	References
1595 cm <sup>-1</sup>	H <sub>2</sub> O <sub>gaz</sub>	OH bend ( $\nu_2$ )	Siesler et al., 2002 Ihinger et al., 1994
3657 cm <sup>-1</sup>	H <sub>2</sub> O <sub>gaz</sub> , OH <sup>-</sup>	OH symmetric stretch ( $\nu_1$ )	Siesler et al., 2002 Ihinger et al., 1994
3758 cm <sup>-1</sup>	H <sub>2</sub> O <sub>gaz</sub> , OH <sup>-</sup>	OH asymmetric stretch ( $\nu_3$ )	Siesler et al., 2002 Ihinger et al., 1994
5235 cm <sup>-1</sup>	H <sub>2</sub> O <sub>gaz</sub>	OH combination ( $\nu_2 + \nu_1$ )	Siesler et al., 2002
1620 cm <sup>-1</sup>	H <sub>2</sub> O <sub>liq</sub>	OH bend ( $\nu_2$ )	Aines and Rossman, 1984
3220 cm <sup>-1</sup>	H <sub>2</sub> O <sub>liq</sub> , OH <sup>-</sup>	OH symmetric stretch ( $\nu_1$ )	Aines and Rossman, 1984
3445 cm <sup>-1</sup>	H <sub>2</sub> O <sub>liq</sub> , OH <sup>-</sup>	OH asymmetric stretch ( $\nu_3$ )	Aines and Rossman, 1984
7100 cm <sup>-1</sup>	H <sub>2</sub> O <sub>liq</sub> , OH <sup>-</sup>	First OH stretching overtone	Aines and Rossman, 1984

#### 1.4. Wadsleyite

Olivine has two high-pressure polymorphs: wadsleyite and ringwoodite, which are characteristic of the transition zone of the Earth's mantle, where they exist in association with majoritic garnet. Wadsleyite was previously called modified spinel phase or  $\beta$ -phase, while ringwoodite was called  $\gamma$ -phase and has a spinel structure (Moore and Smith, 1970). Wadsleyite and ringwoodite were first synthesized (Ringwood and Major, 1966) before they were found in shocked meteorites. Natural wadsleyite was observed for the first time within the Tenham chondrite (Price et al., 1979) but later than ringwoodite within the same meteorite (Binns et al. 1969). Wadsleyite samples from the Earth's mantle are not accessible and studying synthesized samples using high-pressure and high-temperature apparatus (multi-anvil press, diamond-anvil cell), is the only way to investigate such materials at mantle

conditions. Fig. 1.4 presents a phase diagram showing the stability field of the different  $\text{Mg}_2\text{SiO}_4$  polymorphs under anhydrous conditions.

#### 1.4.1. Crystal-chemistry

Wadsleyite is a sorosilicate and crystallizes in the orthorhombic system, space group *Imma* (Moore and Smith, 1970). The structure is based on a nearly perfect cubic close-packing of oxygen atoms with silicon atoms in tetrahedral sites ( $\text{Si}_2\text{O}_7$  groups). They are corner-linked to octahedral chains occupied by divalent or trivalent cations ( $\text{Mg}^{2+}$ ,  $\text{Fe}^{2+}$  or  $\text{Fe}^{3+}$ ). Three octahedral sites can be distinguished, M1, M2 and M3. However, 2 oxygen atoms (O1 site) in the M3 octahedral are not bonded to silicate tetrahedra. Wadsleyite also has a monoclinic polymorph (space group *I2/m*), which was recently identified by Smyth et al, (1997). The principal crystal-chemical data are reported in Table 1.5. Figure 1.5 and Figure 1.6 show different views of the wadsleyite structure.

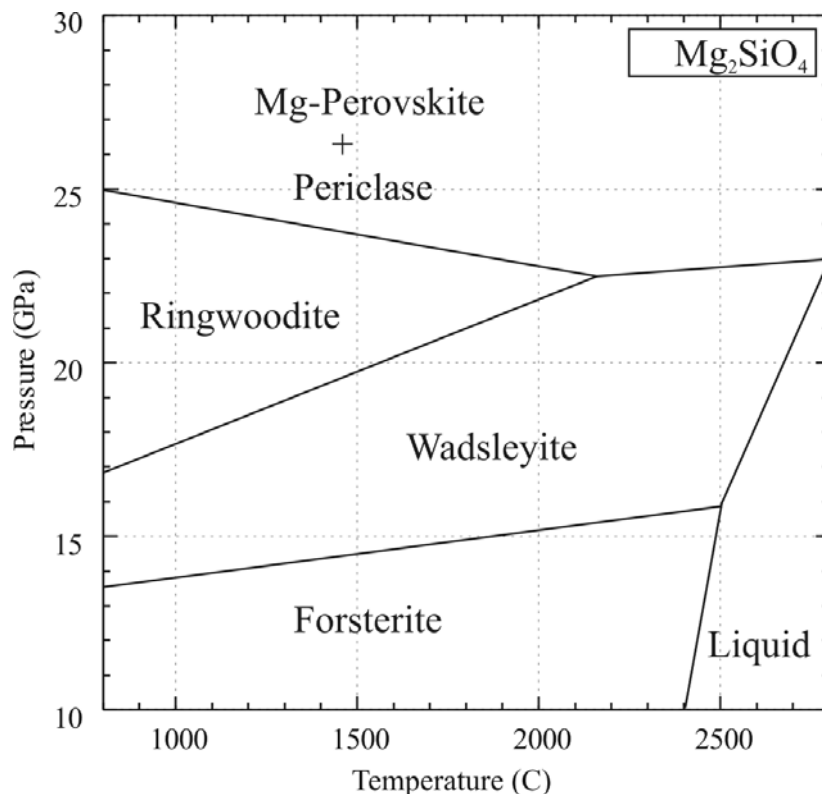


**Figure 1.4.** Phase diagram of  $\text{Mg}_2\text{SiO}_4$  as a function of pressure and temperature under anhydrous conditions (D. Frost, person. comm.). A similar phase diagram is available in Fei et al. (1990)

**Table 1.5** Lattice constants and densities of orthorhombic and monoclinic wadsleyite.

Chemical formula	Wadsleyite		
	$\beta\text{-Mg}_2\text{SiO}_4$	$\beta\text{-(Mg,Fe)}_2\text{SiO}_4$	$\beta\text{-(Mg,Fe)}_2\text{SiO}_4$
Space group	<i>Imma</i>	<i>Imma</i>	* <i>I2/m</i>
a Å	5.6921(2)	5.70(2)	5.6715(7)
b Å	11.460(1)	11.51(7)	11.582(2)
c Å	8.253(2)	8.24(4)	8.258(1)
$\beta^\circ$	90	90	90.397(9)°
Density $\text{g/cm}^3$	3.47	3.84	3.511
Reference	Finger et al. (1993)	Price et al (1983)	Smyth et al. (1997)

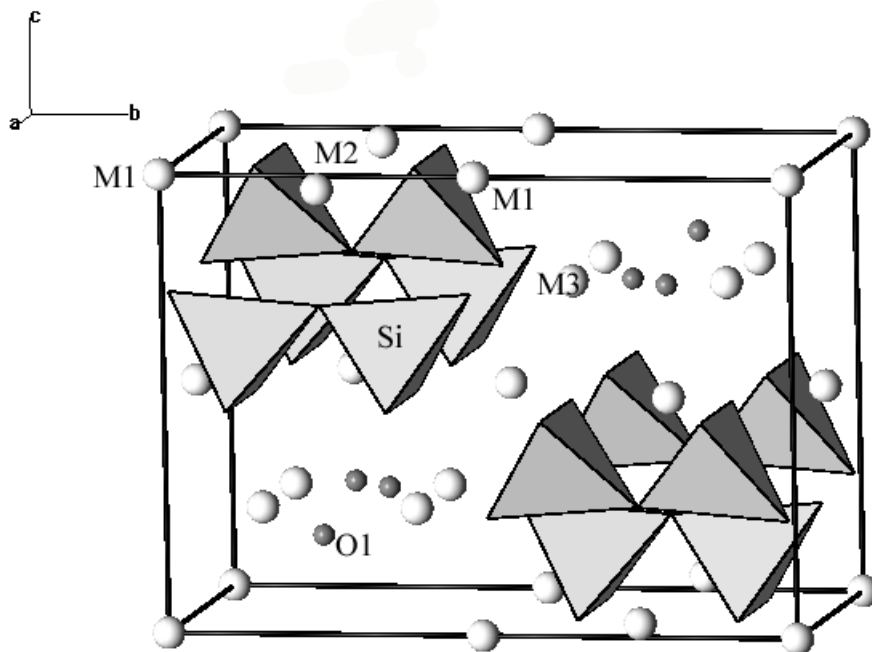


**Figure 1.6.** Wadsleyite structure. Si atoms are in the center of the *grey tetrahedra*; small *gray circle*: oxygen O1 not bound to Si; M1, M2, M3 shown as *white spheres*.

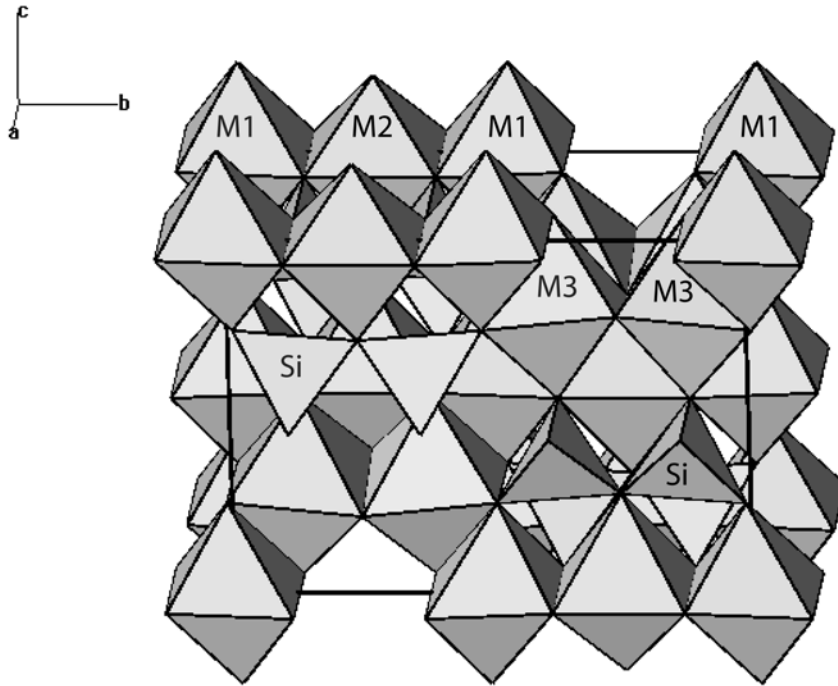


**Figure 1.6.** Polyhedral model of the wadsleyite structure.

#### *1.4.2. Hydrous defects*

As predicted by Smyth (1987) and confirmed by McMillan et al. (1991) using infrared spectroscopy, wadsleyite is able to easily fix hydrogen within its structure and in a larger amount than olivine (Kohlstedt et al, 1996). Effectively the O1 site, which is not attached to silicon tetrahedra, is a very favorable site to bond hydrogen. This hydrous defect would be balance by the formation of magnesium vacancy (Smyth, 1987; 1994). Figure 1.7 shows the model for hydrous wadsleyite with H bonded to O1. Inoue et al. (1995) have reported water contents up to 3.3 wt% H<sub>2</sub>O in iron-free wadsleyite measured with secondary ion mass spectrometer (SIMS) while Kohlstedt et al. (1996) reported only 2.4 wt% H<sub>2</sub>O using unpolarized near infrared spectroscopy.

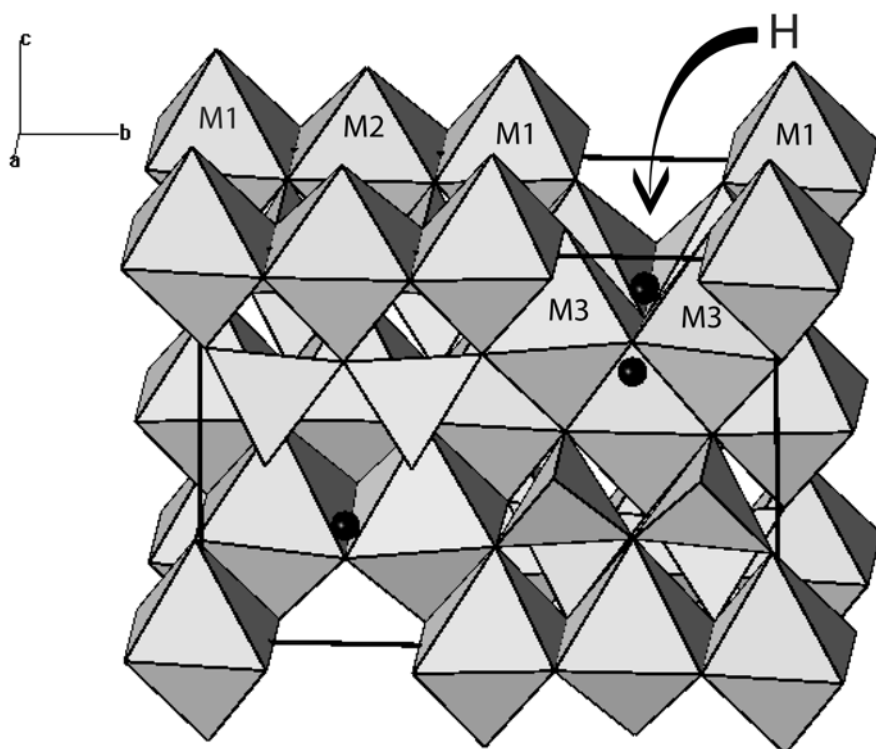


**Figure 1.7.** Hydrous wadsleyite structure model. The H atom is located directly above O1, which is shared by the four M3 octahedra.

### 1.5. Aim of this thesis

As observed for other nominally anhydrous minerals of the Earth's upper mantle (Carpenter-Wood, 2001; Ingrin and Skogby, 2000; Rauch, 2000; Zhao et al., 2001; Bromiley and Keppeler, 2004), chemical composition has an important effect on water solubility and hydrogen diffusivity in olivine. Understanding these effects is important; because water concentration and hydrogen mobility control processes and properties such as deformation, phase equilibria, rheology and electrical conductivity.

The primary aim of this work was to study the kinetics of hydrogen diffusion in an iron-free olivine (forsterite). This constrains the speciation of the mobile water-derived defects in synthetic forsterite, where there is no iron and, hence, no polarons (electronic holes). Hydration experiments were first carried out on iron-bearing olivine and, afterwards exactly and strictly the same experimental procedure was used to hydrate forsterite. Thus using Fourier transform infrared spectroscopy (FTIR), hydrogen solubility and kinetics of hydrogen incorporation in olivine and forsterite single crystals can be compared. These data provide new insights into diffusion mechanisms.

The diffusion models were applied to a natural garnet-lherzolite xenolith from Pali-Aike, Patagonia. This xenolith shows hydrogen diffusion profiles within olivine crystals. This is the first evidence of hydrogen diffusion in mantle-derived olivine. This, combining analyses of a natural xenolith with experimental diffusion data allows constraint on conditions during ascent of the host magma.

Going deeper into the Earth's mantle, the temperature and pressure dependencies on water solubility in iron-free wadsleyite were investigated. This topic was motivated by recent publications, which point towards a variability in water content as a function of synthesis conditions. As a complement to this experimental work, computer calculations using general utility lattice program (GULP) were performed to determine the most favorable hydrous point defects within iron-free wadsleyite structure.

These different studies lead to major advances in thermodynamics and kinetics of water in olivine and wadsleyite.



## 2. Experimental methods

### 2.1. Starting materials and sample preparations

#### *Hydration experiments on olivine and forsterite*

Two types of olivine single crystals were used for hydration experiments. First, I worked with gem quality iron-bearing olivine from San Carlos, Arizona. The same type of olivine crystals were previously described and used by Kohlstedt and Mackwell (1997), Mackwell and Kohlstedt (1990), and Bai et al., (1991). Only optically inclusion-free and uncracked crystals were selected for experiments.

Second, I used synthetic iron-free olivine (forsterite). The forsterite samples were cut from a synthetic single crystal donated by M. Paterson.

Before a hydration experiment, each crystal, either olivine or forsterite, was crystallographically oriented using optical microscopy and a X-ray precession camera. The orientation was checked using Laue X-ray diffraction patterns (in collaboration with F. Bromiley, appendix 2). Rectangular prisms then were cut with faces perpendicular to each crystallographic axis ( $\pm 5^\circ$ ) and carefully polished using diamond films from 30 to 0.5  $\mu\text{m}$  grain size. The final sample size was around  $2.5 \times 3 \times 2 \text{ mm}^3$  parallel to [100], [010] and [001], respectively. The exact size of each single crystal is given in Table 2.1 and Table 2.2. A first infrared measurement was performed to check the water content of the San Carlos olivine single crystals. The samples SC32 and SC33 were dry within the detection limit of the FTIR measurements ( $\sim 1\text{H}/10^6 \text{ Si}$ ). Afterwards, the samples were equilibrated by annealing at  $1300^\circ\text{C}$  for 20 hours at room pressure with the oxygen fugacity around  $10^{-7.3} \text{ atm}$

## 2. Experimental methods

---

(equivalent to the Ni-NiO buffer) controlled by a CO-CO<sub>2</sub> gas-mixture. This step is necessary in order to equilibrate point defect populations in the crystal structure to values near those during the subsequent hydrothermal annealing experiments. Infrared analysis was performed to verify the dry state of the samples. A platinum crucible was used to anneal the forsterite. To avoid chemical interaction between Fe within the olivine and Pt (Kohlstedt and Mackwell, 1987), olivine crystals were annealed surrounded by other olivine crystals in an alumina crucible.

**Table 2.1.** Dimensions (in mm) of olivine samples. Only samples from successful experiments are listed here (i.e., samples survived the experiments largely uncracked).

# Run	# sample	// [100]	// [010]	//[001]
SD 14	SC 32-G	2.99	1.81	1.52
SD 15	SC 32-B	1.39	1.84	3.00
SD 20	SC 33-A	2.53	2.64	2.32
SD 21	SC 33-B	2.53	2.64	2.32

**Table 2.2.** Dimensions (in mm) of forsterite samples. Only samples from successful experiments are listed here.

# Run	# sample	// [100]	// [010]	//[001]
SM	Fo1-3	1.92	0.50	0.99
SD 9	Fo2-2	2.43	2.86	2.08
SD 17	Fo2-5	2.43	2.86	2.09
SD 18	Fo2-6	2.42	2.85	2.08
SD 19	Fo2-4	2.43	2.87	2.09
SD 26	Fo2-8	2.43	2.87	2.09
SD 27	Fo2-9	2.43	2.87	2.09
SD 28	Fo2-10	2.43	2.87	2.09
SD 30	Fo2-12	2.33	2.82	1.90
SD 31	Fo2-13	2.33	2.82	1.90
SD 32	Fo2-14	2.33	2.82	1.90
SD 33	Fo2-15	2.33	2.82	1.90

### *Phase equilibria experiments in the system MgO-SiO<sub>2</sub>-H<sub>2</sub>O*

These experiments were performed using a mixture of SiO<sub>2</sub>, MgO and Mg(OH)<sub>2</sub> powders (99.9 % purity grade, Chempur) that yielded a wadsleyite composition of Mg<sub>2</sub>SiO<sub>4</sub> + 5 wt% H<sub>2</sub>O.

After the experiments, each capsule was pierced to check for excess water (water bubble escaping from the capsule). The run products were mounted in crystal bond and doubly polished to a thickness between 120 and 350 μm for optical microscopy observations, Raman spectroscopy identification of wadsleyite, and electron microprobe analysis (EMPA). Special preparation was necessary prior to the secondary ion mass spectrometry (SIMS) analyses, which is detailed in the SIMS section 2.5.

### *Sample preparation for transmission electron microscope (TEM) observations*

Each sample was polished using diamond-lapping films (30, 15, 6, 3 μm grain size) until a thickness of 30 μm. Afterwards, the sample was mounted on a copper grid, thinned to electron transparency by ion beam bombardment using a Gatan Duomil ion milling machine, and carbon coated.

## **2.2 Chemical composition**

The chemical analyses presented in this thesis were obtained using a Cameca SX50 electron microprobe (EMPA) with the following configuration: voltage equal to 15 keV, 15 nA point beam and 20 second counting time. The EMPA standards and specific procedures used are given in Table 2.3.

### *Hydration experiments on olivine and forsterite*

The chemical composition of the olivine and forsterite were characterized prior to the diffusion experiments. Average content for each element was determined from over 20 analyses. In addition, inductively coupled plasma-atomic emission spectrometry (ICP-AES) analysis of the synthetic forsterite crystal yielded a high boron content

## 2. Experimental methods

(737 at. ppm in Fo2 samples, Table 2.1), which is probably due to the use of boron as a flux during crystal growth. The chemical compositions for olivine and forsterite starting material are given in Table 2.4.

**Table 2.3** Standards and specific procedure used for EMPA.

Elements	Standard	Emission line	Crystal
Si	Enstatite (Mg <sub>2</sub> Si <sub>2</sub> O <sub>6</sub> )	K $\alpha$	TAP
Mg	Enstatite (Mg <sub>2</sub> Si <sub>2</sub> O <sub>6</sub> )	K $\alpha$	TAP
Al	Spinel (MgAl <sub>2</sub> O <sub>3</sub> )	K $\alpha$	TAP
Fe	Pure Fe	K $\alpha$	LiF
Ca	Diopside (CaMgSiO <sub>6</sub> )	K $\alpha$	PET
Mn	Pyrophanite (MnTiO <sub>3</sub> )	K $\alpha$	LiF
Na	Jadeite (NaAlSiO <sub>6</sub> )	K $\alpha$	TAP
Ni	Pure Ni	K $\alpha$	LiF
Cr	Pure Cr	K $\alpha$	LiF
Ti	MnTiO <sub>3</sub>	K $\alpha$	LiF
Pt (Cameca)	Pure Pt	M $\alpha$	PET
Pt (JEOL)	Pure Pt	L $\alpha$	LiF

TAP= Thalliumhydrogenphthalat

PET= Pentaerythritol

LiF = Lithium fluorite

**Table 2.4.** Chemical compositions of the starting material for diffusion experiments in olivine and forsterite. (Table includes only those elements that were above the detection limit).

Sample	Origin	Chemical composition
Olivine	San Carlos, Arizona	(Mg <sub>0.904</sub> Fe <sub>0.092</sub> Ni <sub>0.0035</sub> Cr <sub>0.0003</sub> ) <sub>2</sub> SiO <sub>4</sub>
Forsterite	Synthetic	Mg <sub>2</sub> SiO <sub>4</sub> + 737 at.ppm Boron

### *Peridotite from Pali-Aike*

The analytical procedures used were similar to those for the other materials. The chemical compositions of the minerals from the peridotite xenoliths are presented and discussed in the results section 4.3.

### *Phase equilibria experiments in the system MgO-SiO<sub>2</sub>-H<sub>2</sub>O*

Chemical composition analyses were also obtained using the Cameca for the hydrous wadsleyite samples. For samples H2011, H2058, H2045 and H2044 a second analysis was performed using the new microprobe JEOL JXA-8200 with an identical configuration (15 keV, 15nA, point beam, 20 second counting time). EMPA were performed after SIMS measurements, on the same wadsleyite crystals at around 30-40  $\mu\text{m}$  from the ion probe craters (i.e., sputtering relics). The co-existing melt phase was analyzed only using the new JEOL JXA-8200 with a defocused beam (aperture of 10  $\mu\text{m}$ ) in order to determine an average chemical composition for the quenched crystallized melt.

### **2.3. High-pressure apparatus**

The hydration experiments on olivine and forsterite at high pressure and high temperature were first performed in a piston-cylinder apparatus. However, because of significant cracking of the samples during decompression, titanium-zirconium-molybdenum (TZM) cold-seal vessels were used for most experiments.

#### **2.3.1. Piston-Cylinder**

Hydration experiments were initially carried out in a piston-cylinder apparatus (Bohlen, 1984; Boyd and England, 1960; Johannes et al., 1971). A schematic drawing of the end-loaded piston-cylinder apparatus is presented in Figure 2.1. Run conditions were  $1.5 \pm 0.1$  % (friction corrections 20% and pressure calibration from Bromiley and Keppler, 2004), 1000°C for 3 hours ( $\pm 3$  second). The temperature was controlled using a Pt<sub>100%</sub>-Pt<sub>90%</sub>Rh<sub>10%</sub> thermocouple (i.e., type S - no corrections for the effect of pressure on the temperature emf were applied). The temperature gradient is estimated to be less than 25 °C for the conditions applied (Bromiley and Keppler, 2004).

Talc-Pyrex<sup>TM</sup> cells (Hudson et al., 1994) were used with an alumina or talc cylinder and alumina plugs around the capsule and a tapered graphite furnace (Figure 2.2). Samples were welded into iron capsules (only for sample Fo1-3) or Pt<sub>0.95</sub>-Rh<sub>0.05</sub>

capsules along with 10  $\mu\text{L}$  of water. The capsules were constructed from 5 mm diameter, thin-walled Fe or  $\text{Pt}_{0.95}\text{-Rh}_{0.05}$  tubing with a wall thickness of 0.2 mm and length of 1 cm. The oxygen fugacity,  $fO_2$ , was controlled by adding iron-wüstite powder, Ni-NiO powder, or Ni-foil together with NiO powder. For each experiment, the corresponding  $fO_2$  was calculated using the data from O'Neill (1978b) for the Ni-NiO buffer and from O'Neill and Wall (1978a) for the Fe-FeO buffer. In order to control silica activity, a fine powder (10-20  $\mu\text{m}$  grain size) of San Carlos olivine with 10% of San Carlos enstatite was added. Only iron-free enstatite was added to experiments with forsterite. This powder was previously prepared by mixing pure MgO and pure  $\text{SiO}_2$  powder (99.9 % purity grade, Chempur) in stoichiometric proportions. Afterwards the powder was heated twice to form enstatite powder in a gas-mixing furnace at 1100  $^\circ\text{C}$ , where the  $fO_2$  was controlled along the Fe-FeO or Ni-NiO buffer join. After each experiment, the presence of both Ni and NiO (or Fe and FeO) in the capsule was checked using optical microscopy to verify that neither component of the buffer was consumed. Electron microprobe analysis was used to check for Ni diffusion into the single crystal sample, but no evidence of Ni contamination was observed. The Ni-NiO buffer has the advantage to be effective for long experiments. The Fe-FeO buffer is exhausted after 3 hours due to oxidation by water and loss of hydrogen from assembly.

In order to avoid cracks during the quench, the temperature was decreased over about  $3 \pm 1$  minute, followed by decompression over 5 days. Unfortunately, even with this precaution, it was still difficult to preserve single crystals without significant cracking. Therefore, most experiments were performed with the TZM cold-seal vessel, where the pressure is hydrostatic.

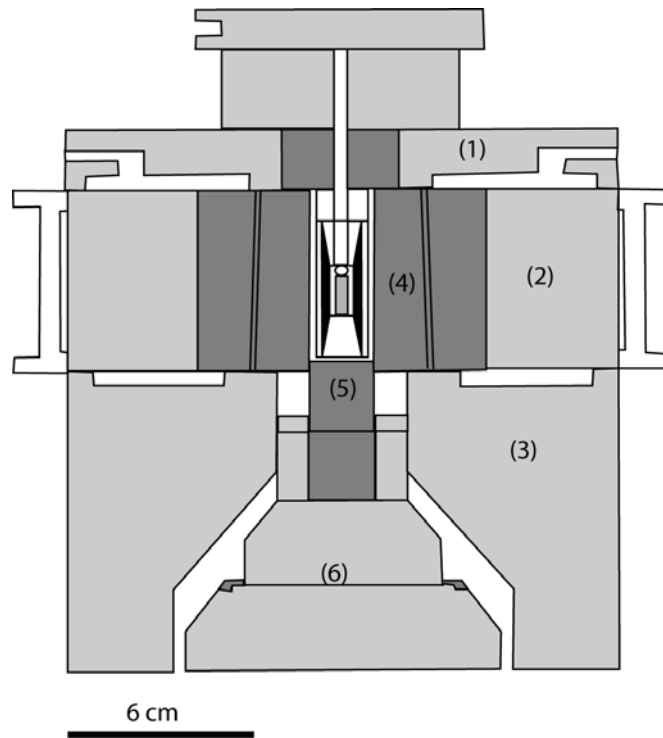


**Figure 2.1.** Principle of a piston-cylinder apparatus (redrawn from Rauch, 2000).

- (1) Top plate
- (2) Bomb (pressure vessel)
- (3) Bridge
- (4) Tungsten carbide core with sample cell
- (5) Tungsten carbide piston
- (6) Pusher assembly

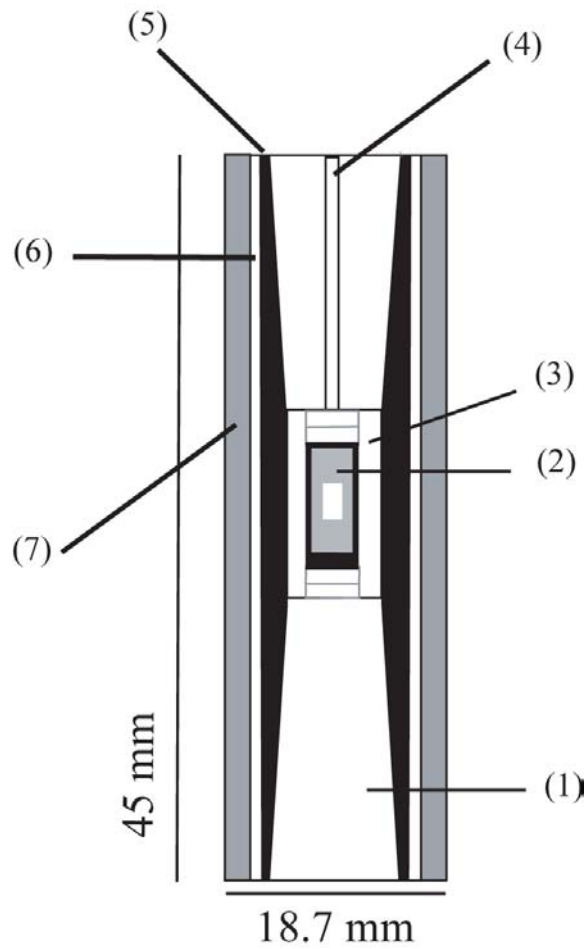


**Figure 2.2.** Details of the piston-cylinder talc-Pyrex<sup>TM</sup> cell assembly.

- (1) Alumina plug
- (2) Capsule with sample
- (3) Pyrophyllite or alumina cylinder
- (4) Hole for the thermocouple
- (5) Tapered graphite furnace
- (6) Pyrex glass cylinder
- (7) Talc or NaCl cylinder

### 2.3.2. TZM rapid-quench cold-seal vessel

A TZM rapid-quench cold seal-vessel is an autoclave where the vessel is made of titanium-zirconium-molybdenum (TZM) alloy (composed of  $\text{Ti}_{0.5\%}\text{Zr}_{0.08\%}\text{C}_{0.02\%}\text{Mo}_{99.4\%}$ ; Williams, 1968) and on which a gravitational rapid-quench system was added. This system permits a quench in 1-2 seconds using an external magnet ring. Argon is used as the pressure medium. The details of this apparatus are shown in Figure 2.3. The hydration experiments in TZM cold-seal vessels were carried out at  $0.2 \pm 0.005$  GPa (error from Rauch, 2000), and temperatures between  $900 \pm 10$  and  $1100 \pm 10^\circ\text{C}$  for experimental durations between 1 and 20 hours ( $\pm 30$  second). The furnace was previously calibrated (up to  $1400^\circ\text{C}$ ) by referencing the furnace thermocouple to an inner NiCr-Ni thermocouple at the sample site. The temperature gradient around the hot spot is  $\sim 30^\circ\text{C}$  per cm. The capsules in these experiments were made of pure platinum of  $\sim 2$  cm in length, 0.5 cm in diameter with a wall thickness of 0.1 mm, The contents of the capsule are similar to those for the piston-cylinder runs (section 2.3.1) except that more water was added: 20  $\mu\text{l}$  of free water.

Before the experiment, the vessel was inserted into the furnace with the top located within the hot spot. Subsequently argon was compressed in the TZM vessel and the furnace was heated to the desired temperature. When the experimental conditions were attained, the capsule was pushed to the hot spot within the vessel using the mobile magnetic sample holder (label 9 and 10 in Figure 2.3). At the end of the experiment, the external magnet ring (label 10 in Figure 2.3) was dropped very quickly, allowing the capsule to fall into the water-cooled Cu-Be sealing plug (label 5 in Figure 2.3). The cooling rate was around  $500^\circ\text{C/s}$  (Holloway et al., 1992) and the pressure was released in 1-2 hours.

As diffusion is very sensitive to temperature, the position of the hot spot in the furnace was checked very often (after each 4 experiments, or after each explosion) and the length of the sample holder was, for each run, adjusted as a function of the length of the sample capsule (1.6-2.0 cm, varying with the weld thickness) to be sure that the capsule is perfectly located in the hot spot.

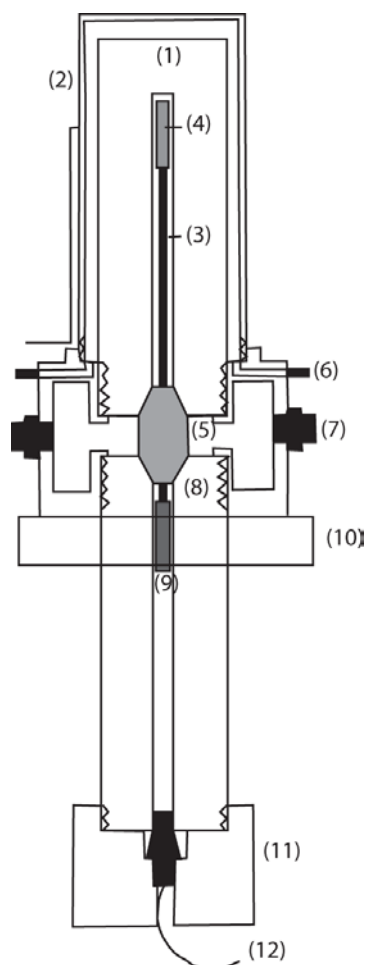


**Figure 2.3** Details of the TZM cold seal-vessel.

(Redrawn from Rauch, 2000).

- (1) Pressure vessel
- (2) Shield
- (3) Sample holder
- (4) Sample capsule
- (5) Copper-beryllium sealing plug
- (6) Argon flow to prevent oxidation
- (7) Cooling-water connection
- (8) Pressure vessel
- (9) Magnetic end of the sample holder
- (10) External magnet ring
- (11) Closure plug
- (12) Argon gas connection for pressure

### 2.3.3. Multi-anvil apparatus

A 1000-ton multi-anvil apparatus (Hymag) was used to study the water solubility in wadsleyite. This multi-anvil apparatus allows experiments at high-temperature (up to 2500°C) and high-pressure using a hydraulic system (up to 25 GPa = 250 kbar). The compression system and details of experimental procedure are given in Rubie (1999). A schematic view of the multi-anvil compression system is shown in Figure. 2.4 Two types of assembly were used: 14/8 and 10/5 (where these numbers refer to the ratio TEL/OEL = truncation edge length/octahedral edge length) to achieve the run pressure ranges of 14-16 GPa and 17-18 GPa, respectively. Two series of experiments were carried out. The first series was run at a constant pressure ( $15 \pm 1$  GPa) and at various temperatures from 900°C up to 1400°C. The second series was performed at constant temperature (1200°C) and various pressures from  $14 \pm 1$  GPa up to  $18 \pm 1$

GPa, where a 10/5 assembly is necessary. The heating duration is the same for every run: 5 hours ( $\pm 2$  min). The mixture of powder ( $\text{Mg}_2\text{SiO}_4 + 5 \text{ wt\% H}_2\text{O}$ ) was welded in pure platinum capsules (for the 14/8 assembly: 2.7 mm length, 1.6/1.4 mm outer/inner diameter ; for the 10/5 assembly: 2.2 mm length, 1.6/1.4 mm outer/inner diameter). The capsule was placed inside an octahedron of MgO doped with 5 %  $\text{Cr}_2\text{O}_3$  to reduce heat loss by radiation. The capsule was surrounded by a  $\text{LaCrO}_3$  furnace, a MgO cylinder and a zirconia cylinder in contact with the octahedron as shown in the Figure 2.5. The temperature was monitored using a  $\text{W}_{3\%}\text{Re} - \text{W}_{25\%}\text{Re}$  thermocouple (no corrections for the effect of pressure on the temperature EMF were applied) placed across an alumina tube in contact with the platinum capsule. To prevent the thermocouple puncturing the capsule, a disc of Re was added between the thermocouple and the top of the capsule.

The pressure calibration method for the same multi-anvil apparatus (Hymag press at BGI) was described by Bolfan-Casanova (2000) for the 14/8 assembly and by Canil (1994) for the 10/5 assembly.

Special attention was given to the ratio of temperature to output power during the experiment. The temperature was controlled manually and the runs were considered successful when the output power did not increase more than 5% from the beginning to the end of the experiment. Under these criteria, one can assume that no migration of the thermocouple or collapse of the capsule occurred and that the temperature given by the thermocouple is the actual temperature at the top of the capsule. However, such multi-anvil assemblies do have a much larger thermal gradient (50-100°C/mm) than piston-cylinder and TZM cold-seal vessels.

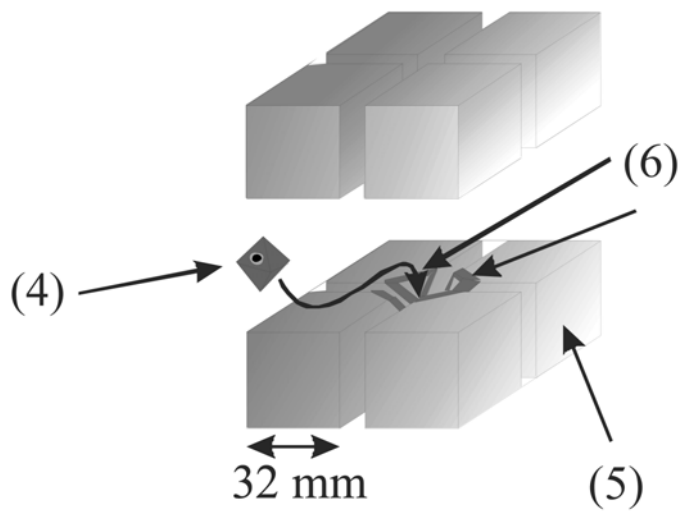
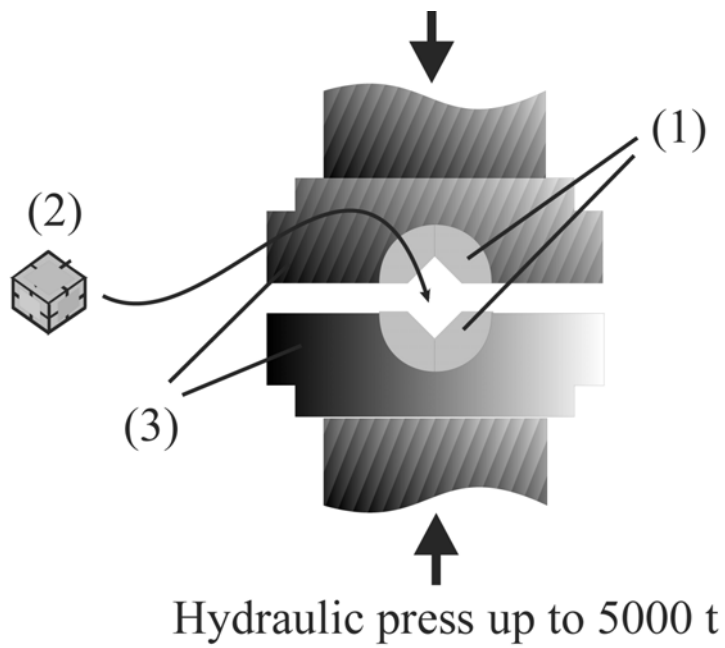


**Figure 2.4** Details of the multi-anvil apparatus (redrawn from Rubie, 1999)

- (1) 6 outer steel anvils
- (2) 8 inner tungsten carbide anvils
- (3) Steel guide blocks
- (4) MgO pressure medium with sample assembly
- (5) Tungsten carbide anvils
- (6) Pyrophyllite gaskets

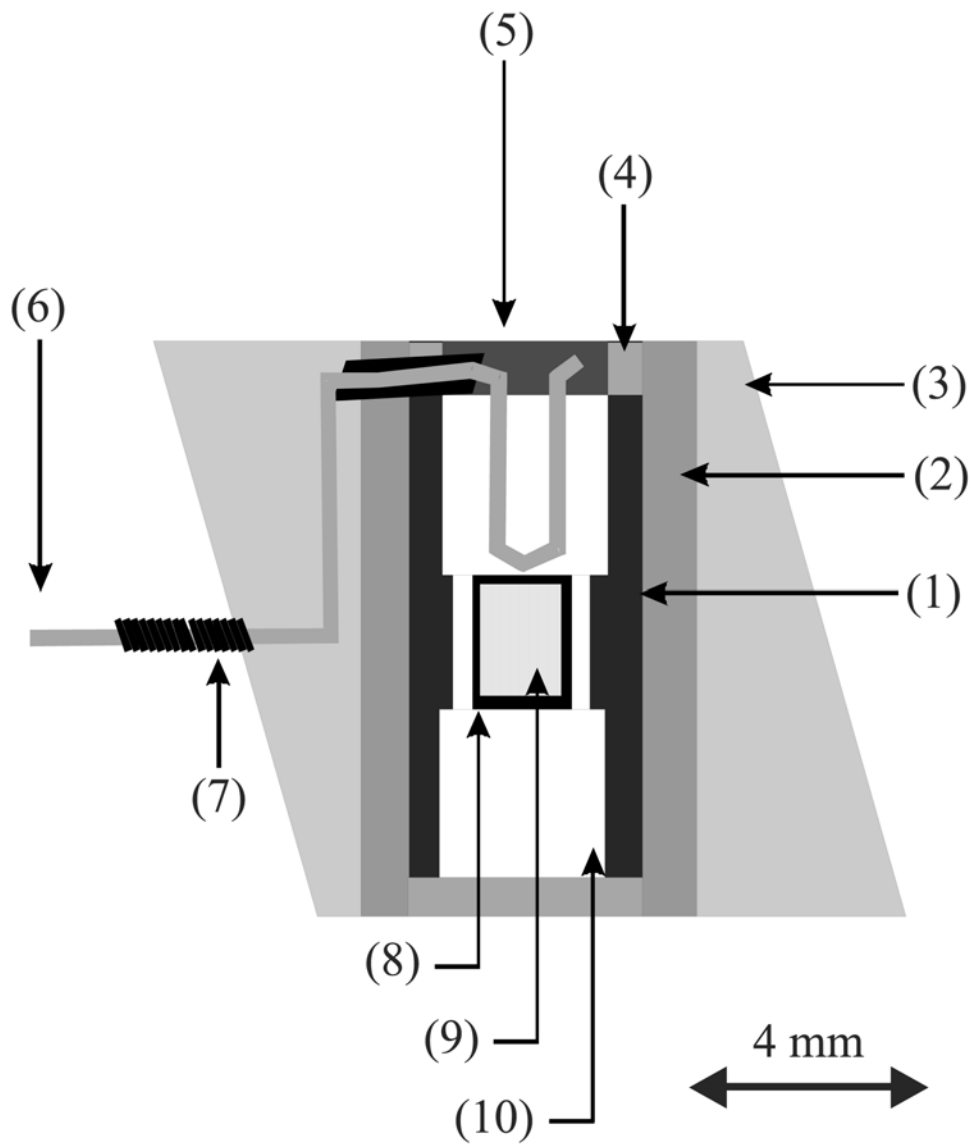


**Figure 2.5** Details of the 14/8 multi-anvil assembly

- (1) LaCrO<sub>3</sub> heater
- (2) Zirconia
- (3) MgO doped with 5% CrCO<sub>3</sub>
- (4) Molybdenum
- (5) Pyrophyllite
- (6) Thermocouple
- (7) Copper coil
- (8) Pt capsule covered by Re disc
- (9) Sample powder mixture
- (10) MgO

## 2.4. Infrared analysis

### 2.4.1. Spectrometer and measurement parameters

The hydroxyl distribution within the samples was analyzed with polarized Fourier transform infrared (FTIR) spectroscopy using a Bruker<sup>TM</sup> IFS 120 HR high-resolution FTIR spectrometer coupled with a Bruker<sup>TM</sup> IR microscope.

Technical details of the design of Fourier transform infrared spectrometers based on the Michelson interferometer are given in Siesler et al. (2002).

The FTIR microscope (Figure 2.6.) contains all-reflecting Cassegranian optics and is equipped with a metal–strip polarizer on a KRS-5 substrate. Analyses in the microscope were made at room temperature and pressure, under a stream of H<sub>2</sub>O- and CO<sub>2</sub>-free purified air. Near infrared (NIR) measurements were performed using a tungsten light source, a Si coated CaF<sub>2</sub> beam splitter and a high-sensitivity narrow-band MCT (mercury-cadmium-telluride) detector cooled by liquid nitrogen. Only infrared spectra of natural olivine and pyroxenes from Pali-Aike were acquired using unpolarized infrared radiation; all other spectra were obtained using polarized infrared radiation. The principal advantages of the microscope coupled to the FTIR are that:

- It is easy to observe the sample spot optically before the measurement,
- The focused IR beam yields higher intensities than a measurement in the sample chamber of the spectrometer.
- The detector placed over the microscope is optimized for a focused beam.

The infrared beam was focused in the middle of the sample using a 1.5 mm aperture, which generates a spot size of 100  $\mu\text{m}$  in the focal plane. Two hundred scans

were accumulated for each spectrum at a resolution of  $1\text{ cm}^{-1}$ . Due to the divergence of the infrared beam, the associated spot size on the surface of a 1 mm thick sample, is around  $600\text{ }\mu\text{m}$ . In order to increase spatial resolution parallel to the diffusion direction, an aluminum mask fixed to the objective lens of the microscope was used to reduce the angle of incidence from  $30^\circ$  to  $10^\circ$ , yielding a spot size at the sample surface of around  $270\text{ }\mu\text{m}$  parallel to the direction of diffusion (Figure 2.7).

Each sample was characterized by taking spectra with the electric vector (or electric field vector),  $E$  parallel to each crystallographic axis. Water contents were calculated from polarized spectra (Bell et al., 2003). Hydroxyl profiles were measured for diffusion parallel to the  $[100]$ ,  $[010]$  and  $[001]$  crystallographic axes, with  $E$  parallel to  $[001]$ . Spectra were collected at a spacing of  $30\text{-}50\text{ }\mu\text{m}$  near the edges of the sample and  $100\text{-}300\text{ }\mu\text{m}$  near the center of the sample (Figure 2.8.).

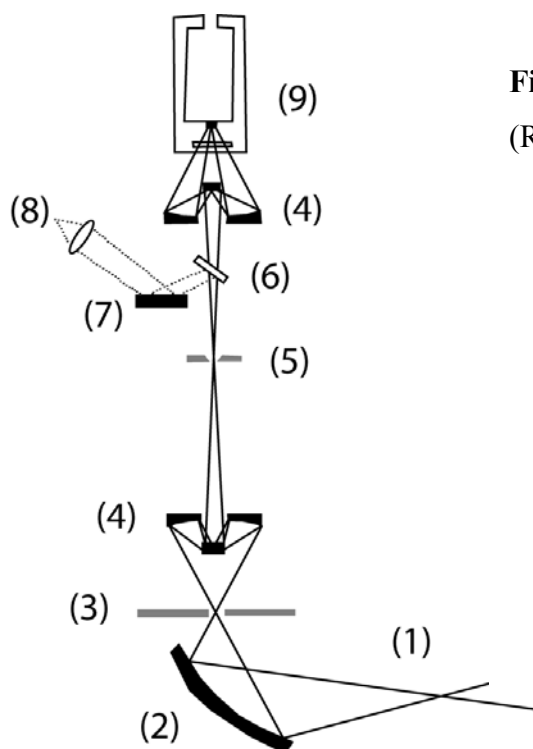


**Figure 2.6** Details of the FTIR microscope (Redraw from Bolfan-Casanova, 2000).

1. IR beam in transmission mode
2. Condensor mirror
3. Sample holder
4. Cassegrainian objective
5. Aperture
6. Moving mirror
7. Mirror
8. Ocular
9. MCT detector

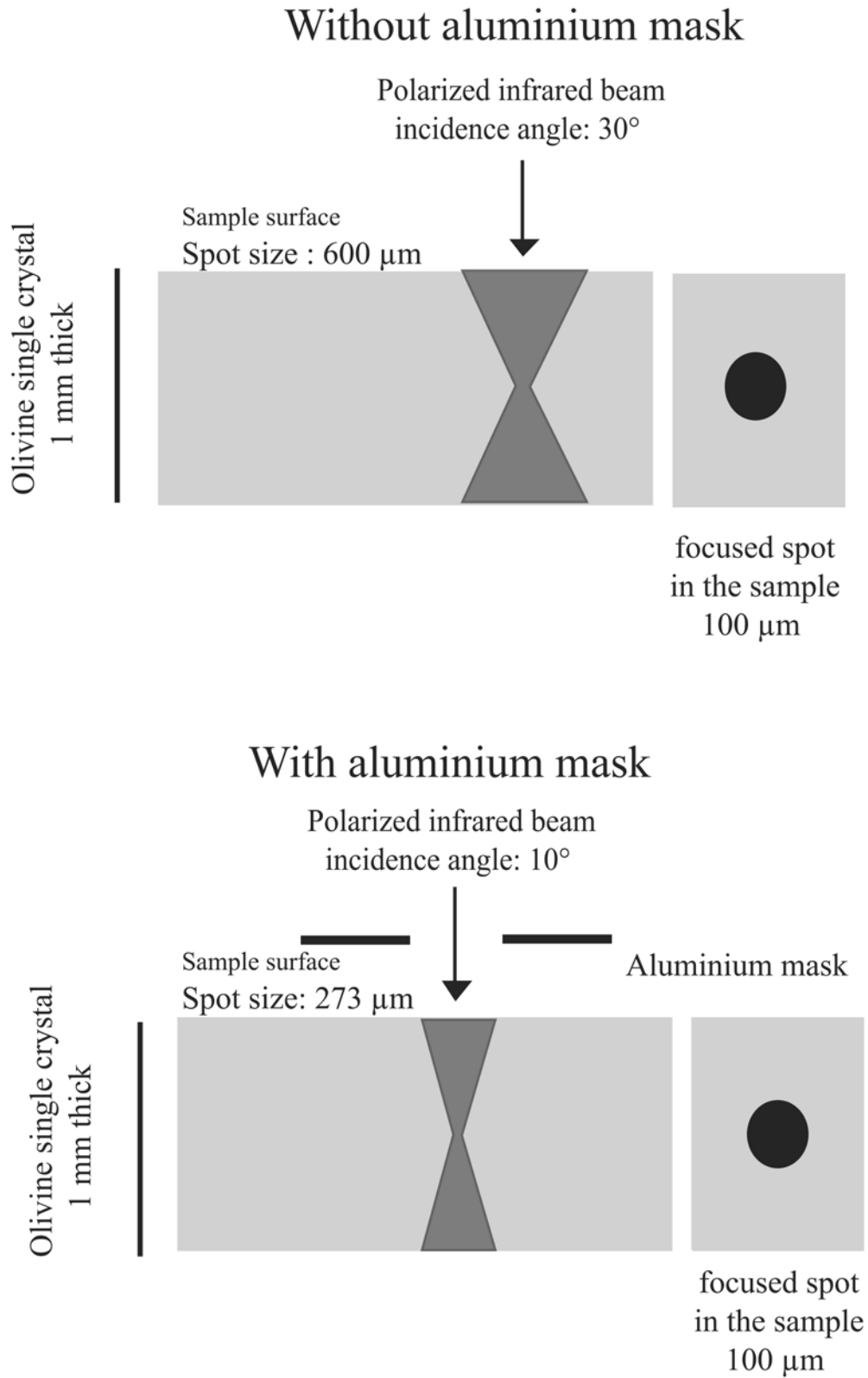


**Figure 2.7** Details of the IR measurement with or without the use of the aluminum mask.

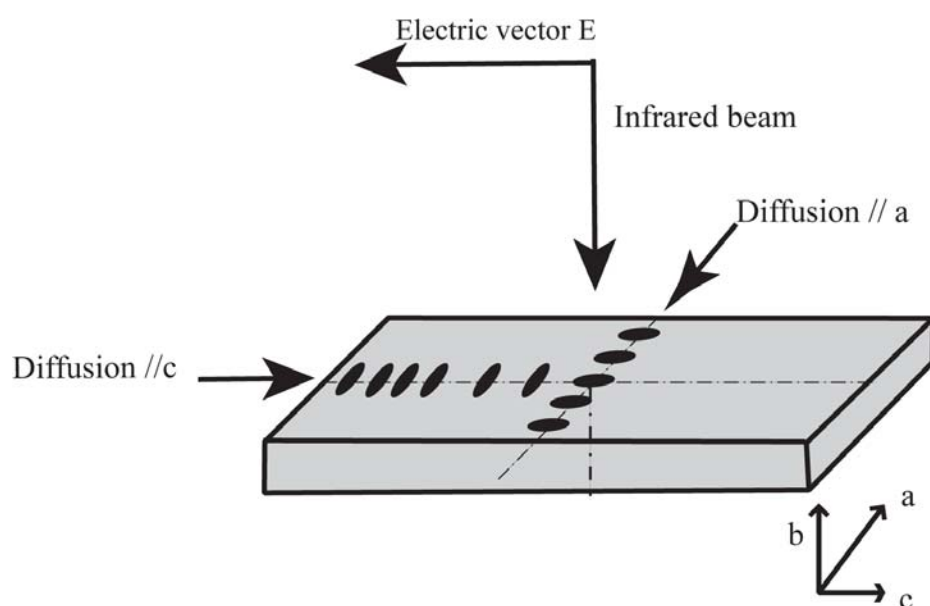


**Figure 2.8** Principle of a profile measurement across a doubly polished and oriented single crystal plate. The sample is oriented with the electric vector  $E$  parallel to the  $[001]$  (or  $\underline{c}$ ) axis. The polarized infrared beam is parallel to the  $[010]$  (or  $\underline{b}$ ) axis. Two profiles can be measured parallel to  $[001]$  (or  $\underline{c}$ ) and  $[100]$  (or  $\underline{a}$ ) axes with  $E$  parallel to  $[001]$  (or  $\underline{c}$ ).

### 2.4.2 Calculation of the water contents using infrared spectroscopy

The measurement of water content by IR is based on the Beer-Lambert's law:

$$A = c \varepsilon t$$

Eq. 5

Where  $c$  is the concentration of the absorber, in mol/L

$A$  is the absorbance,

$\varepsilon$  is the molar extinction coefficient, in  $\text{cm}^{-1}/(\text{mol/L})$

$t$  is the sample thickness, in cm.

This equation can also be written as:

$$c = \frac{K}{\varepsilon} \quad \text{Eq. 6}$$

where,  $K = A/t$  is the absorption coefficient at the wavenumber ( $\nu$ ) per cm.

To quantify water content the extinction coefficients for the mineral,  $\varepsilon$ , must be known since  $\varepsilon$  is matrix dependent. These extinction coefficients are determined by calibration of the infrared data with an independent analytical method for hydrogen measurements such as

- Karl-Fischer-titration,
- Gas extraction manometry,
- $^1\text{H}$  MAS NMR (Magic-Angle-Spinning Nuclear Magnetic Resonance),
- SIMS (Secondary Ion Mass Spectroscopy),
- Nuclear reaction analysis (using the reaction of 6.4 MeV  $^{15}\text{N}$  ions with hydrogen in the mineral).

The approach used here for determining the water content from polarized IR spectra in olivine or forsterite samples is based on the calibration recently presented by Bell et al. (2003). They used  $^{15}\text{N}$  nuclear reaction analysis on three natural olivine crystals in order to calibrate the extinction coefficient of OH in olivine.

$$C_{\text{H}_2\text{O}} = Abs_{tot} / I \quad \text{Eq. 7}$$

with,

$$Abs_{tot} = \frac{1}{t_a} \int_{\nu_1}^{\nu_2} A_a \, d\nu + \frac{1}{t_b} \int_{\nu_1}^{\nu_2} A_b \, d\nu + \frac{1}{t_c} \int_{\nu_1}^{\nu_2} A_c \, d\nu \quad \text{Eq. 8}$$

where,

- $C_{\text{H}_2\text{O}}$  is the concentration of hydroxyl expressed as  $\text{H}_2\text{O}$  in the unit moles/liter of olivine,
- $A_{\text{tot}}(\nu)$  is the total absorption coefficient at wavenumber  $\nu$ ,
- $I$  is the integral extinction coefficient. Here assumed to be  $5.32 \text{ cm}^{-2}$  per wt ppm  $\text{H}_2\text{O}$ , (Bell et al., 2003),
- $A_i$  is the integrated absorbance with the electric vector  $E$  parallel to  $i$  (a, b or c) axis,
- $t_i$  is the plate thickness (in cm) perpendicular to the relative crystallographic axis and parallel to the beam direction.
- $\nu_1$ - $\nu_2$ , is the integral wavenumber range:  $3050$ - $3650 \text{ cm}^{-1}$ .

In this work, the total water content for each sample is determined by summing the concentrations for  $E$  parallel to the three crystallographic axes. However, because only the relative decrease in water content along each crystallographic axis is required to determine the diffusion coefficient and on the assumption that the total water content is proportional to the water content measured with  $E$  parallel to the  $[001]$  axis, the water content plotted in diffusion profiles corresponds, to the integrated absorbance with  $E$  parallel to the  $c$  axis,  $A_c$  alone. Thus,

$$C_{\text{H}_2\text{O}} = \frac{1}{I} \int k_c(\nu) d\nu \quad \text{Eq. 9}$$

When it was not possible to performed polarized infrared analysis (*i.e.* on unoriented olivine crystals from Pali-Aike xenoliths), the calibration of Paterson (1982) was used. This calibration is commonly chosen in the absence of specific calibrations for a given mineral (Bolfan-Casanova, 2000; Rauch, 2000). The calibration of Paterson may underestimate the water content in some minerals (Libowitzky and Rossman, 1996). It is based on an empirical correlation between the OH stretching frequency and the extinction coefficient, which leads to the following expression:

$$C_{\text{OH}} = \frac{X_i}{150\xi} \int \frac{k(\nu)}{3780 - \nu} d\nu \quad \text{Eq. 10}$$

where  $C_{\text{OH}}$  is the concentration of hydroxyl (in H/10<sup>6</sup>Si),

$\xi$  is an orientation factor, equal to 1/3 for unpolarized measurement,

$K(\nu)$  is the absorption coefficient (in cm<sup>-1</sup>) for a given wavenumber  $\nu$ .

$X_i$  is a density factor. Its value is chemical composition dependent.

$X_i = 4.39 \cdot 10^4$  H/10<sup>6</sup>Si or 2695 wt ppm H<sub>2</sub>O for olivine (Fo<sub>90</sub>)

$X_i = 4.366 \cdot 10^4$  H/10<sup>6</sup>Si or 2793 wt ppm H<sub>2</sub>O for forsterite (Fo<sub>100</sub>)

$X_i = 6.707 \cdot 10^4$  H/10<sup>6</sup>Si or 2769 wt ppm H<sub>2</sub>O for Cr-diopside

$X_i = 6.706 \cdot 10^4$  H/10<sup>6</sup>Si or 2727 wt ppm H<sub>2</sub>O for enstatite

(the unit of  $X_i$  defines the unit of the water content in H/10<sup>6</sup>Si or wt ppm H<sub>2</sub>O)

The reliability of the various calibrations is still being discussed (Paterson, 1982; Bell et al, 1995; Libowitzky and Rossman, 1997; Bell et al, 2003). However, the choice of infrared calibration does not affect the calculated diffusivities (Kohlstedt and Mackwell, 1998).

## 2.5. Secondary ion mass spectrometry

Secondary Ion Mass Spectrometry (SIMS) was used to quantify the water content in wadsleyite because the water content of wadsleyite is too high for infrared analysis. The advantage of the SIMS is that the analyzed portion of the crystal is smaller than with infrared and that quantification of water is possible for very hydrated silicates. The disadvantage is that the analysis is destructive (sputtering), sensitive to the vacuum quality (hydrogen pollution from air) and also very sensitive to hydrated sub-microscopic inclusions in the crystal.

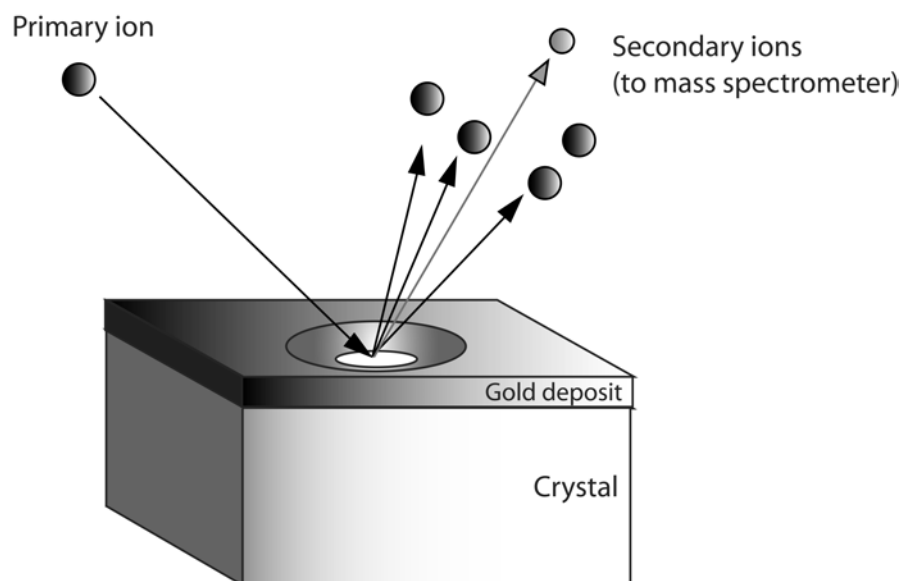


**Figure 2.9** Principle of SIMS with sputtering.

### *Principle*

A beam of primary ions with moderate energy ( $\sim 1\text{-}15$  keV; in general  $\text{O}^-$ ,  $\text{O}^{2+}$ ,  $\text{O}^{2-}$ ,  $\text{Cs}^+$  or  $\text{Ar}^+$  ion source) is used to bombard the sample surface and to remove material by sputtering. A fraction of the sputtered material consists of positive and negative ions, which are referred to as secondary ions (Figure 2.9). The secondary ions are sent into a mass spectrometer where they are analyzed according to their mass-to-charge ratio. SIMS analyses were performed using an ion probe Cameca IMS-1270 instrument (large radius magnetic sector SIMS for geology) at Centre de Recherches Pétrologiques et Géochimiques (CRPG, France) under the direction of Dr. Etienne Deloule. A primary beam of  $\text{O}^-$  ions was used with a current of 4-6 nA (Duoplasmatron source) with a beam diameter  $\sim 20$   $\mu\text{m}$ . The positive secondary beam was centered in a 50  $\mu\text{m}$  image field aperture. The voltage offset was stable at -100 eV and the energy window was fixed at 40 eV. The positive secondary ions of  $^1\text{H}$ ,  $^7\text{Li}$ ,  $^{11}\text{B}$ ,  $^{29}\text{Si}$ , and  $^{30}\text{Si}$  were measured in mono-collection mode. Li and B were measured to check the surface pollution during sample preparation.. For more details, see Deloule et al. (1991, 1995).

A high-quality vacuum in the IMS-1270 ( $2\text{-}4 \cdot 10^{-9}$  torr) and the monocollection mode permit increase in sensitivity of the analysis compare to a SIMS Cameca 3f. Instrumental bias was monitored by checking the  $^{29}\text{Si}/^{30}\text{Si}$  isotope ratio. A schematic picture of the exterior of an ion probe is shown in Figure 2.10.

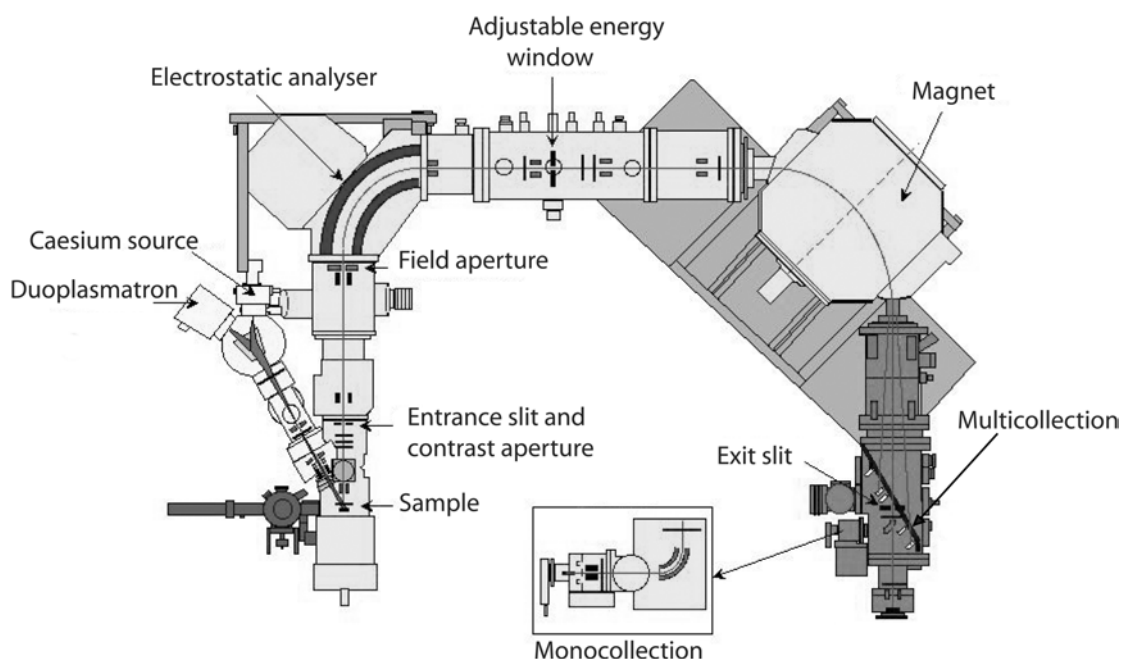


**Figure 2.10** Schematic of the Cameca IMS 1270 (*modified from a Cameca document, courtesy of CRPG - Dr. E. Deloule*-).

### *Sample preparation for SIMS*

Prior the measurement, the glue was removed from the capsule sections in an acetone bath prior to mounting the capsule sections on small cylinders of steel with a very small amount of superglue (cynolite<sup>TM</sup>). Four of these cylinders fit into a classical sample holder of 1-inch diameter. Following to Hauri et al. (2002) and Koga et al. (2003), the use of epoxy was strictly avoided because epoxy degasses in ultra-high vacuum, which contributes to a misrepresentation of the hydrogen background and influences the calibration. The sample holder and sample were afterwards coated with pure gold (100 Å thick). After analysis, the gold coat is removed by wiping with a tissue. Optical microscopy was used to check the sputtering crater in order to control the quality of the analyzed wadsleyite crystal. Afterwards EMPA was performed on the same crystal to obtain the corresponding bulk chemical composition.

*Calibration for H measurements in silicate*

Hydrogen contents were quantified by calibration with natural hydrous and anhydrous silicate minerals and glasses (Table 2.5). Because wadsleyite is water rich compared to other nominally anhydrous minerals of the upper mantle, hydrous glass standards were used.

**Table 2.5** SIMS standards used for water calibration in wadsleyite.

Standard	Description	Water content wt% H <sub>2</sub> O	Ref.
Alv 1833-11	Basaltic glass	1.17	Stolper and Newman, 1994
MC-84df	Obsidian glass	0.67	Newman et al, 1988
Wok 28-3	Basaltic glass	0.49	Stolper and Newman, 1994
NW coulee	Obsidian glass	0.29	Newman et al, 1988
NSH 12	Orthopyroxene	0.18	Bell et al, 1995
Panum Dome	Obsidian glass	0.11	Newman et al, 1988

For measuring water, the intensity of the ratio  $^1\text{H}/^{30}\text{Si}$  was calibrated against the  $\text{H}_2\text{O}/\text{SiO}_2$  wt% ratio. After electron microprobe analysis, which gives the  $\text{SiO}_2$  wt% for every wadsleyite crystal, the water content was obtained from the calibration curve. Measurements of the standards for calibration were always performed prior and after the measurements on a group of wadsleyite samples. This technique allows an assessment of the time effect on the vacuum of the instrument. Calibration curves are shown in Figure 2.11. Standard measurements were performed prior to each set of wadsleyite samples to increase analytical accuracy. Two groups of analyses were carried out (Group 1: SIMS standards followed by H2050, H2053, H2054 and H2058, and Group 2: SIMS standards followed by H2011, H2039, H2044, H2045, H2059, H2060, H2061 and H2065).

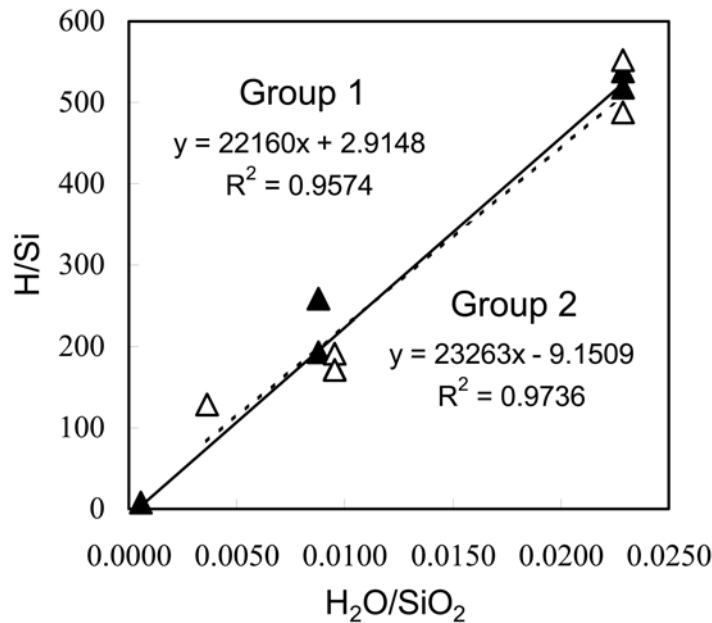


**Figure 2.11** Diagram showing H/Si (SIMS counts) versus H<sub>2</sub>O/SiO<sub>2</sub> (wt% from EMPA analysis) for SIMS calibration group 1 and 2. the *open triangle* SIMS standards group 1, the *closed triangle* SIMS standards group 2. The *dashed line* represents the calibration for group 1 and the *solid line* represents the calibration for group 2. Regressions parameters for these SIMS calibration curves are indicated on the plot.

## 2.6. Transmission electron microscopy

Transmission electron microscope (TEM) observations were performed in collaboration with PD Dr. Falko Langenhorst using a FEG TEM (200kV) on mantle-derived olivine PA-5 from Pali-Aike and on forsterite sample Fo2-10 after the hydration experiment to check whether these samples contained boron-rich precipitates, hydrous defect layers (e.g., humite lamellae, Miller et al., 1987), high dislocation densities, or melt pockets (e.g., the early partial melting phenomenon of Raterron et al., 2000). Selected area diffraction and observations in high resolution TEM were carried out in the hydrated regions as well as in the anhydrous part.

### 3. Analysis of diffusion

Diffusion is the process of matter transport (atoms, ions or molecules) from one part of a system to another one in response to chemical potential gradient. In the following sections, the basics concepts of diffusion will be discussed here.

#### 3.1. Theory of diffusion – Fick’s laws -

There is an obvious analogy between diffusion and heat transfer by conduction. This was recognized by Fick (1855), who applied to diffusion the mathematical equation of heat conduction derived by Fourier. Fick’s mathematical theory for diffusion into an isotropic medium is therefore based on the hypothesis that there is proportionality between the flux of diffusing species and the gradient of concentration. This relationship is referred to as “Fick’s first law”, and is written for diffusion in one dimension as:

$$J = -D \frac{\partial C}{\partial x} \quad \text{Eq. 11}$$

where  $J$  is the flux of diffusing species through a unit cross sectional area per unit time,  $D$  is the diffusion coefficient of mobile species for a given system,  $C$  is the species concentration, which varies in space and time.

In this study, the diffusion coefficient of hydrogen is assumed to be independent of the hydrous defect concentration in the  $(\text{Mg,Fe})_2\text{SiO}_4$  lattice, since previous work has shown a good correlation between observed and theoretical hydrogen diffusivities based on this assumption (Mackwell and Kohlstedt, 1990; Ingrin et al., 1995; Kohlstedt and Mackwell, 1998; Carpenter-Wood et al., 2000).

The flux of the diffusing species changes with position  $x$ , and because of the conservation of matter one obtain the following relation for diffusion in one-dimension.

$$\frac{\partial J}{\partial x} = - \frac{\partial C}{\partial t} \quad \text{Eq. 12}$$

By combining Eq. 11 and Eq. 12, the general equation of diffusion, “ Fick’s second law”, is obtained for diffusion with a constant diffusion coefficient

$$\frac{\partial C}{\partial t} = D \frac{\partial^2 C}{\partial x^2} \quad \text{Eq. 13}$$

For one-dimensional diffusion occurring in a finite medium, the solution of Eq. 12 involves a finite integral over  $x$  and  $t$ . These solutions frequently involve the error function:

$$\text{erf}(\xi) = \frac{2}{\sqrt{\pi}} \int_0^{\xi} \exp(-\eta^2) d\eta \quad \text{Eq. 14}$$

$$\text{where } \xi = \frac{x}{2\sqrt{Dt}}. \quad \text{Eq. 15}$$

(see Carslaw and Jaeger, 1959 ; p. 485, for tabulated values of this error function )

### **3.2. Diffusion in one dimension within a finite slab from an infinite source**

Appropriate solutions to Fick’s second law depend on the initial and final conditions and on the physical parameters of the system under consideration (Schmalzried, 1981). Our olivine and forsterite samples are prepared as rectangular prisms with roughly the same dimensions for the faces, which were cut perpendicular

to each crystallographic axis. Thus, the model for a finite plate solution for one direction of diffusion is used, assuming that there is no significant component due to other diffusion directions. We also suppose that the reservoir of diffusing species (the free water in the capsule) is an infinite source in intimate contact with the sample surface.

The corresponding solution to Fick's law relating concentration and time can be approximated as the summation of diffusion into a semi-finite medium from opposite sides and is given by (Carslaw and Jaeger, 1959: p. 51),

$$C_{OH}(x) = C_0 \left( \operatorname{erfc} \frac{x}{\sqrt{\tilde{D}_i t}} + \operatorname{erfc} \frac{X - x}{\sqrt{\tilde{D}_i t}} \right) \quad \text{Eq. 16}$$

where  $C_{OH}(x)$  is the hydroxyl concentration at a distance  $x$  from the first sample edge,

$X$  is the width of the sample,

$t$  is time,

$\operatorname{erfc}$  is the complementary error function =  $1 - \operatorname{erf}$ ,

$C_0$  is the observed maximum hydroxyl content,

$\tilde{D}_i$  is the chemical diffusivity for the mobile species parallel to  $i = [100]$ ,  $[010]$  or  $[001]$  under the experimental conditions.

This relationship is valid if the profile from each side does not overlap significantly. A full treatment for diffusion into a finite slab is given in Carslaw and Jaeger (1959, p. 96) or by Schmalzried (1981, p. 84).

### 3.3. Mechanisms of diffusion

In an ideal crystalline solid, chemical reactions and mass transfer can occur only because these solids contain imperfections in the structure that permit mobility of

species. Point defects are the major imperfections involved in hydrogen diffusion in the system  $\text{H}_2\text{O} - (\text{Mg, Fe})_2\text{SiO}_4$ .

#### *Diffusion and point defects*

The nature of point defect in complex minerals is not very well understood; the basic concepts come from studies of simple crystals such as NaCl. Two kinds of point defects can occur in crystalline material: *intrinsic* and *extrinsic* point defects. The *extrinsic* point defects result from impurity ions or variations of oxidation state. One of the simplest *intrinsic* defects is a vacant cation site charge balanced by a vacant anion site to maintain the electrical neutrality. Such a combination is called *Schottky defect*. In contrast, the association of an interstitial cation (or anion), which is balancing a cation (or anion) vacancy is called *Frenkel defect*. Schottky and Frenkel defects do not affect stoichiometry.

The diffusion processes may involve other types of point defects. Figure 3.1. presents the elementary diffusion mechanisms in a 2-dimensional lattice. Mechanisms (1) and (2) are direct ion exchanges. Their activation energies are, in both cases, very high. The most probable mechanisms for diffusion involve vacancies (3) or interstitial defects (4, 5) in the crystal structure.

In this study, hydrogen diffusion is assumed to involve polarons (i.e., a polaron is a hole or an electron-deficient site formed in the valence band, when an electron moves from the valence band into the conduction band; Serway et al., 1997). The polaron is a charge carrier and appears as a positive charge  $\text{h}^+$  or  $\text{h}^\bullet$ . Here, the polaron is localized on iron atoms occupying octahedrally coordinated metal cation sites, metal vacancies, and/or silicon vacancies to charge balance the protons.

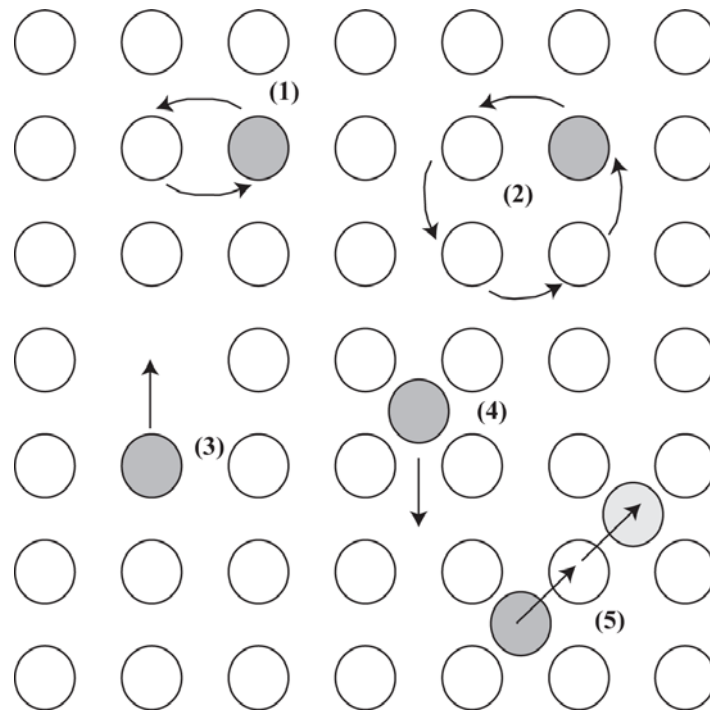


Figure 3. 1. Various atomic mechanisms of diffusion (redrawn from Putnis, 1992).

- (1) and (2) are exchange mechanisms without involving vacancies
- (3) is a vacancy migration mechanism
- (4) and (5) are interstitial migration mechanisms.

*Activation energy*

As diffusion is thermally activated process, it can be described by an Arrhenius law:

$$\tilde{D}_i = \tilde{D}_i^\circ \exp(-Q_i / RT) \tag{Eq. 17}$$

where  $\tilde{D}_i$  is the chemical diffusion coefficient parallel to  $i = [100]$ ,  $[010]$  or  $[001]$ ,  $\tilde{D}_i^0$  is the pre-exponential term,  $Q_i$  is the activation energy for diffusion,  $T$  is the temperature in Kelvin and  $R$  is the gas constant.

Each point defect mechanism has its own activation energy. In certain cases, it may be possible, by comparing experimental values and theoretic models, to identify the point defect mechanism that controls diffusion.

#### 3.4. Ionic diffusion in olivine

Over the past decade, a number of studies have focused on the diffusion of ionic species in silicates (Béjina and Jaoul, 1997), especially olivine (Houlier et al., 1988, 1990; Dohmen et al., 2002). Several approaches have been used. Experimental studies have generally involved two different diffusion processes: ionic self-diffusion and interdiffusion (typically Fe-Mg interdiffusion in olivine), as well as computer simulation (Walker et al., 2003). The diffusion coefficient of a given species is strongly dependent of the chemical composition of the solid. Notably, cation vacancy concentrations vary with trivalent cation content, which is a function of oxygen fugacity. The results of experimental studies to date are not perfectly consistent with each other due to the anisotropy of diffusion. Within anisotropic solids, ionic diffusion measurements must be performed as functions of the crystallographic orientation of the solid. For example oxygen diffusion in diopside is anisotropic, with the  $[010]$  axis the slowest direction of diffusion (Ingrin et al., 2001).

Previous research on ionic diffusion in olivine (Houlier et al., 1988, 1990; Béjina and Jaoul, 1997; Dohmen et al., 2002) has shown that, at 1400°C, the silicon ion is the slowest species to diffuse in olivine ( $\sim 10^{-20}$  m<sup>2</sup>/s) followed by oxygen ( $10^{-18}$  m<sup>2</sup>/s), divalent metal cations (Mg, Fe,  $\sim 10^{-15}$  m<sup>2</sup>/s), and metal vacancies ( $10^{-11}$  m<sup>2</sup>/s). In brief, the self-diffusion of atomic species in olivine is characterized as follows. *Oxygen*: Experimental results (Gérard and Jaoul, 1989, Ryerson, 1989) suggested an interstitial mechanism for oxygen diffusion with a very weak anisotropy such as  $D_{[010]} > D_{[100]} \approx D_{[001]}$ . Recent computer simulations (Walker et al., 2003) suggested that an increase in oxygen fugacity would change the interstitial diffusion to a vacancy

mechanism and that diffusion is isotropic. *Silicon*: According to numerous experimental studies (Anderson et al., 1989; Houlier et al., 1990; Bejina and Jaoul, 1997; Dohmen et al., 2002), silicon is the slowest species to diffuse in olivine or forsterite. The anisotropy of diffusion is a function of the oxygen fugacity with  $D_{[100]} > D_{[010]} > D_{[001]}$  buffered with  $\text{MgSiO}_3$  and  $D_{[010]} > D_{[100]} > D_{[001]}$  buffered with  $\text{MgO}$  (Anderson et al., 1989). Oxygen and silicon self-diffusivities are both lower in forsterite than in iron-bearing olivine (Houlier et al., 1988). *Magnesium*: Chakraborty et al. (1994) have demonstrated a dependency of Mg diffusivity on pressure and oxygen fugacity. The Mg diffusion coefficient decreases with increasing pressure and with decreasing oxygen fugacity. The anisotropy of diffusion is very different from the simulation for oxygen or silicon self-diffusion with  $D_{[001]} > D_{[100]} > D_{[010]}$ . *Iron*: From Nakamura and Schmalzried (1983), it is known that the dominant defects involve changes in Fe redox state and that the Fe point defect population is proportional to  $f\text{O}_2^{1/n}$  where  $n$  varies with pressure and  $a_{\text{SiO}_2}$ . The anisotropy of diffusion is similar to Mg diffusion but at low  $f\text{O}_2$ , the [100] axis was reported to be the fastest direction of diffusion (Jurewicz and Watson, 1988). This is again attributed to a change in the diffusion mechanisms. Hydrogen diffusion mechanisms in olivine are detailed in the next subsection.

### 3.5. Hydrogen diffusion in olivine

Previous experimental studies on olivine indicate that significant amounts of hydroxyl can dissolve within olivine as point defects (Bell and Rossman, 1992, Kohlstedt et al., 1996). Such point defects diffuse in response to changes in the hydrothermal environment (Philibert, 1991).

Mackwell and Kohlstedt (1990) and Kohlstedt and Mackwell (1998, 1999) demonstrated that, in experiments at low temperatures for short experimental durations, hydrogen incorporation occurs by redox exchange of protons with polarons. As the maximum polaron content of olivine (nominally the ferric iron concentration) is on the order of one hundred atomic ppm at low pressure (Nakamura and Schmalzried, 1983; Tsai and Dieckmann, 1997), this process only permits the incorporation of limited concentrations of water-derived species. This phenomenon is

rate limited by proton diffusion and yields proton self diffusivities of around  $10^{-10} \text{m}^2 \text{s}^{-1}$  at  $1000^\circ\text{C}$ ; proton diffusion is also strongly anisotropic with fastest direction of diffusion parallel to  $[100]$  axis (Mackwell and Kohlstedt, 1990).

At higher temperatures and/or longer experimental durations, additional hydrogen is incorporated by a second process that involves defect association of both protons and intrinsic defects, assumed to be metal vacancies by Kohlstedt and Mackwell (1998). In this case, the sample can incorporate more water, up to 135 wt ppm  $\text{H}_2\text{O}$  ( $2,200 \text{ H}/10^6\text{Si}$ ) at 2.5 GPa and  $1100^\circ\text{C}$  (Kohlstedt et al., 1996). The incorporation of hydrogen by this coupled hydrogen-vacancy process occurs at around  $10^{-12} \text{m}^2 \text{s}^{-1}$  in olivine at  $1000^\circ\text{C}$ , with the fastest direction of diffusion parallel to  $[001]$ . As there are essentially no polarons in iron-free olivine, only this second process is expected to occur in end-member forsterite.

- According to Kohlstedt and Mackwell (1998), the chemical diffusivity,  $\tilde{D}_{\text{exch}}$ , for the incorporation of hydrogen by redox exchange is given by

$$\tilde{D}_{\text{exch}} = \frac{2D_{\text{p}}D_{\text{H}}}{D_{\text{p}} + D_{\text{H}}} \quad \text{Eq. 18}$$

where,  $\tilde{D}_{\text{exch}}$  is the chemical diffusivity,  $D_{\text{p}}$  is the polaron diffusivity and  $D_{\text{H}}$  is the proton self-diffusivity. Assuming that  $D_{\text{p}} \gg D_{\text{e}}$  (Schmalzried, 1981), where  $D_{\text{e}}$  is the diffusivity of electrons with  $D_{\text{p}} \gg D_{\text{H}}$  then,

$$\tilde{D}_{\text{exch}} \approx 2D_{\text{H}} \quad \text{Eq. 19}$$

- According to Kohlstedt and Mackwell (1998), the chemical diffusivity for the incorporation of hydrogen linked to metal vacancies is given by

$$\tilde{D} = \frac{3D_{\text{VMe}}D_{\text{H}}}{2D_{\text{VMe}} + D_{\text{H}}} \quad \text{Eq. 20}$$

where  $\tilde{D}$  is the chemical diffusivity measured in the experiments,  $D_{V_{Me}}$  is the diffusivity of metal vacancies and  $D_H$  is the self-diffusivity of protons. On the assumption that  $D_H \gg D_{V_{Me}}$  (Nakamura and Schmalzried, 1983; Kohlstedt and Mackwell, 1998),

$$\tilde{D} \approx 3D_{V_{Me}} \quad \text{Eq. 21}$$

This model of diffusion will apply for end-member forsterite.

### 3. 6. Hydrogen diffusion in a crystalline aggregate

Investigation of the hydrogen distribution within the Pali-Aike olivine crystals involves diffusion in a system with many unknown parameters, such as the exact temperature of the transporting magma, the oxygen fugacity and the water fugacity.

In such a system, each crystal in the xenolith aggregate is considered as a single crystal with anisotropic diffusion occurring along all the directions. The diffusion (in 3 dimensions) can be described by the function  $v(x, y, z)$  (Crank, 1975; Carpenter-Wood, 2001), where the width of the grain in the x direction is  $2a$ , in the y direction  $2b$  and in the z direction  $2c$ :

$$v(x, y, z) = \frac{64}{\pi^3} \sum_{l=0}^{\infty} \sum_{m=0}^{\infty} \sum_{n=0}^{\infty} \frac{(-1)^{l+m+n}}{(2l+1)(2m+1)(2n+1)} \times \\ \cos \frac{(2l+1)\pi x}{2a} \cos \frac{(2m+1)\pi y}{2b} \cos \frac{(2n+1)\pi z}{2c} \times \\ \left[ \exp -\frac{\pi^2 t}{4} \left\{ \frac{D_x (2l+1)^2}{a^2} + \frac{D_y (2m+1)^2}{b^2} + \frac{D_z (2n+1)^2}{c^2} \right\} \right] + C_i \quad \text{Eq.22}$$

Profiles were calculated using Eq. 22 for selected values of  $D_x$ ,  $D_y$ ,  $D_z$  and  $t$  and compared with measured profiles from xenolith grains. The use of the 1-dimensional equation (Eq. 16) can be used to fit hydrogen profiles within grains where the loss profiles are limited to the near-surface regions for all direction of diffusion. However, once diffusion parallel to any one direction penetrates into the

middle of the grain, the full 3-dimensional equation must be used. As an example, Figure 3.2 shows the case for  $D_x = 10^{-12} \text{ m}^2/\text{s}$ ,  $D_y = 10^{-11} \text{ m}^2/\text{s}$ ,  $D_z = 10^{-10} \text{ m}^2/\text{s}$ ,  $t = 1$  hour and with a starting concentration of 100 (arbitrary unit). From Figure 3.2, it is obvious that in a model of diffusion in three-dimensions, the fastest diffusivity is controlling the concentration level observed in the middle of the sample for all directions. In the one-dimension case the plateau indicates the initial concentration even though in the three-dimension model the plateau indicates an intermediate concentration controlled by the fastest diffusivity (in Figure 3.2, by diffusion along the [001] axis). Then, in a one-dimension model, the concentration is overestimated for the slowest direction of diffusion (*i.e.*, [100] and [010] axes).

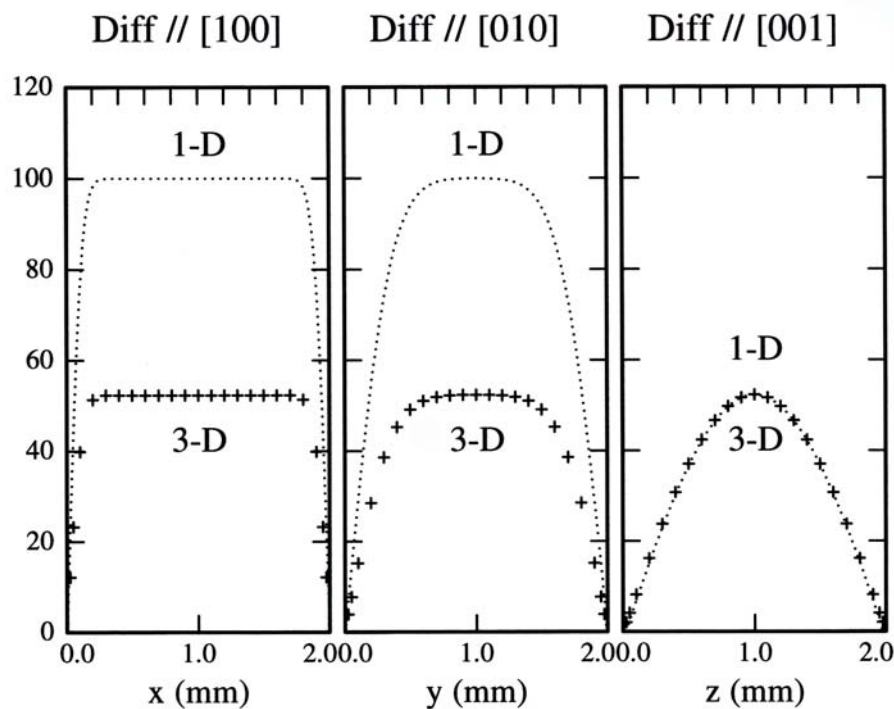


**Figure 3.2** Plot showing differences between **(1-D)** a 1-dimensional diffusion equation (Eq. 16) and **(3-D)** a 3-dimensional diffusion equation (Eq. 22). Starting composition was fixed at 100 (arbitrary unit) and the diffusion coefficients to  $D_x = 10^{-12} \text{ m}^2/\text{s}$ ,  $D_y = 10^{-11} \text{ m}^2/\text{s}$ , and  $D_z = 10^{-10} \text{ m}^2/\text{s}$ . Calculations are shown for a duration of  $t = 1$  hour.

This three-dimension model is used to calculate diffusion profiles (for variable duration), which will be compared to dehydration profiles observed within olivine from Pali-Aike xenoliths.

## 4. Results

### 4.1. Hydrogen diffusion in olivine

#### 4.1.1. Introduction

A small number of experiments were performed on samples of San Carlos olivine, the same material as used by Mackwell and Kohlstedt (1990) and Kohlstedt and Mackwell (1998), to verify their measurements and to provide a direct comparison with the results for iron-free forsterite experiments reported in section 4.2. These experiments were performed using the experimental procedures described in section 2 for hydration of both natural olivine and iron-free forsterite.

#### 4.1.2. Results and discussion

Details of the experimental procedures and analytical techniques are provided in section 2. Table 4.1.1 summarizes the experimental conditions for each run.

**Table 4.1.1** Experimental conditions of hydration for olivine samples.

Sample	Ap.	Temp. °C	P GPa	Time h	Buffer	log $fO_2$	Capsule
SC 32-G	PC	1000	1.5	5 ± 0.01	Ni-NiO	-10.3	Pt <sub>0.95</sub> -Rh <sub>0.05</sub>
SC 32-B	PC	1000	1.5	5 ± 0.01	Ni-NiO	-10.3	Pt <sub>0.95</sub> -Rh <sub>0.05</sub>
SC 33-A	TZM	900	0.2	20 ± 0.01	Ni-NiO	-11.9	Pt
SC 33-B	TZM	900	0.2	1 ± 0.01	Ni-NiO	-11.9	Pt

PC = Piston-cylinder, TZM = titanium-zirconium-molybdenum cold-seal vessel.

log  $fO_2$  calculated according to O'Neill (1987b) for Ni-NiO buffer.

### *Infrared spectra and water solubility*

Figure 4.1.1. shows polarized FTIR spectra for hydrated olivine samples after a short-anneal experiment (SC 33-B, 900°C, 0.2 GPa, 1 hour) and after a long-anneal experiment (SC 33-A, 900°C, 0.2 GPa, 20 hours). Both were hydrated under the same controlled oxygen fugacity along the Ni-NiO buffer. Two groups of infrared bands are distinguishable:

- Group I, at high wavenumbers: from 3616 to 3500  $\text{cm}^{-1}$
- Group II, at lower wavenumbers: from 3500 to 3200  $\text{cm}^{-1}$

With the electric vector (E) parallel to [100], group I is normally the dominant group with respect to band intensity and water content. With E parallel to [010], both groups are reduced in intensity, indicating that the group I bands result in O-H bond mostly subparallel to [100]. With E parallel to [001], group II is the principal group with respect to band intensity and water content. The details of band positions are given in Table 4.1.2. as a function of orientation of E for olivine SC 33-A after hydration at 0.2 GPa, 900°C for 20 hours. Infrared band positions from other olivines are also included for comparison. The olivine sample from Bai and Kohlstedt (1993) was hydrated at 0.3 GPa, 1000°C for 4 hours, under orthopyroxene buffered conditions. The Pamir olivine from Libowitzsky and Beran (1995) is a natural olivine, which contains traces of hydroxyl. In this study, band positions were not observed to change with experiment duration or hydration temperature.

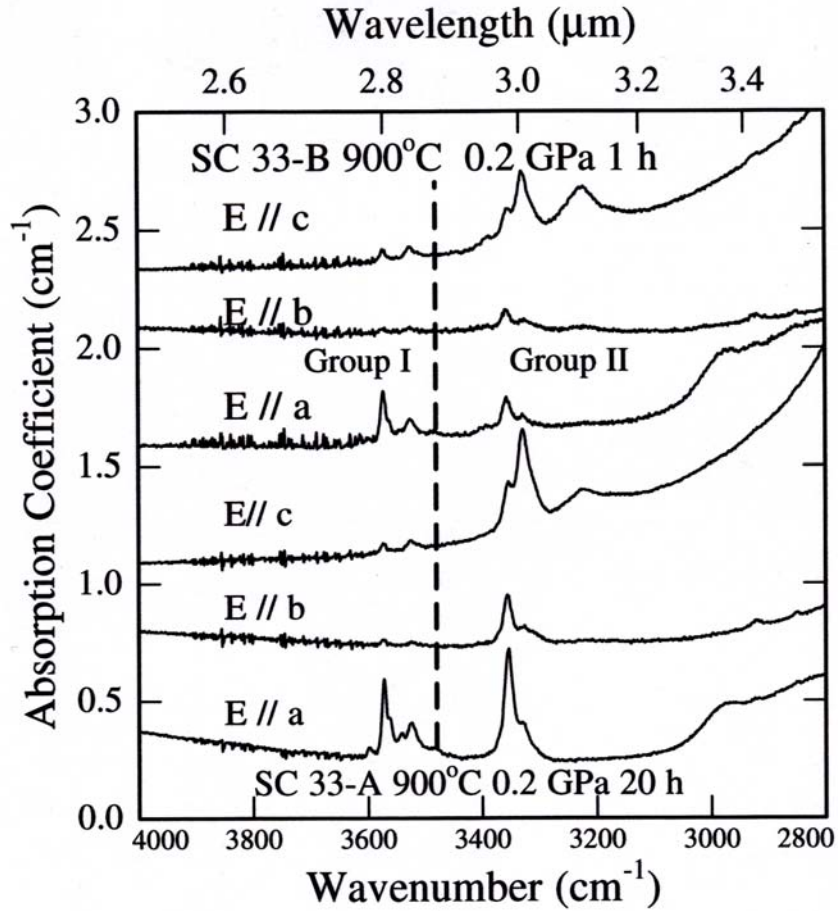


**Figure 4.1.1.** Polarized IR spectra, with different orientations of E, for olivine samples SC 33-A (after an experiment at 900°C, 0.2 GPa, 20 hours duration, buffered by Ni-NiO) and SC 33-B (after an experiment at 900°C, 0.2 GPa, 1 hour duration and buffered by Ni-NiO).

**Table 4.1.2** Hydroxyl band positions for olivine from this study and other iron-bearing olivine from previous investigations (Bai and Kohlstedt, 1993; Libowitzky and Beran, 1995).

SC 33-A <sup>1</sup> ♦			San Carlos olivine <sup>2</sup>	Pamir olivine <sup>3</sup>	
[100]	[010]	[001]	unpolarized	all polarized bands	
				3674	Group I
				3647	
			3637	3640	
			3623	3624	
3616*			3612		
3599			3598	3598	
				3592	
3572	3571*	3571	3576		
				3570	
3563			3565		
3540*			3542		
		3531		3535	
3525	3526*		3529	3524	
				3514	
			3483	3478*	Group II
			3459		
			3443		
			3424		
				3404*	
3352	3355*	3352	3389		
			3354		
				3341*	
3327	3327*	3327	3329		
		3222	3236		
				3215*	

♦ wavenumber resolution  $\pm 2 \text{ cm}^{-1}$

\* indicates a weak infrared band

<sup>1</sup> hydrated San Carlos olivine from this study

<sup>2</sup> hydrated San Carlos olivine (Bai and Kohlstedt, 1993)

<sup>3</sup> natural olivine from skarn deposit in Pamir, Tadzikistan (Libowitzky and Beran, 1995)

The maximum water content of annealed samples presented in Table 4.1.3 were calculated from polarized infrared spectra using the calibration of Bell et al. (2003), and vary from  $10 \pm 1$  wt ppm H<sub>2</sub>O ( $163 \pm 16$  H/10<sup>6</sup>Si, sample SC 33-B) up to  $20 \pm 2$  wt ppm H<sub>2</sub>O ( $327 \pm 33$  H/10<sup>6</sup>Si, sample SC 33-A). These results are comparable to previous hydration experiments in olivine from Mackwell and Kohlstedt (1990).

**Table 4.1.3** Maximum water content of annealed olivine sample and chemical diffusion coefficients along each axis. Water contents were obtained using the calibration of Bell et al., (2003).

Sample	Maximum water content <sup>♦</sup> wt ppm H <sub>2</sub> O (H/10 <sup>6</sup> Si)	$\tilde{D}[100]$ m <sup>2</sup> s <sup>-1</sup>	$\tilde{D}[010]$ m <sup>2</sup> s <sup>-1</sup>	$\tilde{D}[001]$ m <sup>2</sup> s <sup>-1</sup>
SC 32-G* 1000°C	$13 \pm 1$ (212 ± 16)	<i>np</i>	$(3 \pm 1) \cdot 10^{-13}$	<i>np</i>
SC 32-B* 1000°C	$16 \pm 2$ (261 ± 33)	<i>np</i>	$(3 \pm 1) \cdot 10^{-13}$	<i>np</i>
SC 33-A 900°C	$20 \pm 2$ (327 ± 33)	$(1 \pm 1) \cdot 10^{-13}$	$(5 \pm 2) \cdot 10^{-14}$	$(1 \pm 0.5) \cdot 10^{-12}$
SC 33-B 900°C	$10 \pm 1$ (163 ± 16)	$(4 \pm 0.5) \cdot 10^{-11}$	$(2 \pm 1) \cdot 10^{-12}$	$(1 \pm 1) \cdot 10^{-12}$

\* Because of the poor quality of the sample, it was not possible to do infrared analysis with E // [001] so measurements were made with E // [100].

*np* because of the poor quality of the sample, it was not possible to fit a profile.

♦ water content at the rim of the sample using the calibration of Bell et al., (2003).

#### *Diffusion rates and anisotropy*

The chemical diffusivities measured in olivine samples parallel to each axis are shown in Table 4.1.3. Samples resulting from piston-cylinder experiments were too damaged to measure infrared profiles along each crystallographic axis. Figure 4.1.2. presents a series of polarized infrared spectra for sample SC 33-A with E // [001] and diffusion parallel to [001]. The Figure shows the absorption coefficient as a function of wavenumber and position in the single crystal. Intensity and area of

hydroxyl infrared bands are highest at the edges and decrease toward the middle of the sample until a minimum absorption coefficient corresponding to  $\sim 4$  wt ppm  $\text{H}_2\text{O}$  ( $65 \text{ H}/10^6\text{Si}$ ) is reached. This background corresponds to hydrogen incorporated by the fast redox exchange process (Kohlstedt and Mackwell, 1998).

The data were fit using a least squares regression to the following Arrhenius relation (Eq. 17, section 3.3.2).

$$\tilde{D}_i = \tilde{D}_i^0 \exp(-Q_i / RT)$$

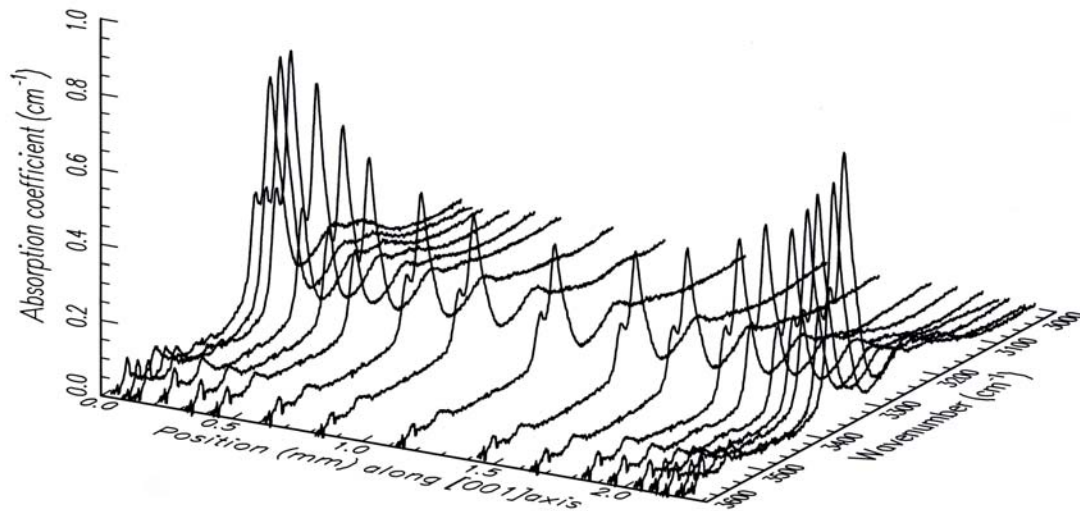


**Figure 4.1.2.** Series of polarized infrared spectra with  $E // [001]$  as a function of position parallel to  $[001]$  in sample SC 33-A after an experiment at 0.2 GPa,  $900^\circ\text{C}$ , for 20 hours buffered with Ni-NiO.

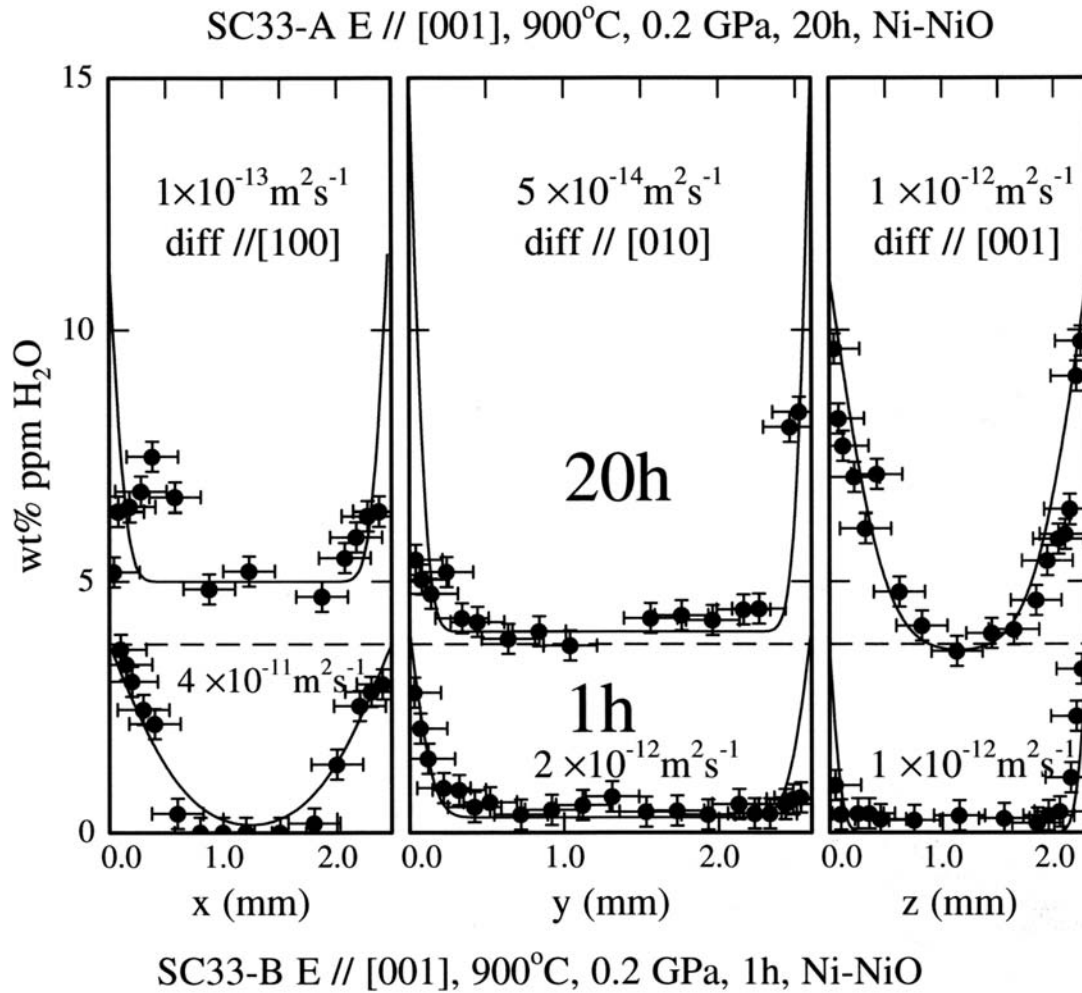


**Figure 4.1.3.** Hydroxyl content as a function of position parallel to each crystallographic axis ( $x = [100]$ ,  $y = [010]$ ,  $z = [001]$ ) for sample SC 33-A after a hydrogenation experiment at 0.2 GPa, 900°C, 20 hours, buffered with Ni-NiO, and sample SC 33-B after a hydrogenation experiment at 0.2 GPa, 900°C, 1 hour, buffered with Ni-NiO. The solid curves represent the solution to the diffusion law presented in Eq. (16). The chemical diffusion coefficient,  $\tilde{D}$ , is given for each axis. Errors in the diffusion coefficients are given in Table 4.1.3.

*First process of incorporation*

Following Eq. (19), the diffusion coefficient of hydrogen obtained for hydrogen incorporation by redox exchange along [100] is around  $4 \pm 0.5 \cdot 10^{-11} \text{ m}^2/\text{s}^{-1}$ , at  $900^\circ\text{C}$ , which is slightly lower than results from previous works ( $5 \cdot 10^{-11} \text{ m}^2/\text{s}^{-1}$ , at  $900^\circ\text{C}$ , Mackwell and Kohlstedt, 1990).

*Second process of incorporation*

Because of the small number of experiments and the previous observation of similar diffusivities for the [100] and the [010] axes (Kohlstedt and Mackwell, 1998), a similar activation energy and pre-exponential term are assumed for both [100] and [010]. Thus hydrogen incorporation can be described for each crystallographic axis by the following relationships, assuming that hydrogen diffusion is limited by metal-vacancy diffusivity (Eq. 21),

- $D_{V_{Me}} [100], [010] = 10^{-(5.6 \pm 3.2)} \exp [-(175 \pm 76)/RT]$
- $D_{V_{Me}} [001] = 10^{-(1.4 \pm 0.5)} \exp [-(258 \pm 11)/RT]$

*(activation energies in kJ/mol)*

These results for hydrogen incorporation linked to metal vacancy diffusion are similar to the preliminary results ( $260 \pm 20 \text{ kJ/mol}$ ) obtained by Kohlstedt and Mackwell, (1998). The diffusivities obtained for [010] are well correlated. However, more experiments are necessary to constrain more fully hydrogen diffusion rates along [100], especially at high temperature (Figure 4.1.4).

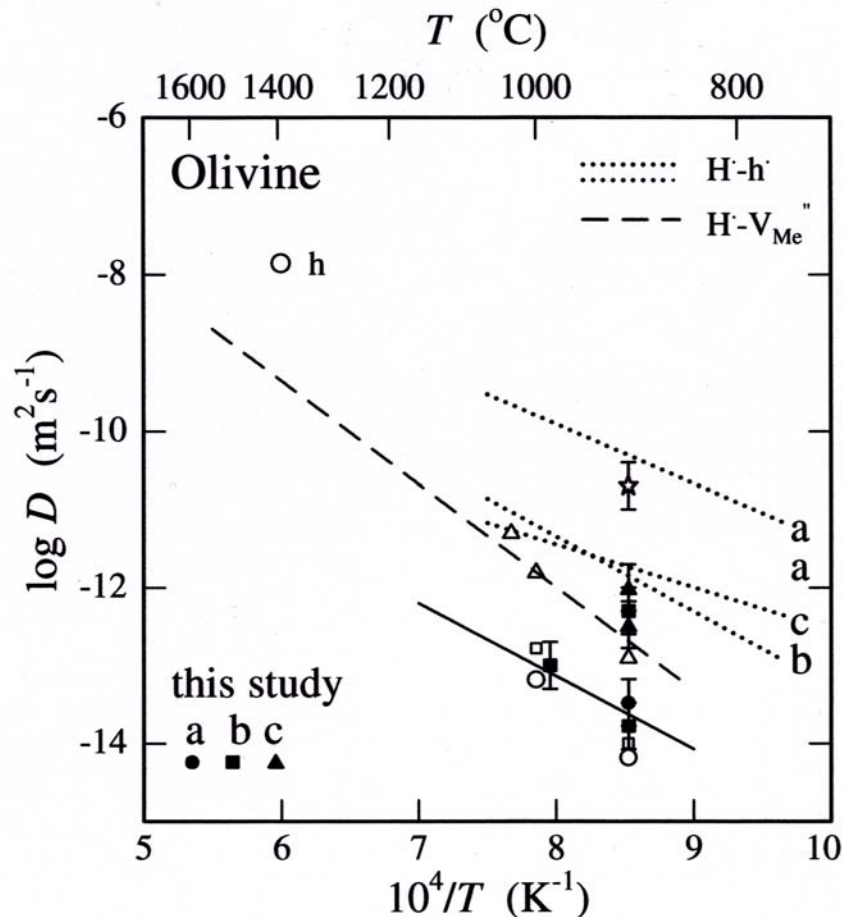


**Figure 4.1.4** Diffusivity for metal vacancies and hydrogen ions in olivine.

*This study:* The filled symbols are the results from the hydrogen incorporation process linked to metal vacancy diffusivities in olivine. The star symbol represents hydrogen incorporation by redox exchange along [100] into olivine. The solid line is the best fit for the hydrogen incorporation process linked to metal vacancy diffusivities in olivine parallel to [100] and [010].

*From previous works:* The dotted lines represent the results from Kohlstedt and Mackwell (1998) for hydrogen diffusion during redox exchange. The open symbols are the previous results from Kohlstedt and Mackwell (1998) for hydrogen incorporation linked to metal vacancy diffusion. The dashed line represents the linear fit to the compilation of data for metal vacancy diffusion in iron-bearing olivine from previous publications (Nakamura and Schmalzried 1983; 1984; Mackwell et al. 1988; Kohlstedt and Mackwell 1998) and also includes results for the [001] direction from this study. The circle represents the polaron diffusivity calculated by Sato (1986) from electrical conductivity measurements.

##### *Effect of $a_{\text{SiO}_2}$ on infrared band position and water solubility*

In theory, each infrared band corresponds to a distinct kind of hydrous point defect. However assigning infrared bands is a current topic of debate. Recently, Matveev et al. (2001) have suggested that experimentally hydrated olivine does not possess the same IR bands as natural olivine. Furthermore, they have suggested that the two distinct infrared band groups result from different  $a_{\text{SiO}_2}$ , with high-wavenumber bands (in olivine co-existing with magnesio-wüstite) linked to a vacant tetrahedral site and low-wavenumber bands (in olivine co-existing with orthopyroxene) linked to a vacant octahedral site. Table 4.1.4 presents the IR band positions observed by Matveev et al. (2001) and from this study. It is clear that in contradiction to the suggestions of Matveev et al. (2001), the experimentally hydrated olivine from this study contains IR features including group I and group II. Thus the simplified model of Matveev et al., (2001) may be not appropriate.

##### *Application to the Earth's interior*

Diffusive loss of water by redox-exchange and coupled vacancies/proton transport will occur in times that are very short compared to the times for ascent of mantle plumes (between 0.2 and 10 m/y, d'Acremont et al., 2003). The diffusion rates obtained here also predict times for partial dehydration of olivine grains that are short in comparison to times for xenoliths to be entrained and brought to the Earth's surface. Thus, one should expect some modification of the original mantle water content in xenolithic olivine. However, full re-equilibration to the new (hydrous or anhydrous) environment during ascent is unlikely. Consequently, water solubility in xenolithic olivine crystals is at best only a partial reflection of the last geological event in an olivine's life.

On the other hand, while gradients in Fe and Mg resulting from transport have been observed in NAMs (Ganguly et al. 1994, 1996, 2001; Shaw, 2004), "natural" water diffusion profiles have never been reported. If such profiles were observed in natural xenolithic olivine, these observations would provide verification that the processes of dehydration discussed here do occur in the Earth. In addition, it might be

possible to use such profiles, with these experimental results, to provide constraints on the processes bringing xenoliths to Earth's surface.

**Table 4.1.1** Hydroxyl band positions for olivine hydrated in equilibrium with different  $a_{SiO_2}$  buffers from this study and from Matveev et al., (2001).

SC33 <sup>1♦</sup> + enstatite		olivine <sup>2</sup> + enstatite		olivine <sup>3</sup> + magnesiowüstite	
[100]	[010]	[001]	unpolarized	unpolarized	
				3640	Group I
3616*				↓	
3599					
3572	3571	3571			
3563					
3540*					
		3531			Group II
3525	3526			↓	
			3380		
3352	3355	3352	↓		
3327	3327	3327			
		3222	3285		

♦ wavenumber resolution  $\pm 1 \text{ cm}^{-1}$

<sup>1</sup> San Carlos olivine sample from this study

<sup>2</sup> hydrated olivine (Fo<sub>90-91</sub>) in equilibrium with orthopyroxene and assumed to be due to H in octahedral cation sites (Matveev et al., 2001).

<sup>3</sup> hydrated olivine synthesized in equilibrium with magnesiowüstite assumed to be due to H in tetrahedral cation sites (Matveev et al., 2001).

##### *Additional application to the Earth's interior: the effect of water on the electrical conductivity of minerals*

There have been a number of studies on electrical conductivity of minerals and its relation with point defects (*e.g.*, Lastovickova 1987, 1991; Hirsch and Shankland, 1993; Hirsch et al., 1993; Wanamaker and Buda, 1993; Xu et al, 1998; Constable and Duba, 2002). In 1990, Karato (1990) was the first to point out that the presence of water (embedded hydrogen) increases significantly the electrical conductivity of Earth upper mantle minerals, which was later developed by other experimentalists (Wang and Li., 1999; B. Poe, person. comm.). More recently Bahr and Simpson (2002), Simpson (2002) and Gatzemeier and Bahr (2003) suggested that at the base of the lithosphere, the electrical conductivity and especially its anisotropy might be explained by the presence of water and the strong anisotropy of water diffusion within olivine. As shown by Figure 4.1.5, a thick layer of wet olivine (Figure 4.1.5 A) could explain the conductance observed by Simpson (2002a, 2002b) but not the observed anisotropy of conductances. Aligned olivine with conducting hydrogen ions (Figure 4.1.5 B) could explain the observed conductances except that it requires a very thick lithosphere (~ 190 km) or a extremely high water concentration (1000 ppm H/Si = 6,120 wt ppm H<sub>2</sub>O = 0.6 wt % H<sub>2</sub>O in olivine), which should not be the case in olivine at this pressure, following the solubility law of Kohlstedt et al. (1996). The diffusivity presented here permits an improvement in the modeling in order to explain the electrical conductivity measurements and magneto-telluric data (Bahr, person. comm., 2003).

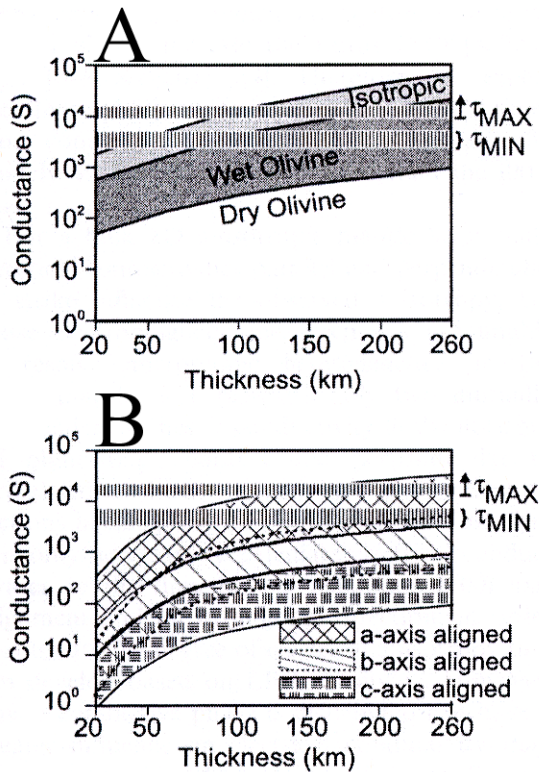


**Figure 4.1.5** (Modified from Simpson 2002). Electrical conductance ( $\tau$ ) as a function of the thickness for a mantle layer composed of (1) dry olivine and wet olivine and (2) aligned olivine with incorporation of hydrogen by diffusion, assuming  $D[100] \gg D[010] \gg D[001]$ , therefore assuming that redox exchange process is dominant. Upper and lower bounds on the shaded zone represent 100 ppm H/Si (= 612 wt ppm H<sub>2</sub>O in olivine Fo<sub>90</sub>) and 1,000 ppm H/Si (~ 6,000 wt ppm H<sub>2</sub>O in olivine Fo<sub>90</sub>) respectively.

### 4.1.3. Conclusions

The anisotropies of hydrogen diffusion for both mechanisms are similar to those reported in earlier works by Mackwell and Kohlstedt (1990) and Kohlstedt and Mackwell (1998). Therefore, the existence of two distinct mechanisms of hydrogen incorporation is confirmed.

1. For the second process of hydrogen incorporation (involving vacancies), diffusivities along the [100] and the [010] axes are significantly slower than along [001], in agreement with previous studies.
3. From the experimental results and assuming that the second process of hydrogen diffusion is linked to metal vacancies, where the vacancies are the slower diffusing species, metal vacancy diffusion can be described by:

#### 4. 1. Results: Hydrogen diffusion in olivine

---

- $D_{V_{Me}} [100], [010] = 10^{-(5.6 \pm 3.2)} \exp [-(175 \pm 76)/RT] \text{ m}^2\text{s}^{-1}$
- $D_{V_{Me}} [001] = 10^{-(1.4 \pm 0.5)} \exp [-(258 \pm 11)/RT] \text{ m}^2\text{s}^{-1}$

*(activation energies in kJ/mol)*

Insufficient experiments are yet available to distinguish between the diffusion laws for diffusion along [100] and [010].

## 4.2. Hydrogen diffusion in forsterite

### 4.2.1. Introduction

The aim of this section is to constrain more fully the speciation and transport rate of the mobile water-derived defects in synthetic forsterite, where there is no iron and, hence, no polarons. This section presents the results of experiments in piston-cylinder and TZM cold-seal vessels to produce hydration profiles. Details of the experimental procedures and analytical techniques are provided in section 2. Table 4.2.1 summarized the experiments performed.

**Table 4.2.1** Experimental conditions of hydration for forsterite samples.

Sample	Apparatus	Temperature °C	Pressure GPa	Time h	Buffer	log $fO_2$	Capsule
Fo1-3	PC	1000	1.5	3	Fe-FeO	-14.2	Fe
Fo2-2	PC	1000	1.5	3	Ni-NiO	-10.3	Pt <sub>0.95</sub> -Rh <sub>0.05</sub>
Fo2-4	TZM	1000	0.2	8	Ni-NiO	-10.3	Pt
Fo2-5	TZM	1060	0.2	8	Ni-NiO	-9.4	Pt
Fo2-6	TZM	1060	0.2	8	Ni-NiO	-9.4	Pt
Fo2-8	TZM	1100	0.2	3	Ni-NiO	-8.9	Pt
Fo2-9	TZM	1110	0.2	3	Ni-NiO	-8.7	Pt
Fo2-10	TZM	1110	0.2	3	Ni-NiO	-8.7	Pt
Fo2-12	TZM	900	0.2	20	Ni-NiO	-11.9	Pt
Fo2-13	TZM	950	0.2	12	Ni-NiO	-11.0	Pt
Fo2-14	TZM	900	0.2	20	Ni-NiO	-11.9	Pt

PC = Piston-cylinder, TZM = titanium-zirconium-molybdenum cold-seal vessel.

log  $fO_2$  calculated according to O'Neill (1987) for Ni-NiO, and O'Neill and Wall (1987) for Fe-FeO.

### 4.2.2. Infrared spectra and water contents

Figure 4.2.1 shows typical polarized FTIR spectra of the hydrated forsterite samples from crystal Fo1 and Fo2. The major O-H absorption bands for samples from Fo2 are at  $3613\text{ cm}^{-1}$  and  $3579\text{ cm}^{-1}$  for E parallel to  $[100]$  and at  $3155\text{ cm}^{-1}$  and  $3567\text{ cm}^{-1}$  for E parallel to  $[001]$ . Sample Fo1-3, which had been treated at more reducing conditions, shows only a very weak band at  $3613\text{ cm}^{-1}$  with E parallel to  $[100]$  and a strong band at  $3215\text{ cm}^{-1}$  with E parallel to  $[001]$ . Positions for all O-H bands observed in the hydrogenated forsterite samples are shown in Table 4.2.2. The band positions do not change with experimental run duration or temperature. The maximum water contents (Table 4.2.3) calculated from the infrared spectra with beam polarization parallel to all three crystal axes using the calibration of Bell et al. (2003), vary from  $1.3 \pm 0.2$  wt ppm water ( $20 \pm 3\text{ H}/10^6\text{Si}$ ) in sample Fo2-12 to  $6.4 \pm 0.9$  wt ppm water ( $100 \pm 14\text{ H}/10^6\text{Si}$ ) in sample Fo1-3. In general, water contents increases with increasing temperature at fixed pressure, except for sample Fo2-8, which has an inexplicably lower water content than other samples treated at essentially the same conditions. The water contents reported for Fo2-2 is a minimum value as poor sample quality made it impossible to measure hydroxyl concentrations with E polarized parallel to all 3 crystallographic axes.

As suggested by the IR spectra, TEM observations, carried out in the hydrated regions near the sample edges as well as in the anhydrous interior, demonstrate that the sample Fo2-10 was free of hydrous inclusions, precipitates, linear and planar defects (see TEM documentation in appendix 3).

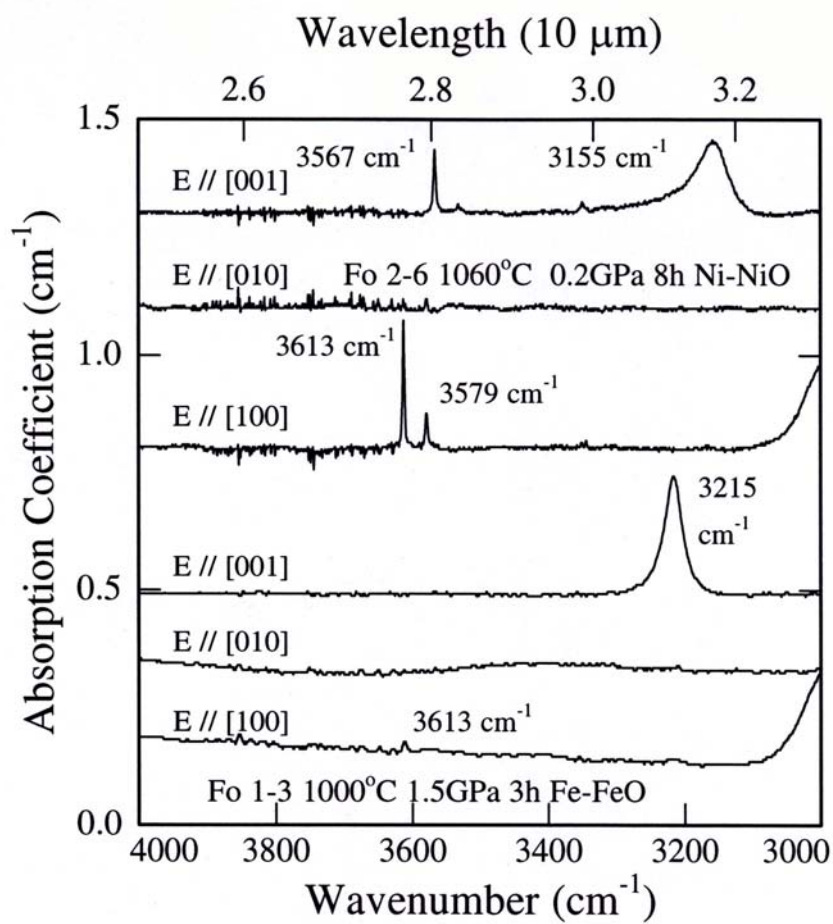


**Figure 4.2.1.** Polarized IR spectra, with different orientations of electrical vector  $E$ , for forsterite samples Fo1-3 (after an experiment at 1000°C, 1.5 GPa, 3 hours duration, buffered by Fe-FeO) and Fo2-6 (after an experiment at 1060°C, 0.2 GPa, 8 hours duration and buffered by Ni-NiO). The noise of the spectra for Fo2-6 results from the poor quality of the sample.

## 4.2. Results: hydrogen diffusion in forsterite

**Table 4.2.2** Hydroxyl band positions for different orientations of the infrared electric vector (E) in synthetic forsterite from this study and from iron-bearing olivine from previous investigations.

Fo1-3 <sup>1</sup>		Fo2 <sup>1</sup>			San Carlos olivine <sup>2</sup>	Pamir olivine <sup>3</sup>
E // [100]	[001]	[100]	[010]	[001]	Unpolarized	All polarization directions
						3674
						3647
					3637	3640
					3623	3624
3613		3613			3612	
					3598	3598
						3592
		3579	3577		3576	
						3570
				3567*	3565	
			3552		3542	
				3534*		3535
				3531*	3529	
						3524
						3514
					3483	3478*
					3459	
					3443	
					3424	
						3404*
					3389	
				3350	3354	
		3344				3341*
					3329	
					3236	
	3215					3215*
				3155		

Wavenumber resolution  $\sim \pm 2 \text{ cm}^{-1}$

\* indicates a weak infrared band

<sup>1</sup> synthetic forsterite samples from this study

<sup>2</sup> hydrated San Carlos olivine (Bai and Kohlstedt 1993)

<sup>3</sup> natural olivine from skarn deposit in Pamir, Tadzikistan (Libowitzky and Beran 1995)

## 4.2. Results: hydrogen diffusion in forsterite

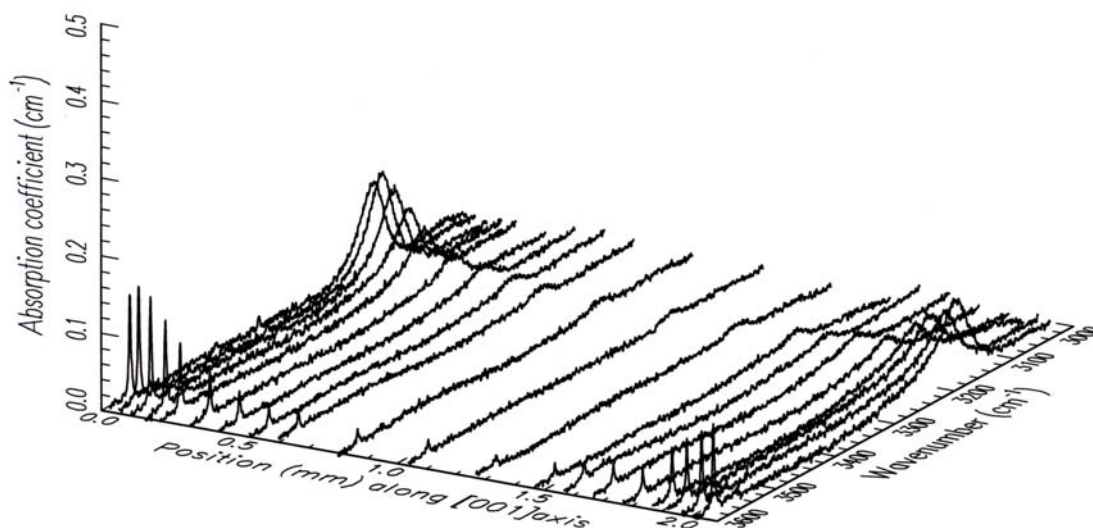
**Table 4.2.3** Maximum water contents in forsterite samples and chemical diffusivities along each axis.

Sample	Maximum water content <sup>#</sup> wt ppm H <sub>2</sub> O (H/10 <sup>6</sup> Si)	$\tilde{D}$ [100] m <sup>2</sup> s <sup>-1</sup>	$\tilde{D}$ [010] m <sup>2</sup> s <sup>-1</sup>	$\tilde{D}$ [001] m <sup>2</sup> s <sup>-1</sup>
Fo 1-3 1000°C	6.4 ± 0.9 (100 ± 14)	(4 ± 1). 10 <sup>-13</sup>	(3.0 ± 0.2). 10 <sup>-13</sup>	(5.0 ± 0.2). 10 <sup>-13</sup>
Fo 2-2* 1000°C	>1.1 ± 0.2 (>17 ± 3)	(7.0 ± 0.2). 10 <sup>-13</sup>	(3.0 ± 0.2). 10 <sup>-13</sup>	<i>np</i>
Fo 2-4 1000°C	2.8 ± 0.4 (44 ± 6)	(1.0 ± 0.4). 10 <sup>-13</sup>	(1 ± 1). 10 <sup>-13</sup>	(1.0 ± 0.2). 10 <sup>-12</sup>
Fo 2-5 1060°C	5.7 ± 0.8 (89 ± 12)	(2.0 ± 0.5). 10 <sup>-13</sup>	(1.0 ± 0.5). 10 <sup>-12</sup>	(3.0 ± 0.8). 10 <sup>-12</sup>
Fo 2-6 1060°C	5.5 ± 0.8 (86 ± 12)	(2.0 ± 0.5). 10 <sup>-13</sup>	(6 ± 1). 10 <sup>-13</sup>	(2.0 ± 0.5). 10 <sup>-12</sup>
Fo 2-8 1100°C	2.3 ± 0.3 (36 ± 5)	(5 ± 2). 10 <sup>-13</sup>	(1.0 ± 0.2). 10 <sup>-12</sup>	(1.3 ± 0.2). 10 <sup>-11</sup>
Fo 2-9 1110°C	5.7 ± 0.8 (89 ± 12)	(8 ± 4). 10 <sup>-14</sup>	(1.6 ± 0.5). 10 <sup>-12</sup>	(3.5 ± 0.5). 10 <sup>-12</sup>
Fo 2-10 1110°C	3.6 ± 0.5 (56 ± 8)	(1 ± 1). 10 <sup>-13</sup>	(3.6 ± 2.0). 10 <sup>-13</sup>	(1.0 ± 0.5). 10 <sup>-12</sup>
Fo 2-12 900°C	1.3 ± 0.2 (20 ± 3)	<i>nwd</i>	<i>nwd</i>	(2.0 ± 0.6). 10 <sup>-13</sup>
Fo 2-13 950°C	4.2 ± 0.6 (66 ± 9)	<i>np</i>	(2 ± 1). 10 <sup>-13</sup>	(7 ± 1). 10 <sup>-13</sup>
Fo 2-14 900°C	3.8 ± 0.5 (59 ± 8)	(2 ± 1). 10 <sup>-13</sup>	(2 ± 1). 10 <sup>-13</sup>	(2.5 ± 0.5). 10 <sup>-13</sup>

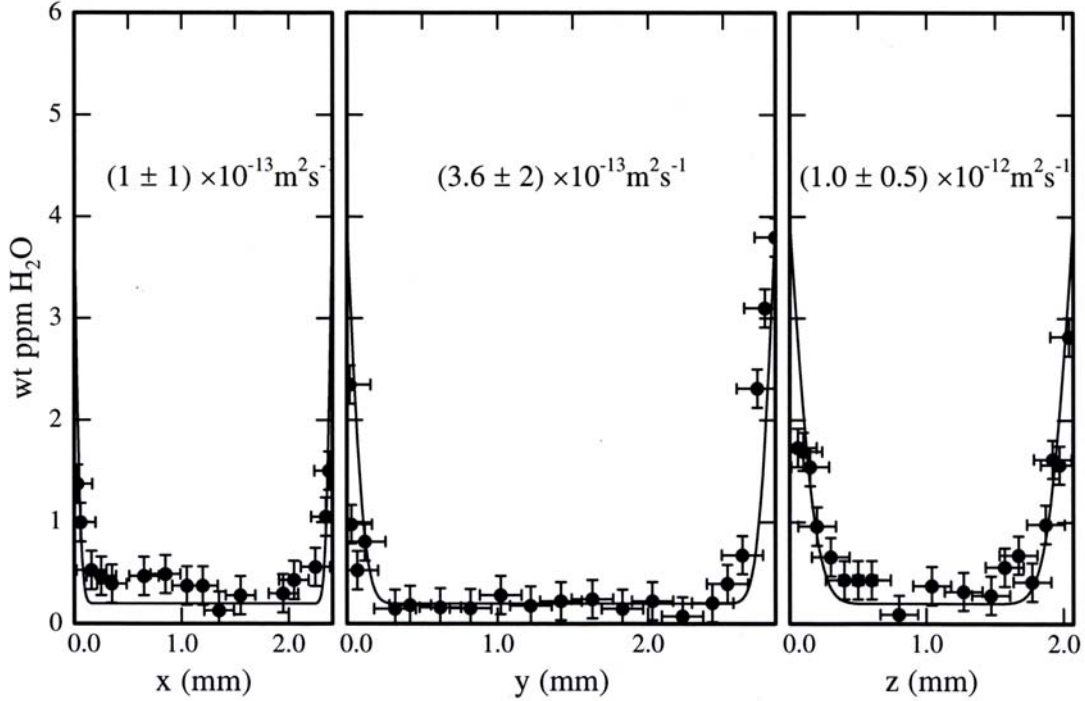
\* Because of the poor quality of the sample, it was not possible to do infrared analysis with E // [001] so measurements were made only with E // [100]. Thus the quoted water content is a lower limit of the true water content only. *np*: because of the poor quality of the sample, it was not possible to fit a profile. *nwd*: no water detected by infrared spectroscopy as there was insufficient hydroxyl for measurement along this axis. <sup>#</sup> water content at the rim of the sample using Eq. (7) and the calibration of Bell et al. (2003).

### 4.2.3 Diffusion rates and anisotropy

Figure 4.2.2 presents a series of polarized infrared spectra for sample Fo2-9 with  $E // [001]$  and diffusion parallel to  $[001]$ . The Figure shows absorption coefficient as a function of wavenumber and position in the sample. Intensity and area of hydroxyl infrared bands are highest at the edges and decrease toward the middle of the sample. Chemical diffusivities for each sample and each diffusion direction are given in Table 4.2.3. The diffusion is anisotropic, with fastest diffusion parallel to  $[001]$  and slowest diffusion generally parallel to  $[100]$ . An example of hydroxyl diffusion profiles for each axis is plotted in Figure 4.2.3 for sample Fo2-10, with  $E$  parallel to  $[001]$ . The black lines represent the best fits of the diffusion law to the data using Eq. (16), which yielded the chemical diffusivities given on the Figure. The fits were performed assuming the same hydroxyl concentration at the edges of each sample and in the middle. While some data deviate somewhat from the fitted curves, they fall mostly within the uncertainty limits of the measurements. These deviations often resulted from small imperfections, such as conchoidal fractures on the sample corners or small surface scratches.



**Figure 4.2.2.** Series of polarized infrared spectra with  $E // [001]$  as a function of position parallel to  $[001]$  in sample Fo2-9 after a experiment at 0.2 GPa, 1110°C, for 3 hours buffered with Ni-NiO.



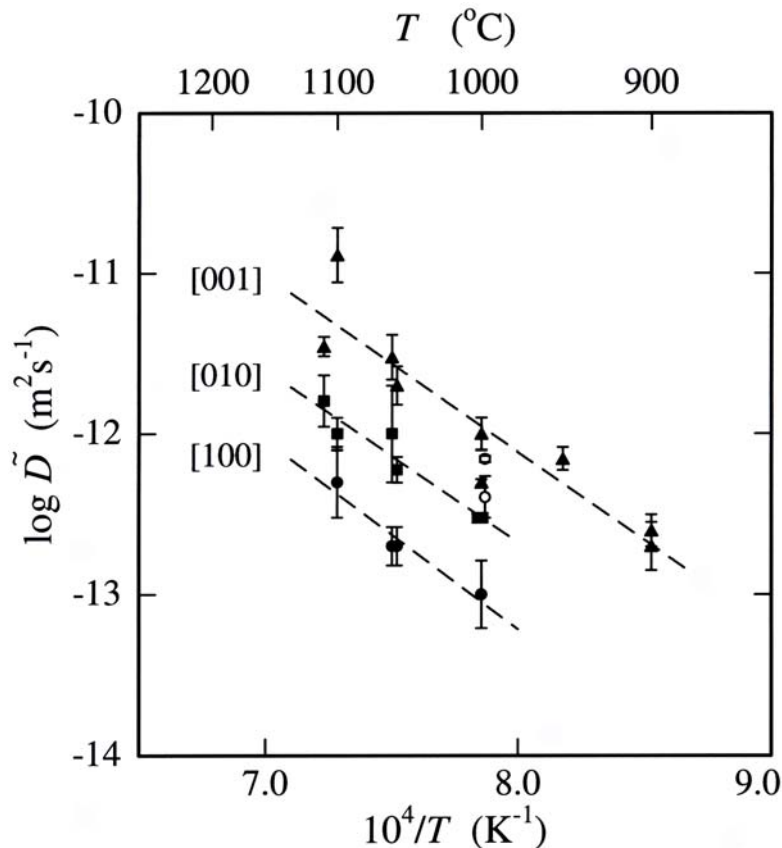
**Figure 4.2.3.** Hydroxyl content as a function of position parallel to each crystallographic axis ( $x = [100]$ ,  $y = [010]$ ,  $z = [001]$ ) for the sample Fo2-10 after a hydrogenation experiment at 0.2 GPa, 1110°C, 3 hours, buffered with Ni-NiO. The *solid curves* represent the solution to the diffusion law presented in Eq. (16). The chemical diffusion coefficient,  $\tilde{D}$ , is given for each axis.

Figure 4.2.4 shows chemical diffusivities for hydrogen incorporation as a function of temperature for diffusion parallel to each of the crystal axes. Only diffusion coefficients with errors lower than 30% for diffusion parallel to [001] and lower than 50% for diffusion parallel to [010] and [100] are plotted in the Figure and were used to calculate activation energies. While the data for diffusion parallel to [001] and [010] for the experiments at 1.5 GPa agreed well with those from experiments at 0.2 GPa, the data on diffusion parallel to [100] for both Fo1-3 and Fo2-2 (the open circles in Figure 4.2.4) are significantly faster than those from the lower pressure experiments, and were not used in the activation energy calculations. While a possible anisotropic dependence of diffusivity on pressure is intriguing, quantification of such an effect is beyond the aim of the present work. The remaining data were fit using a least squares regression to the Arrhenius relation:

$$\tilde{D}_i = \tilde{D}_i^0 \exp(-Q_i / RT) \quad \text{Eq. 17}$$

where  $\tilde{D}_i$  is the chemical diffusion coefficient parallel to  $i = [100]$ ,  $[010]$  or  $[001]$ ,  $\tilde{D}_i^0$  is the pre-exponential term and  $Q_i$  is the activation energy for diffusion. Using Eq. (17), the activation energies and pre-exponential terms were determined for chemical diffusion of  $210 \pm 33 \text{ kJmol}^{-1}$  and  $10^{-3.3 \pm 1.3} \text{ m}^2 \text{ s}^{-1}$  for diffusion parallel to  $[001]$ ,  $205 \pm 31 \text{ kJmol}^{-1}$  and  $10^{-4.1 \pm 1.2} \text{ m}^2 \text{ s}^{-1}$  for diffusion parallel to  $[010]$ , and  $225 \pm 40 \text{ kJmol}^{-1}$  and  $10^{-3.8 \pm 1.6} \text{ m}^2 \text{ s}^{-1}$  for diffusion parallel to  $[100]$ .

As the calculated activation energies for chemical diffusion are, within error, the same for all directions, a global fit to all data were performed for all directions and yield an activation energy for chemical diffusion of  $211 \pm 18 \text{ kJmol}^{-1}$  and pre-exponential terms of  $10^{-3.3 \pm 0.7} \text{ m}^2 \text{ s}^{-1}$  parallel to  $[001]$ ,  $10^{-3.9 \pm 0.7} \text{ m}^2 \text{ s}^{-1}$  parallel to  $[010]$ , and  $10^{-4.4 \pm 0.7} \text{ m}^2 \text{ s}^{-1}$  parallel to  $[100]$ . The global fit was performed by varying the activation energy and pre-exponential terms until the root-mean-square-deviation of the fit from the data was minimized.



**Figure 4.2.4.** Diffusivity for metal vacancies and hydrogen ions in forsterite. The *solid symbols* are the results from the hydrogen incorporation process linked to metal vacancies. The *dashed lines* represent the best linear least squares fit to the data for each axis. The *open circles* are the experiment at 1.5 GPa (see text for explanations).

#### 4.2.4. Discussion

##### *Infrared band positions and water solubility*

Table 4.2.2 presents infrared band positions from this study and from previous work on iron-bearing olivine (Bai and Kohlstedt 1993; Libowitzky and Beran 1995). Three main differences are apparent: (1) Hydroxyl infrared bands in forsterite are more strongly polarized than in olivine. (2) The forsterite spectra do not show bands between 3680 and 3620  $\text{cm}^{-1}$ , suggesting that these bands could represent hydrogen linked to iron-related point defects or that these bands may represent layers of hydrous minerals within olivine as suggested by Miller et al. (1987), and reported in Table 1.4. (3) A strong band is situated at 3155  $\text{cm}^{-1}$  in sample Fo2 and at 3215  $\text{cm}^{-1}$  in sample Fo1-3, in both cases with E parallel to [001]. Although Libowitzky and Beran (1995) mentioned a very weak band at 3215  $\text{cm}^{-1}$ , such a strong band has not been observed previously in this wavenumber range in forsterite. The source of this band is unlikely to be due to sample contamination as the forsterite samples are still perfectly transparent after the experiments and contamination from the buffer powders was not detected by EMPA measurements.

An alternative source of this band could be hydrogen-boron defects, as there is certainly abundant boron in the Fo2 forsterite crystal. Unfortunately, there was not enough hydrated Fo2 material to perform middle infrared analysis (MIR) using KBr pellets in the wavenumber range 760-530  $\text{cm}^{-1}$  to check for  $[\text{B}(\text{OH})_4]^-$  and to compare with the spectra of Sykes et al. (1994). Sufficient material was also not available to perform ICP-AES analysis of the Fo1 crystal to check the boron content after experiment. In addition, the effect of boron on hydroxyl band positions is difficult to estimate. Thus, although hydrogen-boron associated defects are likely in these samples crystals, it is not possible to claim definitively these as source of the hydroxyl bands in forsterite at 3215 $\text{cm}^{-1}$  and 3155  $\text{cm}^{-1}$ .

A recent study by Lemaire et al. (2004) on the effect of  $a_{\text{SiO}_2}$  on hydrogen site occupancy in olivine (polarized FTIR study) suggests that bands at low-wavenumber (3160-3220  $\text{cm}^{-1}$ ) are linked to a medium or high  $a_{\text{SiO}_2}$ . Thus an alternative cause for the low wavenumber bands (3220  $\text{cm}^{-1}$ ) could be the high activity of silica in the experiments.

In previous studies the infrared bands have, based mostly of bond orientations, been variously assigned as hydrogen divalent metal vacancy or hydrogen-silicon vacancy associated defects (e.g., Beran and Putnis 1983; Freund and Oberheuser 1986; Matveev et al. 2001; Locke et al. 2002). In the recent work of Matveev et al. (2001), hydroxyl bands between  $3380\text{-}3285\text{ cm}^{-1}$  were assigned as hydrogen linked to divalent metal vacancies whereas hydroxyl bands at higher-frequencies  $3640\text{-}3430\text{ cm}^{-1}$  and at  $3295\text{ cm}^{-1}$  were attributed to hydrogen substitution in tetrahedral (silicon) sites. Unfortunately, direct association of hydroxyl infrared bands with specific point defects remains controversial and these results do not permit discrimination between the defect models. The fact that all bands seem to be incorporated into forsterite at similar rates is suggestive of, but certainly does not guarantee, a single diffusive species.

When FTIR spectroscopy is used to quantify water content, a calibration has to be applied to the spectra to determine the water concentration. The reliability of the various calibrations is a source of ongoing debate (Paterson 1982; Bell et al. 1995; Libowitzky and Rossman 1996; Bell et al. 2003). In this study, the calibration of Bell et al. (2003) was used following Eq. (7). It is noteworthy, however, that the choice of infrared calibration will have no effect on the calculated diffusivities (Kohlstedt and Mackwell 1998).

### *Diffusion in forsterite*

On the assumption that hydrogen self-diffusion is much faster than metal vacancy diffusion (Kohlstedt and Mackwell 1998), the Eq. (21) was used to determine the diffusivities for metal vacancies from the chemical diffusivities. Figure 4.2.5 presents diffusion rates as functions of temperature from this study, as well as from previous work on transport of water-derived species, metal vacancies and electron holes in olivine (Nakamura and Schmalzried 1983; Sato 1986; Mackwell and Kohlstedt 1990; Kohlstedt and Mackwell 1998). The results are in good agreement with previous work on metal vacancy diffusion in iron-bearing olivine using (1) water as a tracer, as in this study (label KM in Figure 4.2.5; Kohlstedt and Mackwell 1998), (2) reequilibration rates from deformation and electrical conductivity experiments (Mackwell et al. 1988; Wanamaker 1994), (3) electrical conductivity measurements of Constable and Duba (2002), and (4) Fe-Mg interdiffusion and thermal balance

measurements (Nakamura and Schmalzried 1983; 1984). Compared with the previous work on diffusion of hydrogen-metal vacancy diffusion in iron-bearing olivine (Kohlstedt and Mackwell 1998), although the diffusivities are a little slower for the same orientation and temperature, the anisotropy in diffusion of hydrogen-metal vacancy defects is the same as in iron-bearing olivine, with fastest diffusion parallel to [001] (Figure 4.2.5). Parallel to [001], the activation energy for diffusion is  $210 \pm 33$  kJ.mol<sup>-1</sup> is slightly lower compared to that for olivine of  $260 \pm 20$  kJmol<sup>-1</sup> (Kohlstedt and Mackwell 1998) and  $258 \pm 11$  kJmol<sup>-1</sup> (section 4.1) .

### *Point defects in forsterite*

End-member forsterite (Mg<sub>2</sub>SiO<sub>4</sub>) is near-stoichiometric and an insulator. Deviations from stoichiometry are expected to result from thermal Frenkel defects on the metal sublattice (e.g., Stocker 1978; Stocker and Smyth 1975). At the relatively low homologous temperatures of the experiments, defect concentrations are likely only at sub-ppm levels. However, as noted above, boron may play a significant role in the point-defect chemistry of the studied forsterite, as it is the majority impurity species. While boron is most likely in the +3 valence state, as a substitutional defect in silicon sites and is charge compensated by metal vacancies, its detailed speciation is not known with certainty. Should the boron reside mostly in the silicon sites, a logical role for hydrogen would be to charge compensate the boron, making hydrogen-boron associations a favoured defect in the structure of synthetic forsterite.

Given that the rate and anisotropy of diffusion are similar to those for iron-bearing olivine, it seems reasonable to assume that the same diffusion mechanism is involved in forsterite (Kohlstedt and Mackwell 1998). Thus, incorporation of water into the forsterite structure at ppm levels requires the cooperative incorporation of other defects, probably divalent metal (octahedrally coordinated) or silicon (tetrahedrally coordinated) vacancies. The resulting concentration of vacancies (divalent metal or silicon) is thus significantly higher when associated with water than under dry conditions. The concentrations of such defects, as indicated by the hydroxyl concentrations in the samples, are similar or possibly slightly lower than in iron-bearing olivine. Thus, the concentration of hydrogen-vacancy associated defects is not highly dependent on iron content.

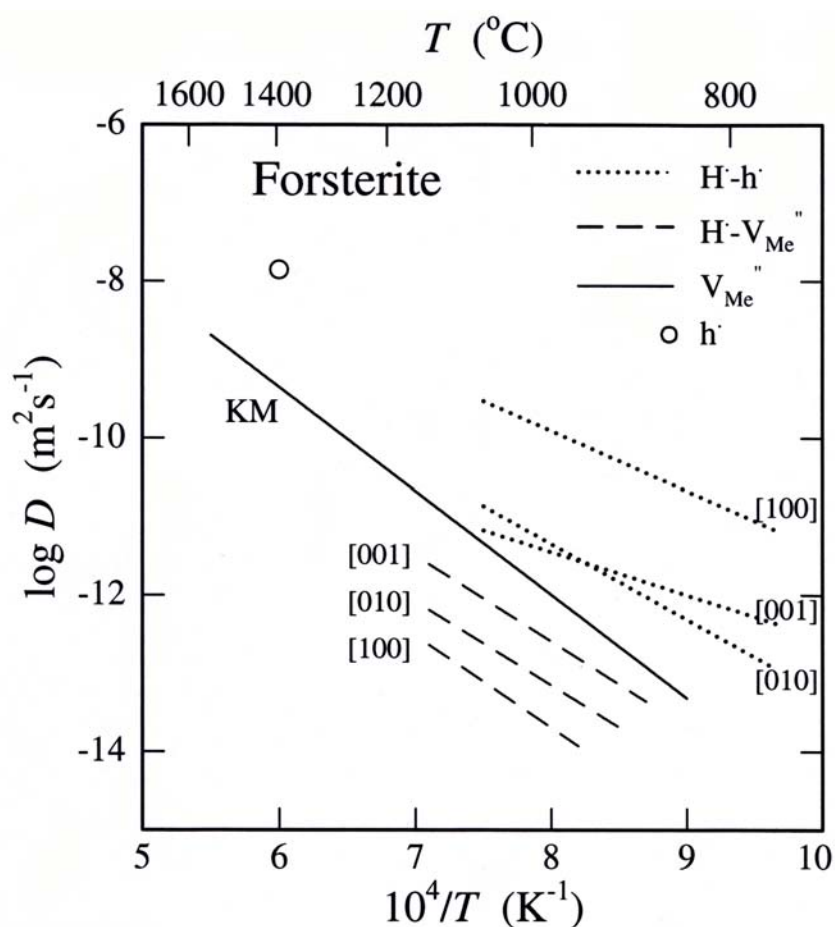


**Figure 4.2.5** Diffusivities for metal vacancy and hydrogen ions in olivine and forsterite. The *dashed lines* are the metal vacancy diffusivities assuming hydrogen incorporation process linked to metal vacancy transport. The *dotted lines* represent the results from Kohlstedt and Mackwell (1998) for hydrogen diffusion during redox exchange in olivine. The *solid line* represents the linear fit to the compilation of data for metal vacancy diffusion in iron-bearing olivine from previous publications (Nakamura and Schmalzried 1983; 1984; Mackwell et al. 1988; Kohlstedt and Mackwell 1998). *The circle* represents the polaron diffusivity calculated by Sato (1986) from electrical conductivity measurements.

Interestingly, the stabilization of higher concentrations of vacancies (divalent metal or silicon) by the presence of water-derived species should act to increase the diffusivities of the appropriate cations in the forsterite structure (Costa and

Chakraborty, perso. comm., 2004) . Thus, if the defects are mostly hydrogen-metal vacancy associate pairs, a significant increase in magnesium diffusion or iron-magnesium interdiffusion in a hydrous environment might be anticipated. On the other hand, if the defects are mostly hydrogen-silicon vacancies, a major weakening of the mechanical behaviour of forsterite under wet conditions might be expected.

### *Implication of the upper mantle*

These experiments shows that for equilibration of forsterite (or olivine) crystals in response to a change in the hydrothermal environment can be expected to take significantly longer than predicted from hydrogen self-diffusion in olivine, as it requires transport of hydrogen-bearing defect associates, which are rate limited by the transport of slower defects, such as metal vacancies.

### **4.2.5 Conclusions**

The hydrogenation experiments reported in this study provide further insight into the interactions of olivine with water under conditions appropriate to the interior of the Earth. In particular, the following results were obtained:

1. Very rapid hydrogenation with fastest diffusion parallel to [100], as described previously by Mackwell and Kohlstedt (1990) for iron-bearing olivine, does not occur in iron-free forsterite, supporting the model of proton-polaron exchange for this process.
2. Hydrogenation results for forsterite with fastest diffusion parallel to [001] are similar to previous data for olivine (Kohlstedt and Mackwell 1998), which were interpreted as incorporation of proton-metal vacancy associated defects. These new results are thus consistent with incorporation of water-derived species rate limited by the diffusivity of metal vacancies. It is also conceivable that the mobile defects are hydrogen-silicon vacancy associates.

3. Diffusion is only modestly slower in forsterite than in olivine under the same conditions. Thus, the transport of water-derived species in olivine is not strongly coupled to the iron concentration, in contrast to measurements of hydrogen solubility, which increase with increasing iron content (Zhao et al. 2001).

4. Iron content also does not affect anisotropy of diffusion, with results for both iron-free forsterite and iron-bearing olivine yielding

$$\tilde{D}_{[001]} > \tilde{D}_{[010]} > \tilde{D}_{[100]}$$

5. From the experimental results and assuming a model of hydrogen-metal vacancy defects, where the vacancies are the slower diffusing species, metal vacancy diffusion parallel to each crystallographic direction in forsterite can be described by

$$D_{V_{Me}}^{[001]} = 10^{-(3.8 \pm 1.3)} \exp [-(210 \pm 33)/RT]$$

$$D_{V_{Me}}^{[010]} = 10^{-(4.6 \pm 1.2)} \exp [-(205 \pm 31)/RT]$$

$$D_{V_{Me}}^{[100]} = 10^{-(4.3 \pm 1.6)} \exp [-(225 \pm 40)/RT]$$

*(activation energies in kJ/mol)*

7. Equilibration of forsterite or olivine crystals to a change in the hydrothermal environment can be expected to take significantly longer than predicted from hydrogen self-diffusion in olivine, as it requires transport of hydrogen-bearing defect associates, which are rate limited by the transport of slower defects, such as metal vacancies.

### **4.3. Dehydration profiles in mantle-derived olivine**

#### **4.3.1. Introduction**

As demonstrated in the previous sections on the kinetics of hydration in olivine and forsterite (section 4.1 and section 4.2), dissolved water would be lost in just a few hours on ascent from depth in the Earth at temperatures over 800°C. However, to date, such a process was never recognized or reported for mantle-derived olivine in xenoliths. This section presents the first evidence of a signature of hydroxyl diffusion in xenolithic iron-bearing olivine from garnet  $\pm$  spinel peridotite in alkali basalt from Pali-Aike in Patagonia, South America. The application of hydroxyl diffusion profiles as a tool to estimate magma ascent rate and implication for the water distribution within Earth's upper mantle is also discussed.

#### **4.3.2. Geological setting and sample characterization**

##### *The Pali-Aike volcanic field*

The Pali-Aike volcanic field (PAVF) is located in southernmost South America at the border between Argentina and Chile in Patagonia (Figure 4.3.1). This volcanic plateau was previously described and studied by Stern and co-workers (Skewes and Stern, 1979; Stern et al., 1990; Selverstone and Stern, 1983; Kilian et al., 2002). The PAVZ is affiliated to the Plio-Quaternary Patagonian Plateau lava field and is located over a slab-window (Kilian et al., 2002; D'Orazio et al., 2001) at around 200 km from the austral volcanic zone (AVZ). The associated lithosphere appears to be relatively thin (<100km, Stern et al., 1999). The PAVF is constituted of Pleistocene to Recent alkali olivine basalts, which contain various xenoliths as garnet  $\pm$  spinel lherzolites and harzburgite, phlogopite-bearing peridotite (Stern et al., 1999; Stern et

al., 1989), mafic granulites but also sedimentary and granitic rocks (Selverstone and Stern, 1983). This work is focused on the garnet  $\pm$  spinel lherzolite xenoliths. Relating to the host magma, no magma chamber has been located where the xenoliths could acquire a new hydrous/anhydrous feature; the temperature of the primary magma was estimated by D’Orazio et al., (2000) to be between 1200 and 1290°C using the  $\text{Fe}_2\text{O}_3/\text{FeO}$  ratio within olivine (i.e., phenocryst cores-liquid using the geothermometer of Leeman and Scheidegger (1997). The absence of amphibole in the basalt indicates that the alkali basalt was under-saturated in water. Samples from the PAVF were chosen because of the recentness of the lava eruptions and, therefore, the fresh state of these peridotite xenoliths.

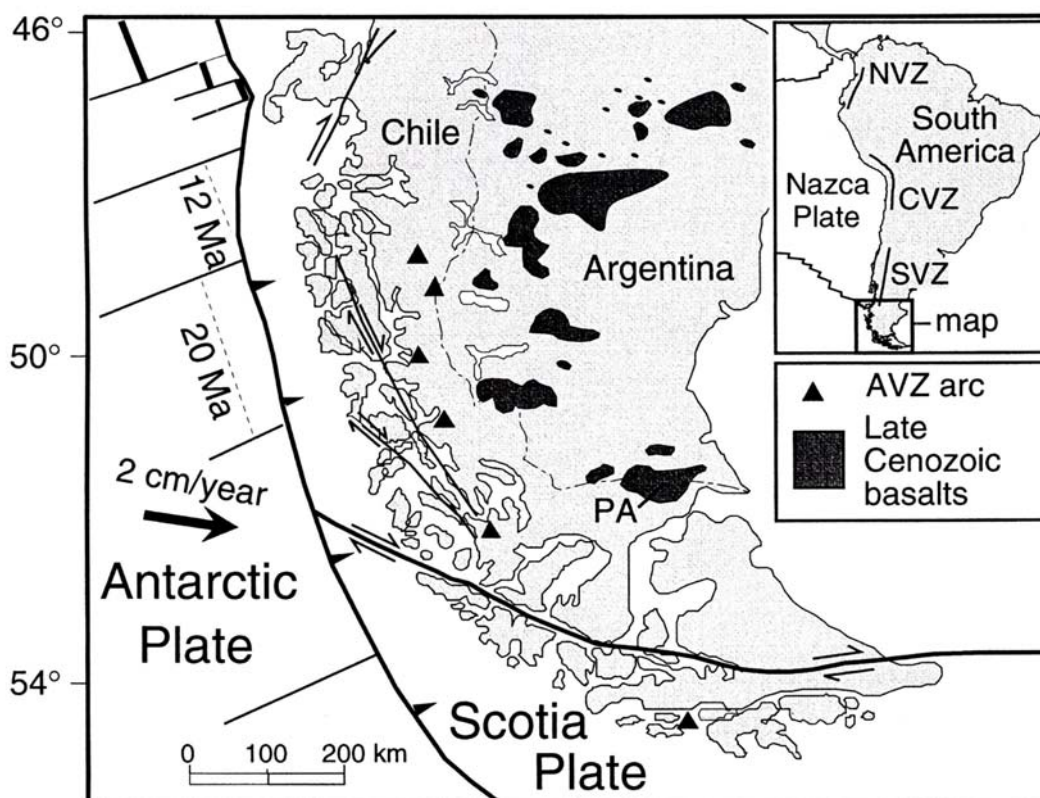


**Figure 4.3.1** Map modified from Stern et al. (1999) showing the location of the Pali-Aike volcanic field (PAVF) in southernmost South America with regards to the other parts of the Patagonian Plateau lava field. NVZ, CVZ, SVZ and AVZ indicate North-, Central-, South- and Austral-Volcanic Zone respectively. Main tectonic features from Cande and Leslie (1986).

*Lherzolite and olivine samples*

The ultramafic xenoliths include pyroxenite, olivine websterite, and garnet  $\pm$  spinel-bearing peridotite. Figure 4.3.2 shows a representative micrograph of the lherzolite Palix-1, where the white crystals are olivine, dark grey and pale grey are Cr-diopside and orthopyroxene, respectively. The mantle xenoliths have dimensions between 2 cm and 40 cm. The texture is mostly granoblastic and only some parts show porphyroclastic textures (Mercier and Nicholas, 1975); these parts were avoided when selecting olivine grains for study. The mineralogical assembly is highly magnesian and consists of Mg-olivine, orthopyroxene, diopside, rare spinel and Cr-pyrope which contains hydrous and brownish glassy inclusions and secondary spinel-rich kelpytic rims.

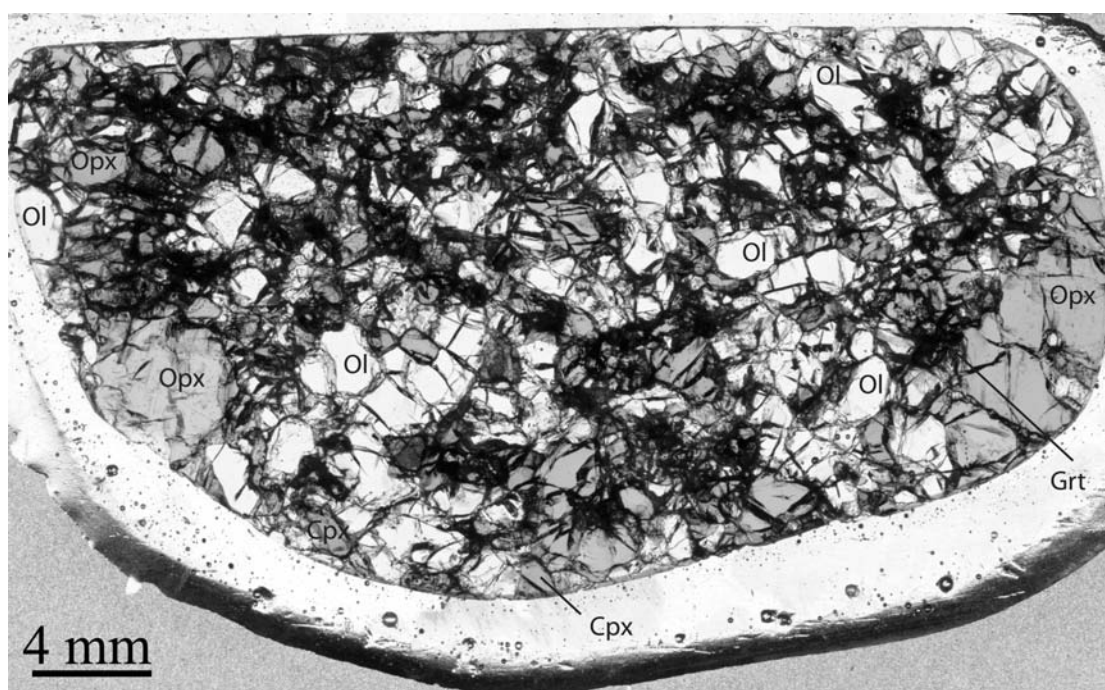


**Figure 4.3.2** Photomicrograph of a garnet lherzolite. Thin section is  $500 \pm 5 \mu\text{m}$  thick, which is a suitable thickness for FTIR analysis on olivine. Minerals are Ol = olivine (white, pale green in transmitted light (TL), Cpx = Cr-diopside (grey, emerald green in TL), Opx = Mg-rich orthopyroxene (grey, green in TL), Grt = Cr-pyrope (dark grey, fuschia pink to reddish in TL).

A previous geochemical study (Stern et al., 1999) indicates that these xenoliths have major element compositions similar to Ringwood's pyrolite (Ringwood, 1962a, 1962b; Green and Fallon, 1998). Trace element and isotopic compositions are similar to the global asthenospheric source of mid-ocean ridge basalts (Stern et al., 1999). However, core compositions of minerals in the garnet-lherzolite indicate equilibrium temperatures between 970°C and 1160°C, and pressures range from 1.9–2.4 GPa, corresponding to ~70 km deep in the subcontinental lithosphere.

The olivine single crystals are of very good quality with an average grain size around 2.4 mm, reached 1 cm in a few spinel-bearing lherzolites. The grains are not affected by serpentinization, weathering effects, secondary grain boundary re-crystallization, show no oriented foliation, and no effect due to melt infiltration (*i.e.* host basaltic glass). In addition, the low occurrence of inclusions and cracks makes those olivine grains highly suitable for FTIR analysis.

#### *Sample preparation*

Two preparation methods were used to study the hydroxyl content in xenolithic olivine from the Pali-Aike volcanic field (Patagonia). (1) A thick slide was randomly cut in a xenolith after impregnation using crystal bond or super glue. Afterwards, a doubly polished section was prepared from the slide, with an approximated thickness around 500µm, which was found to be suitable for NIR. After an acetone bath for at least 12 hours, the sample was ready for FTIR analysis, (2) Few single grains were separated from the parent-xenolith and then oriented using a single crystal X-ray diffractometer "HUBER SNC 9000" operating with Mo  $K\alpha$  radiation. One crystal, PA-3, was cut with faces perpendicular to each axis to form a prism (883 x 1090 x 980 µm) and carefully polished (using diamond films, from 30µm to 1µm grain size). The second olivine grain, PA-7, was polished only to have two parallel faces perpendicular to [010].

After infrared analysis, xenolith pieces and olivine grains were mounted in epoxy resin and again carefully polished with diamond powder for major elements analysis with a Cameca SX50 electron microprobe (section 2.2). Multi-component profiles were measured along the same direction as for the NIR profile analysis, but these analyses did not reveal chemical differences between core and rims in olivine grains.

### *Chemical compositions*

Table 4.3.1 presents selected EMPA chemical analyses of every mineral phase occurring in the xenoliths. These analyses are comparable to previous EMPA analyses (Skewes and Stern, 1979; Stern et al., 1989; D’Orazio et al., 2000) and are consistent with garnet  $\pm$  spinel lherzolite peridotite with a bulk composition corresponding to Ringwood’s pyrolite (Ringwood, 1962a, 1962b, Ringwood and Major, 1966).

### **4.3.3. Infrared spectra and water contents**

#### *Olivine*

Figures 4.3.3-A and 4.3.3-B show unpolarized and polarized FTIR spectra for olivine single crystal PA-3, respectively. The major O-H absorption band, which is also the most important infrared bands in terms of water content, is located at  $3572\text{ cm}^{-1}$  with the electric vector, E, parallel to [100]. Two weak bands are visible around  $3572$  and  $3525\text{ cm}^{-1}$  with E parallel to [010] and with E parallel to [001]. The IR spectra show two unusual and strongly polarized bands at  $3330$  and  $3228\text{ cm}^{-1}$  with E parallel to [001]. Details of the infrared band positions from olivine PA-3 and also from a previous study on experimentally hydrated mantle-derived olivine (Bai and Kohlstedt, 1993) are given in Table 4.3.2. The use of unpolarized and polarized infrared radiation permits to apply different well-known and recognized calibrations: the calibration of Paterson (1982) for unpolarized and polarized spectra and the recent calibration of Bell et al. (2003) specifically for iron-bearing olivine ( $\text{Fo}_{90}$ ). The total water concentrations and distribution within olivine samples are given in Tables 4.3.3 and Table 4.3.4.

In addition, the TEM observations were carried out in the central hydrated regions of the sample PA-5 as well as in the anhydrous sample edges demonstrated that the olivine Pa-5 was free of precipitates, linear and planar defects (see TEM documentation in appendix 3).

### 4.3. Results: Dehydration profiles in mantle-derived olivine

**Table 4.3.1** Selected EMPA for minerals from Pali-Aike xenoliths.

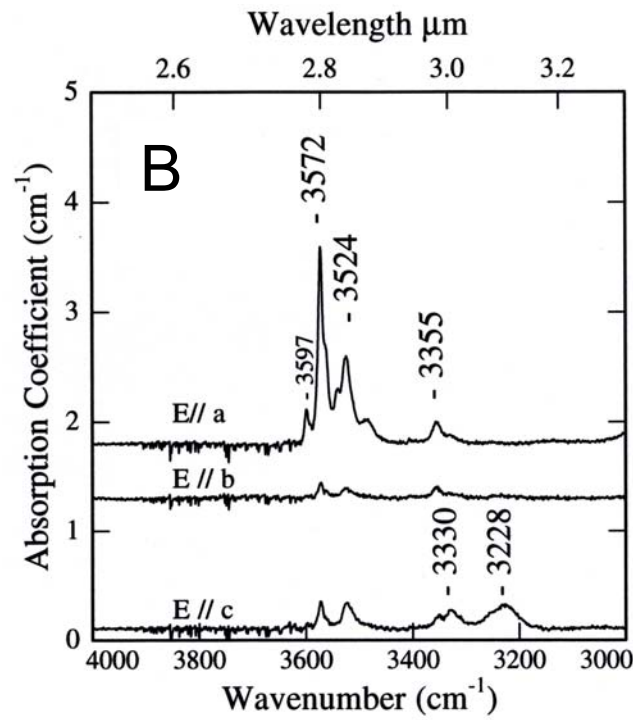
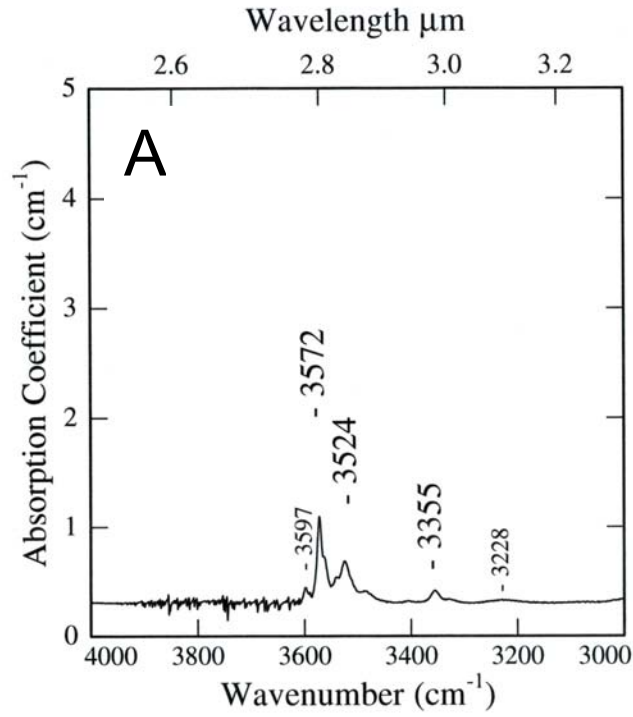
Xenolith sample	LS 33	LS 33	PA-sp	TMO	PA-1	PA-1	LS 33	PA-sp
Mineral	olivine	olivine	olivine	olivine	olivine	olivine	opx	opx
Element (wt.%)								
SiO <sub>2</sub>	41.30	41.49	41.34	40.60	40.91	40.77	55.14	54.68
TiO <sub>2</sub>	<DL	<DL	0.02	0.01	<DL	<DL	0.15	0.08
Al <sub>2</sub> O <sub>3</sub>	0.05	0.06	0.01	<DL	0.04	0.03	4.33	3.64
Cr <sub>2</sub> O <sub>3</sub>	0.01	0.03	0.02	<DL	0.02	0.06	0.58	0.41
FeO	9.22	9.06	8.78	9.83	9.52	9.72	5.88	6.04
MnO	0.09	0.08	0.11	0.10	0.11	0.12	0.10	0.13
MgO	49.66	50.03	50.52	49.99	49.70	49.82	33.15	34.68
CaO	0.11	0.09	0.02	0.06	0.06	0.05	1.17	0.28
Na <sub>2</sub> O	<DL	<DL	<DL	0.01	<DL	0.02	0.18	0.04
NiO	0.30	0.44	0.31	0.38	0.38	0.49	0.13	0.05
Sum	100.74	101.28	100.86	100.97	100.75	101.07	100.81	100.02
Si	1.00	1.00	1.00	0.99	1.00	0.99	1.89	1.89
Ti	-	-	0	0	-	-	0	0
Al	0	0	0	-	0	0	0.18	0.15
Cr	0	0	0	-	0	0	0.02	0.01
Fe	0.19	0.18	0.18	0.2	0.19	0.2	0.11	0.17
Mn	0	0	0	0	0	0	0	0
Mg	1.8	1.8	1.81	1.81	1.8	1.8	1.70	1.79
Ca	0	0	0	0	0	0	0.04	0.01
Na	-	-	-	0	-	0	0.01	0
Ni	0.01	0.01	0.01	0.01	0.01	0.01	0	0
Sum	3.00	3.00	3.00	3.01	3.00	3.01	3.95	4.03
Mg#	90.57	90.78	91.08	91.08	91.08	91.08		
Cr#								
Ens#							91.61	90.63
Fs#							2.31	0.52
Wo#							6.08	8.85

<DL=below detection limit

**Table 4.3.1 (second part)** Selected EMPA for minerals from Pali-Aike xenoliths.

Xenolith sample	TMO	PA-1	PA-1	PA-sp	TMO	PA-1	TMO	PA-sp
Mineral	opx	opx	diop	diop	diop	garnet	garnet	spinel
Element (wt.%)								
SiO <sub>2</sub>	55.57	55.22	52.36	51.70	52.14	42.25	42.21	0.09
TiO <sub>2</sub>	0.16	0.07	0.45	0.47	0.56	0.16	0.17	0.11
Al <sub>2</sub> O <sub>3</sub>	3.22	3.72	5.26	6.23	5.52	22.73	22.92	52.13
Cr <sub>2</sub> O <sub>3</sub>	0.43	0.52	1.33	1.21	1.06	1.68	1.12	15.58
FeO	6.29	6.12	3.13	2.04	3.06	7.55	7.78	11.39
MnO	0.17	0.09	0.06	0.01	0.06	0.29	0.35	<DL
MgO	33.82	33.56	15.86	14.68	15.87	20.88	20.92	19.65
CaO	0.66	0.74	19.02	21.13	18.61	4.99	4.82	0.00
Na <sub>2</sub> O	0.11	0.12	1.74	1.74	1.99	0.02	0.04	0.01
NiO	0.10	0.14	0.03	<DL	0.07	0.03	0.03	0.38
Sum	100.51	100.20	99.24	99.93	98.93	100.57	100.34	99.33
Si	1.91	1.91	1.91	1.89	1.90	5.97	5.97	<DL
Ti	0	0	0.01	0.01	0.02	0.02	0.02	<DL
Al	0.13	0.15	0.23	0.27	0.24	3.78	3.82	1.64
Cr	0.01	0.01	0.04	0.03	0.03	0.19	0.13	0.33
Fe	0.17	0.18	0.10	0.06	0.09	0.89	0.92	0.25
Mn	<DL	<DL	<DL	<DL	<DL	0.03	0.04	<DL
Mg	1.74	1.73	0.86	0.80	0.86	4.39	4.41	0.78
Ca	0.02	0.03	0.74	0.83	0.73	0.75	0.73	<DL
Na	<DL	<DL	0.06	0.06	0.07	<DL	<DL	<DL
Ni	<DL	<DL	<DL	<DL	<DL	<DL	<DL	0.01
Sum	4.01	4.01	3.95	3.95	3.95	16.03	16.04	3.01
Mg#								75.46
Cr#								16.70
Ens#	89.47	89.43	50.70	47.34	51.25			
Fs#	1.26	1.42	43.69	48.97	43.21			
Wo#	9.33	9.15	5.61	3.70	5.54			

&lt;DL=below detection limit.



**Figures 4.3.3A/B** Unpolarized (A) and polarized (B) infrared spectra for olivine PA-3, with different orientations of the electrical vector  $E$ .

**Table 4.3.2** Hydroxyl band positions for different orientations of the infrared electric vector (E) in olivine Pa-3 from Palix-1 xenolith and from experimentally hydrated San Carlos olivine.

Pali-Aike PA-3 <sup>1</sup>			San-Carlos <sup>2</sup>
[100]	[010]	[001]	Unpolarized
			3637
			3623
			3612
3597			3598
3594			
3573	3573	3573	3576
			3565
3539			3542
3529			3529
3524	3524	3524	
3487			3483
			3459
			3443
			3424
			3389
3355	3355	3355	3354
		3330	3329
		3228	3236*

Wavenumber resolution  $\pm 2 \text{ cm}^{-1}$

\* indicates a weak infrared band

<sup>1</sup> olivine samples from Pali-Aike xenolith, this study

<sup>2</sup> experimentally hydrated xenolithic olivine from San Carlos, Arizona (Bai and Kohlstedt, 1993)

### 4.3. Results: Dehydration profiles in mantle-derived olivine

**Table 4.2.3** Water content in olivine from Pali-Aike xenoliths using the calibration of Paterson (1982).

Sample	Xenolith Ref §	Xenolith type	Water content £ wt ppm H <sub>2</sub> O (H/10 <sup>6</sup> Si)
Olivine PA-1	Palix-1	Lherz +grt	16 ± 5 (258 ± 80)
Olivine PA-2	Palix-1	Lherz +grt	10 ± 3 (163 ± 50)
Olivine PA-3	Palix-1	Lherz +grt	9 ± 3 (147 ± 50) *
Olivine PA-4	Palix-1	Lherz +grt	6 ± 2 ( 98± 33)
Olivine PA-5	LS33	Lherz +grt	8 ± 3 (130 ± 50 )
Olivine PA-6	TMO	Lherz +grt	11 ± 4 (180 ± 65)
Olivine PA-7	Pak-1	Lherz +sp	13 ± 4 (195 ± 65 ) *
Olivine PA-ph	LLS-1	Harz+phlo	9 ± 4 (147 ± 65)

All the water contents reported for olivine are the maximal water concentration observed in the olivine core. Abbreviations: lherz= lherzolite xenolith, grt=garnet, sp=spinel, harz=harzburgite xenolith, phlo=phlogopite. § xenolith reference for comparison with Stern et al., (1986, 1999). £ water content using the calibration of Paterson (1982), Eq. (10) with  $\xi = 1/3$ . \*water content for oriented crystal using the calibration of Paterson (1982), Eq. (10) with  $\xi = 1$ .

**Table 4.2.4** Water content from polarized IR spectra in olivine PA-3 and PA-7 and for different calibrations available for olivine.

Sample	Water content * [100]+[010]+[001]=total water in wt ppm H <sub>2</sub> O	Water content # [100] +[010]+[001]=total water in wt ppm H <sub>2</sub> O
Olivine PA-3	5.6+0.6+3.0= <b>9.2 (± 3)</b>	13.7+2.4+7.52= <b>23.62 (± 2)</b>
Olivine PA-7	8.6+1+3.7= <b>13.3 (± 4)</b>	24+3+14= <b>41(± 4)</b>

\*water content using the calibration of Paterson (1982), Eq. (10) with  $\xi = 1$  and on oriented sample. # water content using Eq. (7) and the calibration of Bell et al. (2003) on oriented olivine sample.

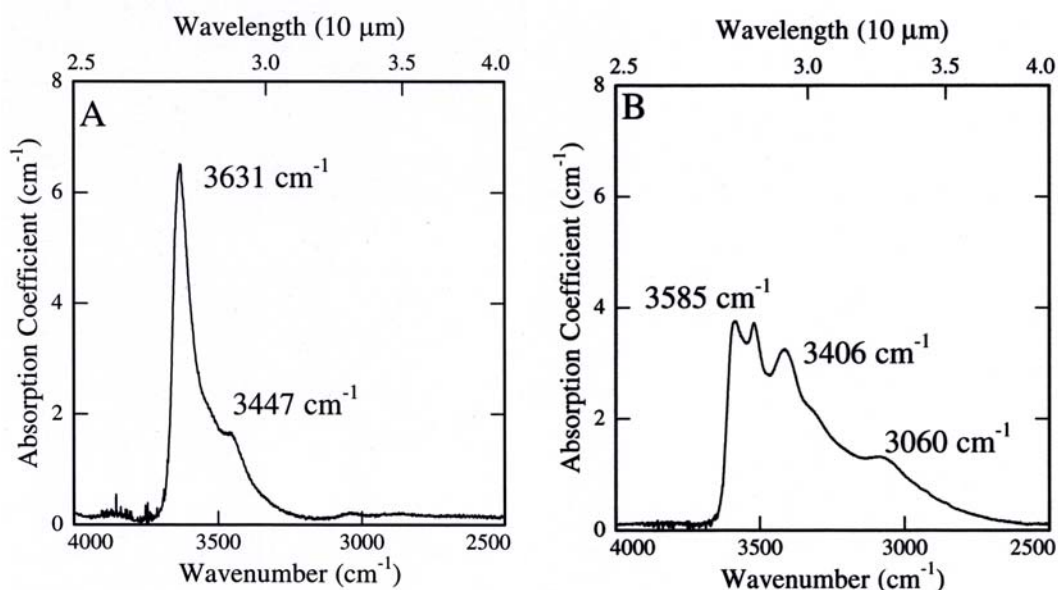
#### *Pyroxenes*

While hydrogen in Cr-Diopside and orthopyroxene is not the focus of this study, these minerals within the xenoliths contain trace amounts of water. Two unpolarized IR spectra are shown in Figure 4.3.4-A and Figure 4.3.4-B for diopside and orthopyroxene, respectively, from Palix-1 lherzolite. The spectra are typical for peridotite xenolith pyroxene (Bell et al., 1995). The main infrared band of diopside presents is around  $3631\text{ cm}^{-1}$  with a shoulder around  $3447\text{ cm}^{-1}$ . Orthopyroxene has five infrared bands, located at  $3585\text{ cm}^{-1}$ ,  $3522\text{ cm}^{-1}$ ,  $3406\text{ cm}^{-1}$ ,  $3310\text{ cm}^{-1}$  and  $3060\text{ cm}^{-1}$ . The water concentrations for various diopside and enstatite crystals are given in Table 4.3.5. Cr-diopside is the main hydrous phase in these xenolith assemblies, with water contents up to  $410 \pm 150\text{ wt ppm}$  (sample D-1 in the garnet-bearing lherzolite Palix-1). The orthopyroxene from the same lherzolite sample is also relatively rich in water with a concentration up to  $310\text{ wt ppm H}_2\text{O}$ . Contrary to olivine, the hydroxyl distribution is homogeneous in the different pyroxenes and for different peridotite samples, suggesting either that no hydrogen was lost during entrainment and transport of the xenoliths, or that the hydrogen has completely reequilibrated during transport. The observations of diffusion profiles in the olivine suggest that complete reequilibration had not occurred.

#### *Accessory phases: garnet and spinel*

The garnets within the xenoliths are poorly preserved. They contain many cracks due to the decompression during transport, and the borders are frequently rich in secondary spinel (i.e., resulting from phase transition) and brownish hydrous glassy inclusions. Despite the difficulties in finding suitable places for measurements, FTIR analyses on the few clear parts (free of inclusions, cracks, of adequate thickness and sufficiently large area ( $\sim 30\mu\text{m}$ )) show that the garnets are absolutely dry within the detection limit of the FTIR measurements ( $\sim 1\text{H}/10^6\text{ Si}$ ,  $\ll 1\text{ wt ppm H}_2\text{O}$ ).

The spinels were too fine-grained as well as too dark (opaque) to perform accurate infrared measurement.



**Figures 4.3.4/A and 4.3.4/B** Unpolarized infrared spectra for diopside (A) and orthopyroxene (B) from Palix-1 garnet-bearing lherzolite.

**Table 4.3.5** Water content in pyroxenes from Pali-Aike xenoliths.

Sample	Xeno. ref\$	Xeno. type	wt ppm H <sub>2</sub> O (H/10 <sup>6</sup> Si)
Diopside D-1	Palix1	Lherz +grt	416 ± 150 (6,794 ± 2,450)
Diopside D-2	LS33	Lherz +grt	255 ± 85 (4,164 ± 1,388)
Diopside D-3	TMO	Lherz +grt	350 ± 120 (5,715 ± 1,960)
Diopside D-4	Pak-1	Lherz +sp	151 ± 65 (2,450 ± 1,061)
Enstatite En-1	Palix1	Lherz +grt	310 ± 103 (5,062 ± 1,682)
Enstatite En-2	LS33	Lherz +grt	190 ± 65 (3,103 ± 1,061)
Enstatite En-3	TMO	Lherz +grt	250 ± 60 (4,083 ± 980)
Enstatite En-4	Pak-1	Lherz +sp	70 ± 36 (1,143 ± 588)
Enstatite En-5	LLS-1	Harz + phlo	120 ± 50 (1,960 ± 817)

Abbreviations are given for: phlo=phlogopite, lherz= lherzolite xenolith, harz=harzburgite xenolith, grt=garnet, sp=spinel.

\$ xenolith reference for comparison with previous works of Stern et al., (1989, 1999).

\* water content using Eq. (10) and the calibration of Paterson (1982).

#### 4.3.4. Diffusion profiles in olivine

##### *How to explain water heterogeneity in olivine ?*

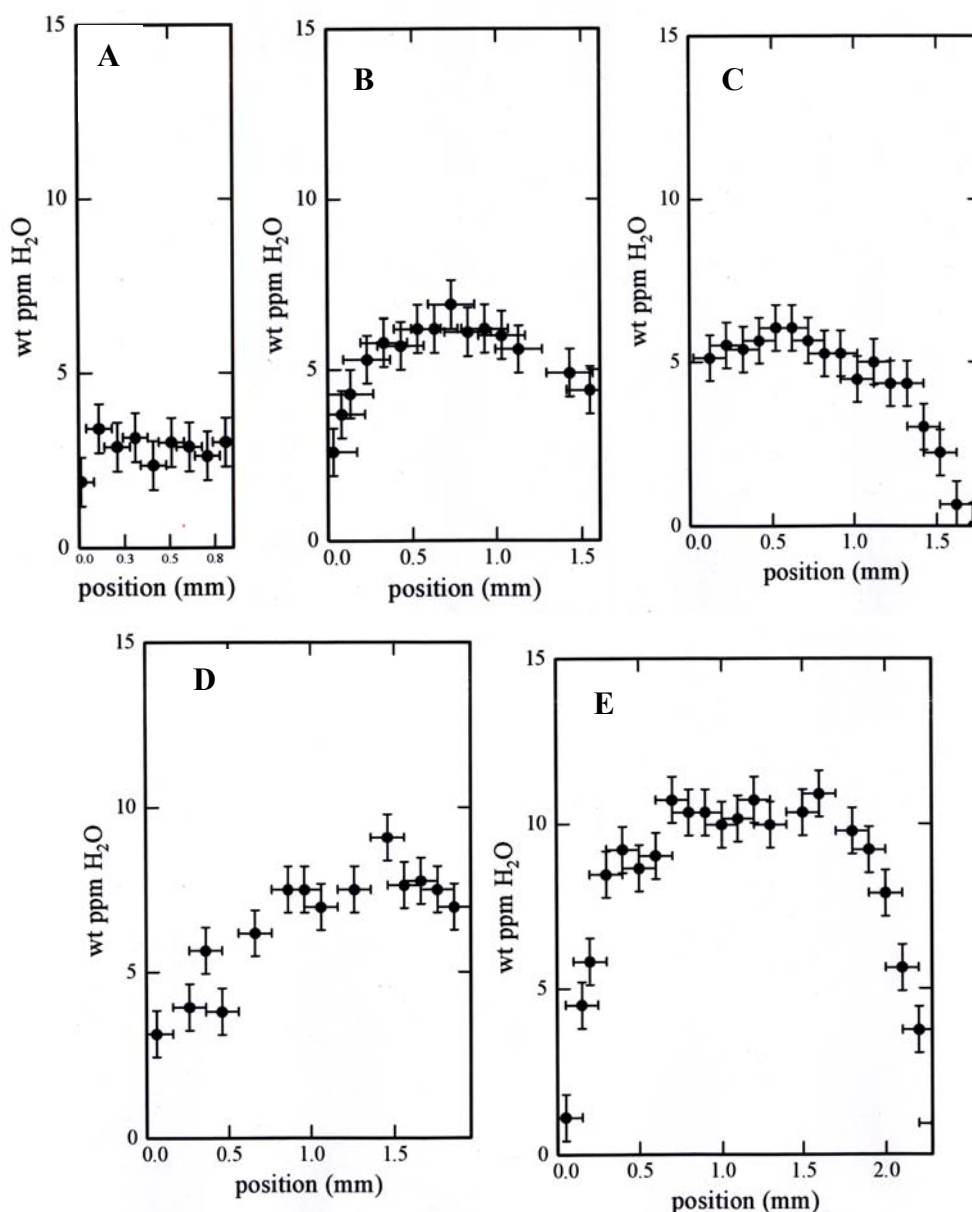
From diffusion experiments on the NAMs from the upper mantle, it is known that the isotropic diffusion coefficient of hydrogen in garnet is slower than the fastest direction of diffusion in olivine. Also, diffusion coefficients of hydrogen in orthopyroxene and clinopyroxene are slower than the fastest direction of diffusion in olivine (at 1000°C, values are given in Table 1.2). The observations from Pali-Aike lherzolites are consistent with these experimental results that olivine is dehydrating and therefore presents a heterogeneous water distribution, while pyroxene has yet to start to dehydrate. The details of the heterogeneity of water distribution within olivine are discussed in the following sections.

As predicted by Hirth and Kohlstedt (1996), the water partition coefficient between olivine and garnet is expected to be around 1:1. This is in contradiction to the observations from these Pali-Aike xenoliths, where olivine still contains water but not garnet. This may be due to the fact that the hydrogarnet substitution becomes unfavourable at high pressure (Withers et al., 1998). Alternatively, the low water content of garnet may be related to the partial transformation in spinel.

##### *Unoriented profiles*

Figures 4.3.5-A-B-C-D-E give a series of five infrared profiles across five different crystals of olivine (these profiles were obtained from IR analyses on the thick sections and not from separates grains) with the water content as a function of the position along the olivine crystals (olivine PA-16, 0.86 mm long ; olivine PA-14, 1.61 mm long ; olivine PA-18, 1.77 mm long, olivine PA-2, 1.96 mm long; olivine PA-1, 2.26 mm long for Figure 5.- A, B, C, D E, F respectively). These infrared profiles are comparable to hydroxyl diffusion profiles generated experimentally by hydration or dehydration by Mackwell and Kohlstedt (1990) and as presented in the section 4.2 of this thesis. This series of hydroxyl profiles clearly shows that rims are depleted in hydroxyl. Therefore, the olivines were dehydrating, losing hydrogen to the entraining basalt. Notice that for length scales less than 0.5 mm (i.e., the central part of a grain),

the water content appears to be extremely low and the distribution, uniform. In general, the maximum water content occurs in the largest grains. The asymmetrical shape of Figure 4.3.5-B, -C and -D are due to conchoidal fractures or irregularities at the edges of the grains. Figure 4.3.5-E is remarkable for the quality of the profile, justifying a full IR analysis of the hydroxyl distribution within the crystal.



**Figures 4.3.5 A/B/C/D and /E** Unpolarized infrared profiles across different unoriented olivine crystals (A) olivine PA-16, 0.86 mm; (B) olivine PA-14, 1.61 mm; (C) olivine PA-18, 1.77mm, (D) olivine PA-2, 1.96 mm; (E) olivine PA-1, 2.26 mm.

*Oriented profiles*

Two large grains of gem quality olivine were separated and oriented using a 4-circle single crystal X-ray diffractometer. The first crystal, olivine Pa-3, was polished with faces perpendicular to each axis to obtain a cube. Polarized IR measurements were made with E parallel to all three directions (Figure 4.3.3-B). By grinding orthogonal faces on the crystal, most of the grain near the grain boundary was removed, limiting the length of hydroxyl profiles. The second grain, olivine Pa-7 is only doubly polished to obtain a (010) plate in order to measure IR profiles along [100] and [001], which are as long as possible (to conserve as much as possible of the original grain boundary). Thus, olivine Pa-7 presents much more complete profiles than olivine Pa-3. Figure 4.3.6 presents a series of polarized spectra from olivine Pa-7, with E parallel to [100] and spectra taken along the [100] direction, which confirms the observations from unoriented profiles: the grain borders are depleted in hydroxyl.

Figure 4.3.7 and Figure 4.3.8 show water content plotted as a function of the position along the crystal axes for olivine Pa-7, with E parallel to the [100] axis (Figure 4.3.7) and to the [001] axis (Figure 4.3.8). The water contents reported in y-axis were obtained with the calibration for olivine from Bell et al. (2003).

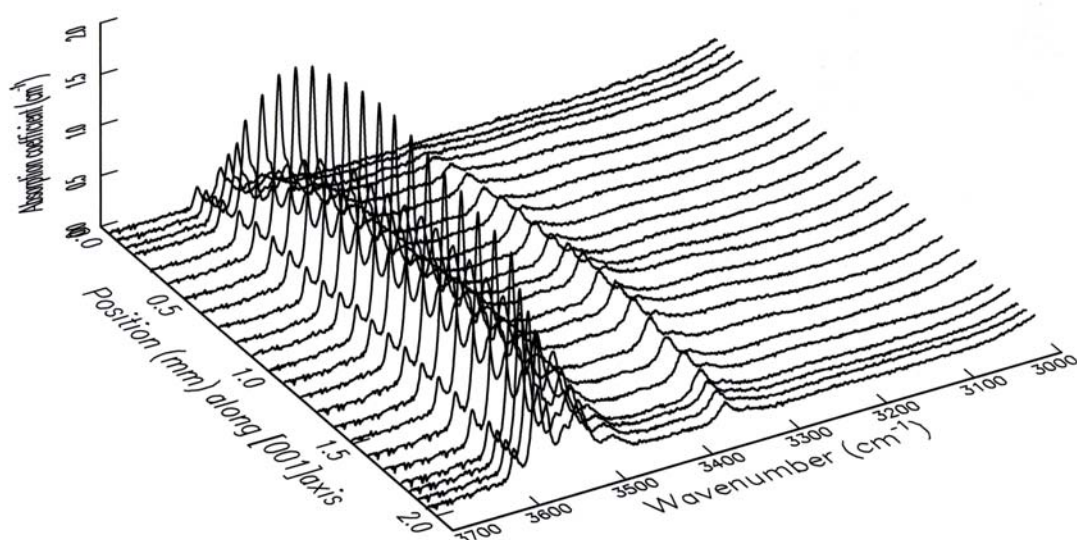


**Figure 4.3.6** Series of polarized infrared spectra with E // [100] along the [100] axis within olivine Pa-7.

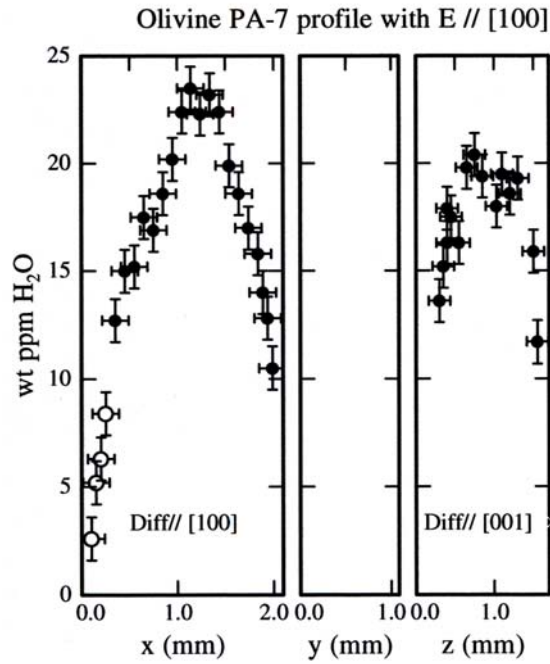


**Figure 4.3.7** Polarized infrared profile across olivine Pa-7 with E // [100]. The *open circles* indicate points along a short bevel adjacent to the grain boundary along [100]. Thus the thickness was over estimated compare to the rest of the profile, leading to underestimation of the water content in the first 300  $\mu$ m in the left-hand profile.

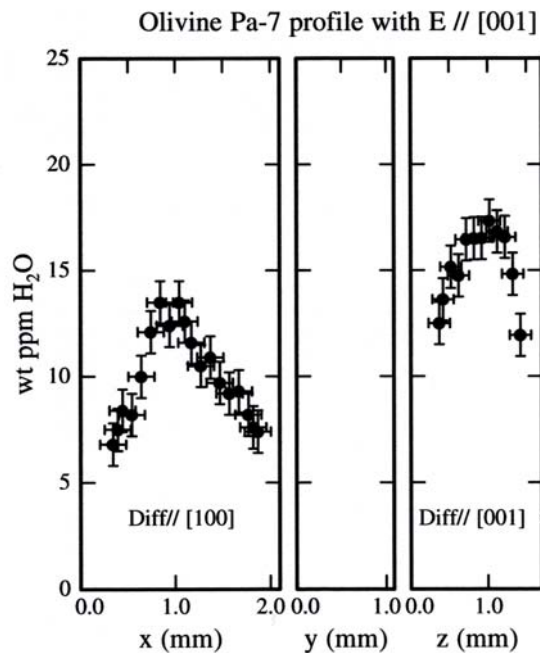


**Figure 4.3.8** Polarized infrared profile across olivine Pa-7 with E // [001].

Comparison between the profiles for E // [100] shows that diffusivity along the [100] axis is slightly faster than along [001], while profiles with E // [001] clearly show that diffusion along [100] is faster than diffusion along the [001] axis. These qualitative observations on the anisotropy of diffusion suggest that this olivine lost its water for a part by redox exchange process. Figure 4.3.9 is identical to Figure 4.3.8 but gives additional details of the water concentration partitioning between high- and low-wavenumber IR bands.

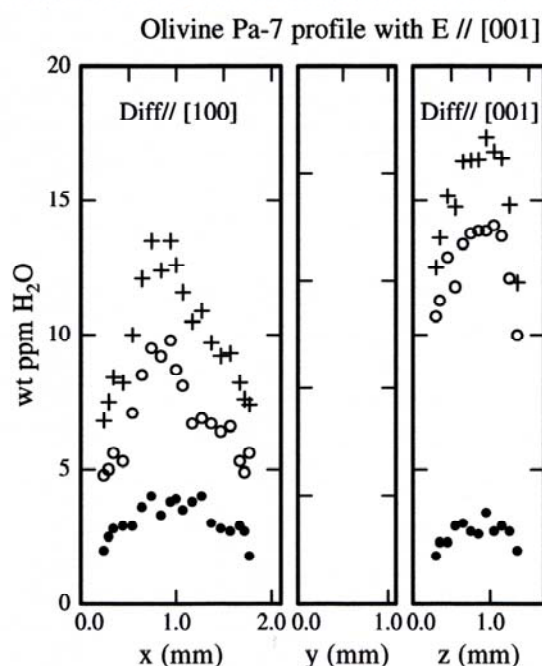


**Figure 4.3.9** Polarized infrared profiles across olivine Pa-7 with E // [001]. The *small crosses* represent the total water content, the *closed circles* represent water content from integration between 3650-3450 cm<sup>-1</sup> and the *open circles* represent water content from integration between 3450-3100cm<sup>-1</sup>.

In order to determine whether the defects associated with IR bands diffuse at the same rate, the contribution in % of the groups to the total hydroxyl content was calculated for each analysed point and for both IR calibrations (Table 4.3.6). With E // [001], group 2, which represents integration between 3450-3100 cm<sup>-1</sup>, is dominant. The distribution between the two groups remains relatively constant across the profile as shown in Figure 4.3.9. Therefore the defects associated with both sets of bands have a similar diffusivity. Thus, the diffusing defects may be the same; even though the sites associated with the various bands in the IR spectra are different.

**Table 4.3.6** Water distribution between high- and low-wavenumber groups of IR bands from olivine Pa- 7 using both Paterson (1982) and Bell et al. (2003) calibrations.

	Profile with E// [001] and diffusion along	Group 1 3650-3450 cm <sup>-1</sup>	Group 2 3450-3100 cm <sup>-1</sup>	Ratio Group2/Group1
		% of the total water content		
Calibration of	along [100]	49±4	51 ±4	1 ± 0.1
Paterson (1982)	along [001]	30.2 ± 2.3	69.8 ± 2	2.31 ± 0.04
Calibration of	along [100]	31 ± 3	69 ± 3	2.3 ± 0.4
Bell et al. (2003)	along [001]	17±1.3	83 ± 1.3	4.88 ± 0.55

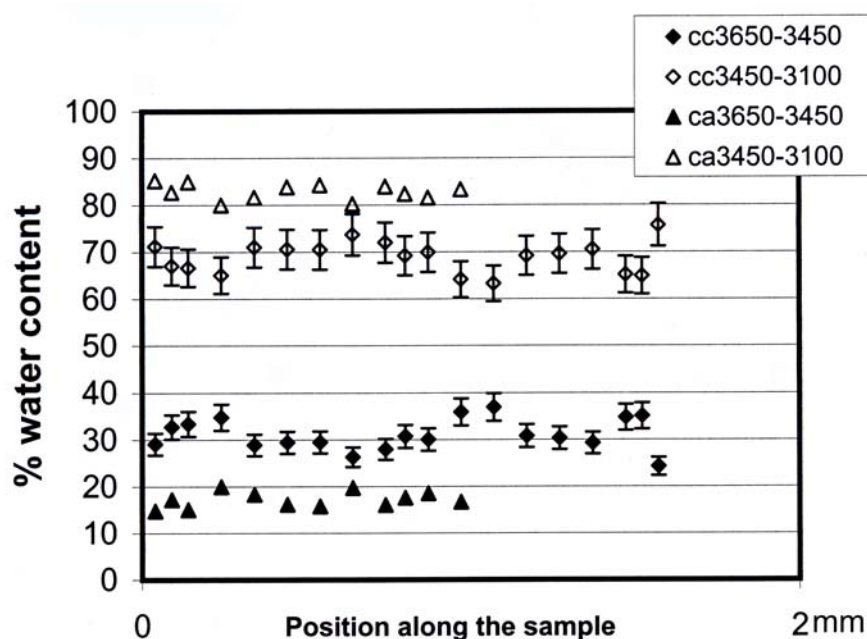
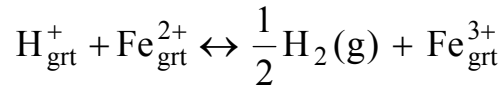


**Figure 4.3.10** Water content distribution in % between high- and low-wavenumber groups of IR bands from Pali-Aike olivine Pa-7 using the calibration of Bell et al., (2003). The distribution does not show significant differences in the rate of change for the two groups of bands, proving that the mobile species are diffusing at the same rate. *In the legend*, the first letter indicates the orientation of the E vector and the second, the direction of the profile, followed by the wavenumber range of integration.

### 4.3.5 Mössbauer analysis

Mössbauer analysis was performed on the garnet–lherzolite LS-33 by Catherine McCammon at Bayerisches Geoinstitut using the micro-Mössbauer spectrometer. Sample grains to be studied were identified using an optical microscope and selected on the basis of homogeneity. A hole with 500  $\mu\text{m}$  diameter drilled in a piece of 25  $\mu\text{m}$  thick Ta foil was centred over the grain to be studied, such that gamma rays passing not through the grain were absorbed by the foil. The thickness of the section (475  $\mu\text{m}$ ) combined with chemical compositions of the individual minerals gave the following estimated absorber thicknesses: 9 mg Fe/cm<sup>2</sup> for both olivine and garnet, 8 mg Fe/cm<sup>2</sup> for orthopyroxene and 4 mg Fe/cm<sup>2</sup> for clinopyroxene. Mössbauer spectra were recorded at room temperature (293 K) in transmission mode on a constant acceleration Mössbauer spectrometer with a nominal 370 MBq <sup>57</sup>Co high specific activity source in a 12  $\mu\text{m}$  Rh matrix (McCammon et al. 1991; McCammon 1994). The velocity scale was calibrated relative to 25  $\mu\text{m}$   $\alpha$ -Fe foil using the positions certified for National Bureau of Standards reference material no. 1541; line widths of 0.36 mm/s for the outer lines of  $\alpha$ -Fe were obtained at room temperature. The spectra were fitted using the commercially available fitting program NORMOS written by R.A. Brand (distributed by Wissenschaftliche Elektronik GmbH, Germany). Spectra took one day each to collect.

Resulting spectra are shown in Figure. 4.3.11. Ferric/ferrous iron ratio are the following: garnet 8 %, Cr-diopside 17%, enstatite 5 % and olivine contains less than 1%. These results are in agreements with normal iron ferric content of xenolith minerals except for garnet with 8 % in contrast to the 5% normally observed (C.McCammon, person. comm.). As garnet is the driest phase into LS-33 lherzolite, this high-Fe<sup>3+</sup> concentration agrees with the hypothesis of a redox exchange during dehydration of the garnet. Further analyses are necessary to confirm such a trend, where dehydration/hydration is strongly correlated to Fe<sup>3+</sup>. Such a model has been discussed by Dyar et al. (1996), Xia et al. (2000) and Johnson (2003), with the following reaction (Eq. 23) suggested by Bai and Kohlstedt (1992).



Eq. 23

Dehydration →

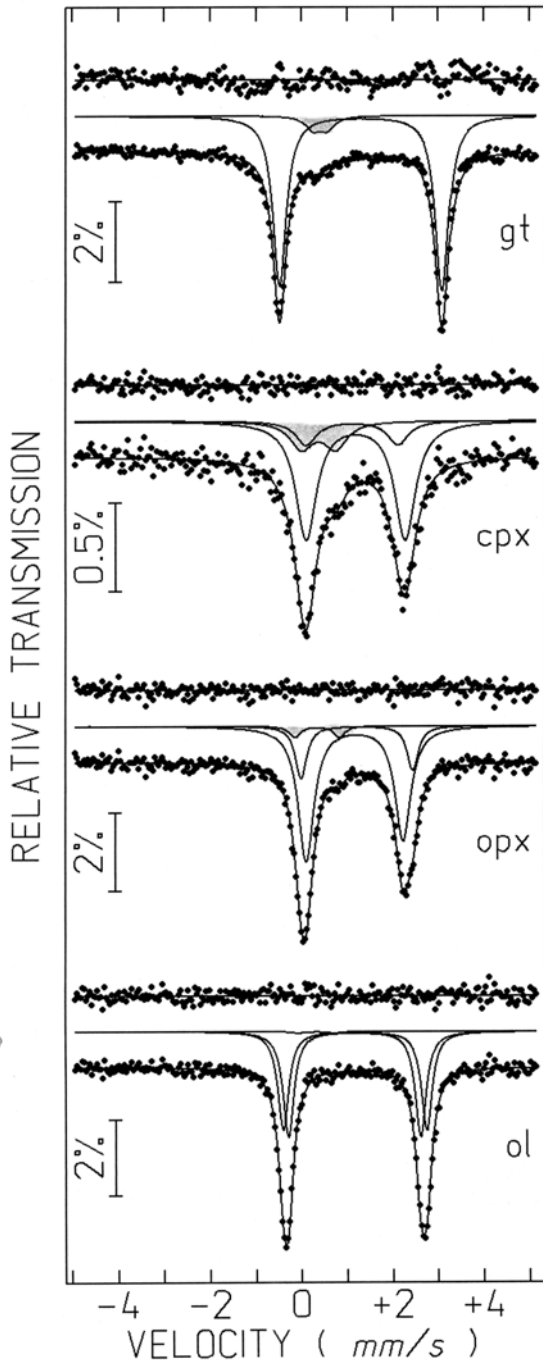


**Figure 4.3.11** Room temperature Mössbauer spectra from each mineral in the garnet-lherzolite LS-33. In each spectrum, the relative abundance of  $\text{Fe}^{3+}$  is represented by the grey subspectrum.

gt = garnet contains 8 % of  $\text{Fe}^{3+}$ , cpx = clinopyroxene-Cr-diopside contains 17%, opx = orthopyroxene-enstatite contains 5 % and ol= olivine contains  $\leq 1\%$ .

### 4.3.6. Discussion and implications for the upper mantle

#### *Water content and water partitioning within NAMs from Pali-Aike xenoliths*

Table 4.3.7 shows the water content ratio between olivine/clinopyroxene and olivine/orthopyroxene for the various xenoliths studied, where olivine are partial dehydrated (the maximum water contents observed were used for the calculations). Thus, these ratios underestimate the truth partitioning coefficient of water between olivine/clinopyroxene and olivine/orthopyroxene. As expected, the ratio given here are lower by about one order of magnitude than previous estimates by Hirth and Kohlstedt (1996) and Bolfan-Casanova (2000). Results for  $D_{ol/opx}$  from this study are about half of the value obtained by Koga et al. (2003), except for the phlogopite-bearing harzburgite. However, these ratios can be used in the future studies to identify dehydrated xenoliths by checking the relative amounts of water in the various mineral phases using FTIR.

**Table 4.3.7** Water partition coefficients for upper mantle minerals, from this study and other studies.

Xeno §	Sample	$D_{Ol/Cpx}$	$D_{Ol/Opx}$	References
Lherz +grt	Palix1	$0.038 \pm 0.002$	$0.051 \pm 0.001$	
Lherz +grt	LS33	$0.031 \pm 0.002$	$0.042 \pm 0.001$	
Lherz +grt	TMO	$0.031 \pm 0.001$	$0.044 \pm 0.001$	This study
Lherz +sp	Pak-1	$0.019 \pm 0.001$	$0.042 \pm 0.001$	
Harz +phlo	LLS-1	-	$0.075 \pm 0.001$	
Calculated for oceanic upper mantle		0.1	0.2	Hirth and Kohlstedt (1996)
Calculated from solubility law, at 1100 °C and 3 GPa			0.54	Bolfan-Casanova (2000)
Quench experiments, with olivine and orthopyroxene embedded in glass		-	$0.08 \pm 0.02$	Koga et al. (2003)

Abbreviations: lherz= lherzolite xenolith, grt=garnet, sp=spinel, harz=harzburgite xenolith, phlo=phlogopite. § xenoliths reference for comparison with Stern et al. (1989, 199).

#### *Application to magma ascent rate*

Diffusion coefficients for each axis can be calculated from the hydroxyl profiles obtained following the procedures established experimentally in section 4.1. Using an estimate of the host basalt temperature it is then possible to calculate ascent duration of the mantle xenoliths. While this is a very simple model for ascent, it may provide interesting insight into the process. The range of temperature in host basalt was estimated to be between 1200-1290°C by D’Orazio et al. (2000, 2001). Thus an average value of 1245°C was assumed. At this temperature and assuming that hydrogen loss is limited by metal vacancies diffusion, the corresponding diffusion coefficients are reported in the Table 4.3.8. In order to solve for time of dehydration, the initial water content must also be known. As it is shown from the water profiles, the olivines are dehydrating. Consequently, the maximum water content given by the profiles cannot be assumed to be the initial water concentration within the olivines in this xenolith. The water content in orthopyroxene is considering to be a good indicator to determine the initial water content in olivine. The water solubility laws for orthopyroxene (Rauch and Keppler, 2002) and olivine (Kohlstedt et al, 1996) can be used to calculate the water partitioning coefficient between olivine and orthopyroxene ; at 2.5 GPa and assuming that the solubility laws are applicable at 1245°C,  $D_{ol/opx}$  is equal to 0.34 (see Bolfan-Casanova for calculation method, 2000). The initial water content in olivine is then deduced using  $D_{ol/opx}$  and the measured water content in orthopyroxene. The water content within the xenolithic orthopyroxene is equal to ~ 310 wt ppm H<sub>2</sub>O (Tables 4.3.5), which yields a water content of ~ 106 wt ppm of H<sub>2</sub>O within olivine. These water contents are based on the calibration of Paterson (1982); using the calibration of Bell et al. (2003), it predicts a water solubility for the olivine of ~313 wt ppm H<sub>2</sub>O. The solubility of water in olivine is the sum of the concentrations calculated with E // [100], [010] and [001]. Thus, the maximum water content for that orientation of E will be less than the solubility, but can be calculated from earlier observations. From spectra of experimentally water-saturated olivine from Bai and Kohlstedt (1998) presented by Bell et al. (2003, Figure 4), it is deduced that ~ 116 wt ppm H<sub>2</sub>O (37% of the total water content ~313 wt ppm H<sub>2</sub>O) would be seen with E parallel to [100], 64 wt ppm H<sub>2</sub>O (20%) parallel to [010] and ~ 135 ppm H<sub>2</sub>O (43%) parallel to [001]. These values were used as initial water content for the calculated diffusion profiles.

**Table 4.3.8** Calculated diffusion coefficients for metal vacancies (assumed to limit hydrogen diffusion at higher temperature) for each crystallographic axis for olivine.

Temperature °C	$D_{[100]} = D_{[010]}$ $\text{m}^2\text{s}^{-1}$	$D_{[001]}$ $\text{m}^2\text{s}^{-1}$
1245	$2.4 \cdot 10^{-12}$	$5.2 \cdot 10^{-11}$

The profiles were calculated using a 3-dimensional equation (Eq. 22) presented in detail in section 3.5. The calculated profiles are shown in Figure 4.3.12. The resulting durations are in a range of few hours. Assuming a depth origin of 70 km and that dehydration occurred continuously and isothermally throughout transport, a time between 2.8 and 5 hours yields an ascent rate from  $\sim 7$  m/s to  $\sim 4$  m/s respectively. These results suggest an extremely rapid ascent toward the surface, which was already expected by the very fresh aspect of the peridotite xenolith. These ascent rates are faster than ascent duration estimations from Selverstone and Stern (1983), who gave ascent rates around 1 m/s for granulite xenoliths from Pali-Aike. They are also faster than results from Spera (1980), who determined ascent rates around 0.5 m/s, based on nodule settling velocities, and the work of Rutherford and Devine (2003), who calculated ascent rate  $>0.02$  m/s based on reaction-rim formation within hornblende. In addition, recent work from Shaw (2004) based on the same principle but using Mg-Fe interdiffusion data in olivine suggest, as in this study, a very rapid ascent of  $\sim 3$  hour for clinopyroxenite inclusions in basanite from the Eifel volcanic field in Germany. Thus, while fast, the reported ascent rates from this study are quite credible.

However, uncertainties on the initial water content and on the temperature used to calculate the diffusion profiles ( $\pm 45$  °C) will have significant consequences on the calculated ascent duration, and therefore on the ascent rate. These need to be improved, by more accurate diffusion laws (*i.e.* deduce from experiments at 1200-1400°C specifically for the [100] direction), solubility laws at high temperature corresponding to host basalt temperature and by the use of more precise

geothermometers, in order to use this promising tool in a rigorous way to obtain accurate ascent rates.

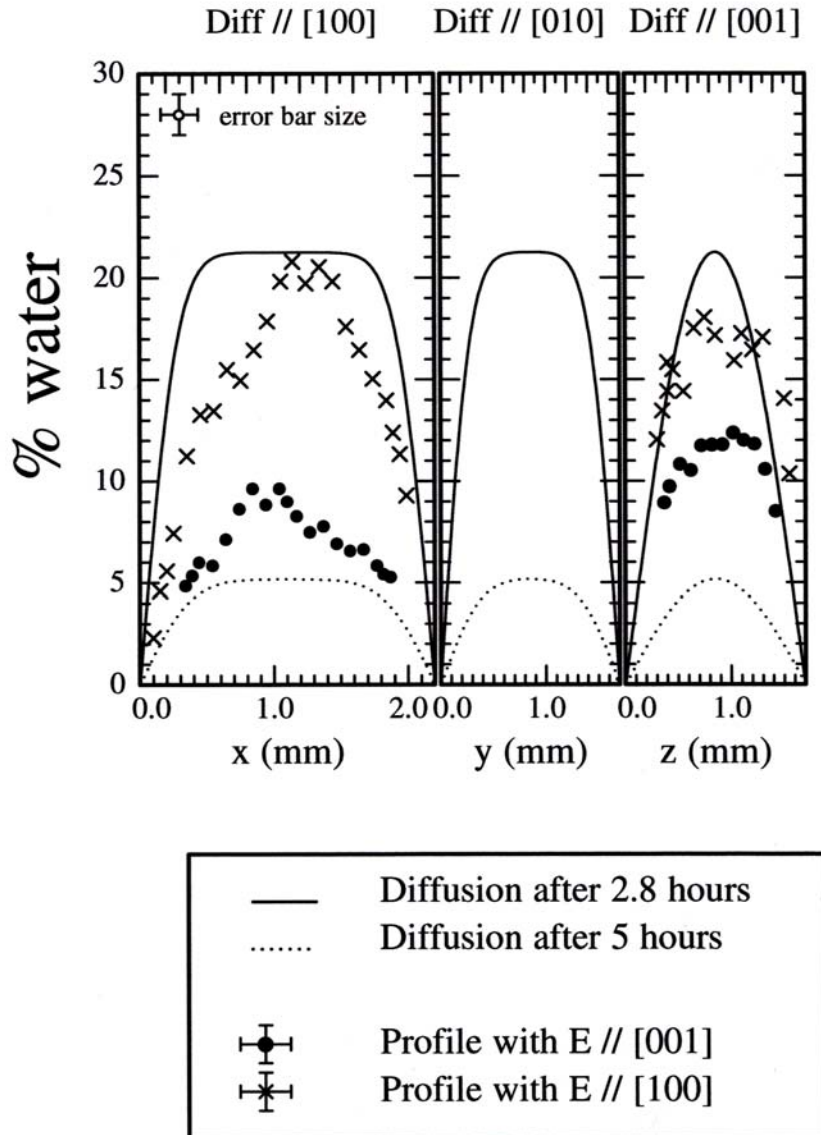


**Figure 4.3.12** Water content normalized to 100 wt ppm H<sub>2</sub>O as a function of position parallel to each axis. Polarized infrared profile across olivine Pa-7 with E parallel to [100] (*crosses*) and E parallel to [001] (*dots*). The *solid lines* represent the calculated diffusion profiles in 3-dimensions (Eq. 22) at 1245°C, after 2.8 hours. The *dotted line* represent the calculated diffusion profiles in 3-dimensions (Eq. 22) at 1245°C, after 5 hours.

### 4.3.6 Conclusion

The results reported in this study provide further insights on the water distribution at the bottom of the lithosphere and on kinetics of hydrogen incorporation within olivine. The following results were obtained:

1. The water distribution in olivine within mantle xenoliths from Pali-Aike is heterogeneous with hydroxyl-depleted rims, indicating that dehydration occurred during ascent from the Earth's uppermost mantle. In contrary Cr-diopside and enstatite show homogeneous water distribution and the garnets are dry.
2. These observations are the first evidence that hydrogen diffusion occurs during magma ascent. Therefore the water content observed in xenolithic olivine from the uppermost mantle is only a partial reflection of the initial water concentration.
3. The water content ratios determined within the NAMs in xenolithic peridotites from Pali-Aike underestimate water-partitioning coefficients between olivine/clinopyroxene and olivine/orthopyroxene. However, these ratios can be used to identify dehydrated xenoliths.
4. The dehydration profile can be used to estimate the ascent duration of the host magma toward the surface, but crucial uncertainties in the initial water content and on the temperature need to be improved in order to use this promising tool in a rigorous way to obtain accurate ascent rates.



## **4.4. Pressure and temperature dependence of water solubility in iron-free wadsleyite**

### **4.4.1 Introduction**

Experimental studies show that wadsleyite can incorporate several weight percent of water, but there is some evidence that the water content of wadsleyite may vary as a function of experimental conditions (Jacobsen, et al., 2004; Kohn et al., 2002; Smyth et al., 1997; Kawamoto et al., 1996; Inoue et al., 1995) and may also depend of the nature of the coexisting phases. In addition, Othani et al. (2000) showed that the water content of ringwoodite, co-existing with hydrous liquid, decreases with increasing temperature.

The pressure and temperature dependence of water solubility in minerals ultimately determines the equilibrium distribution of water in the mantle. Thermodynamic models of water solubility in minerals need to separate out the effects of pressure, temperature and water fugacity on water solubility in order to allow any meaningful prediction of water distribution in the Earth's mantle. For upper mantle minerals, this is relatively straightforward because, in experiments at moderate temperatures and pressures, these minerals coexist with a hydrous fluid containing only little dissolved silicate component. One can therefore reasonably assume that the activity of water in this fluid is close to unity, implying that water fugacity may be calculated with good approximation using the equations of state for pure water. At the pressures and temperatures of the transition zone or lower mantle, however, the situation is very different. The fluid coexisting with minerals such as wadsleyite or ringwoodite will contain abundant dissolved oxides, yielding a phase more appropriately described as "hydrous melt" rather than "aqueous fluid". Water activity in this melt is probably significantly below unity and apparent variations of observed water contents in minerals may reflect changes in water activity due to changes in

#### 4.4. Results: Temperature and pressure-dependence of water solubility in wadsleyite

melt composition rather than any temperature dependence of the dissolution reaction itself. If however, the equilibrium water content in a phase decreases due to a reduced water activity in the coexisting melt, this will not affect the partitioning of water between various minerals. Also, if water solubility decreases with temperature due to a negative enthalpy of the dissolution reaction itself, the effects of temperature on the distribution of water between this phase and other minerals could be dramatic. Accordingly, the aim of this work was to investigate rigorously the separate effects of temperature, pressure, and water activity on the water solubility in iron-free wadsleyite.

For this purpose, a series of multi-anvil experiments were performed at a fixed pressure of 15 GPa and at various temperatures. A second series of experiments was performed with the temperature fixed at 1200°C and pressure varied from 13 to 18 GPa. The starting material in both cases was a mixture of oxides and hydroxide powders yielding  $\text{Mg}_2\text{SiO}_4 + 5 \text{ wt}\% \text{ H}_2\text{O}$ .

Details of the multi-anvil experimental procedures are given in section 2.2.3. The water content was quantified using a ion probe Cameca IMS 1270 (see section 2.5). After polishing of the recovered samples, Raman spectroscopy was used to identify wadsleyite (e.g., Figure 4.4.1). The wadsleyite crystals were carefully examined with optical microscopy to select appropriate grains without cracks, fluid inclusion and milky areas. Afterwards SIMS analyses were performed to quantify water within the wadsleyite. To be rigorous, microprobe analyses were performed after SIMS, on the same wadsleyite crystals at around 30-40  $\mu\text{m}$  from the ion probe crater (sputtering relic).

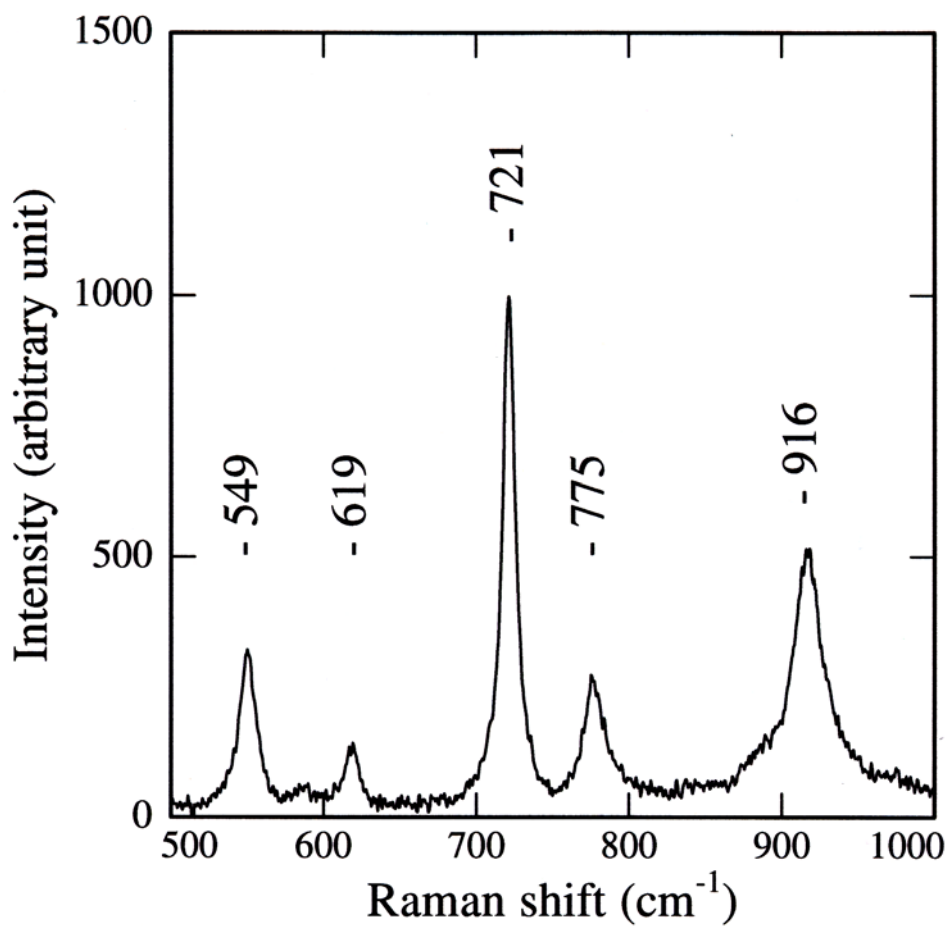


Figure 4.4.1 Raman spectrum of wadsleyite from run H2045.

#### 4.4.2. Results

##### *Run product descriptions and identification*

After each experiment, the capsule was pierced to check for the presence of excess water (indicating water saturation of the system). Experiments where excess water was not observed were discarded. Run products were wadsleyite, clinoenstatite and a quenched crystallized melt. Run conditions and products are compiled in Table 4.4.1.

#### 4.4. Results: Temperature and pressure-dependence of water solubility in wadsleyite

**Table 4.4.1** Experimental conditions, run products,  $^1\text{H}/^{30}\text{Si}$  ratios from SIMS measurements and equivalent average water contents in wadsleyite

Exp. No.	Pressure $\pm 1$ GPa	Temperature $\pm 50$ °C	Run products	$^1\text{H}/^{30}\text{Si}$	$\text{C}_{\text{H}_2\text{O}}^{\text{\$}}$ wt % $\text{H}_2\text{O}$
<i>Constant pressure 15 <math>\pm</math> 1 GPa, increasing temperature</i>					
H2065	15	900	$\beta + qm + \mathcal{F}$	1167	$2.23 \pm 0.37$
H2039	15	1000	$\beta + qm + \mathcal{F}$	1173	$2.13 \pm 0.18$
H2011	15	1100	$\beta + \text{Cen} + qm + \mathcal{F}$	1281	$2.41 \pm 0.12$
H2061	15	1100	$\beta + qm + \mathcal{F}$	1306	$2.42 \pm 0.40$
H2058	15	1200	$\beta + \text{Cen} + qm + \mathcal{F}$	1160	$2.24 \pm 0.06$
H2044	15	1300	$\beta + qm + \mathcal{F}$	910	$1.66 \pm 0.11$
H2045	15	1400	$\beta + \text{Cen} + qm + \mathcal{F}$	533	$0.93 \pm 0.1$
<i>Constant temperature 1200°C, increasing pressure</i>					
H2050	14	1200	$\beta + qm + \mathcal{F}$	1359	$2.40 \pm 0.22$
H2060	14	1200	$\beta + qm + \mathcal{F}$	1577	$2.68 \pm 0.25$
H2059	16	1200	$\beta + qm + \mathcal{F}$	1144	$2.60 \pm 0.22$
H2053	17*	1200	$\beta + qm + \mathcal{F}$	1315	$2.43 \pm 0.33$
H2054	18*	1200	$\beta + qm + \mathcal{F}$	635	$1.24 \pm 0.33$

\* Experiment performed with a 10/5 multi-anvil assembly, \$ average water concentration based on several individual SIMS analyses, except for H2054.  $\beta$  = wadsleyite, *Cen* = clinoenstatite,  $\mathcal{F}$  = observed excess water as fluid at the end of the experiment, *qm* = quenched melt.

Figure 4.4.2 shows electron back-scattered images of typical capsule sections. The central part of the capsule is composed of wadsleyite crystals (dark grey), the rim contains several tiny crystals of clinoenstatite (light grey) and finally the quenched melt is visible between the wadsleyite/clinoenstatite aggregate and the Pt capsule wall. Clinoenstatite was expected to form in each run as in previous studies (Inoue 1994; Inoue et al. 1995; Bolfan-Casanova 2000) but was recognized in only 3 runs. The small volume fraction of clinoenstatite in these experiments could be a reason why clinoenstatite was not observed in every capsule section. Wadsleyite chemical

#### 4.4. Results: Temperature and pressure-dependence of water solubility in wadsleyite

---

compositions are reported in Table 4.4.2. Clinoenstatite and quenched melt analyses are given in Table 4.4.3.

##### *Water solubility*

Table 4.4.1 gives the experimental conditions, the  $^1\text{H}/^{30}\text{Si}$  ratios from SIMS measurements and equivalent average water contents within wadsleyite. Water contents in wadsleyite range from 0.93 wt%  $\text{H}_2\text{O}$  at 1400°C and 15 GPa to 2.68 wt %  $\text{H}_2\text{O}$  at 1200°C and 14 GPa with coexisting hydrous silicate melt and clinoenstatite. The range of water contents is similar to the results of previous SIMS measurements on hydrous wadsleyite (Kawamoto et al., 1996; Inoue et al. 1995). Kawamoto et al. (1996) have reported water contents in iron-bearing wadsleyite between 1.52 wt%  $\text{H}_2\text{O}$  and 3.13 wt %  $\text{H}_2\text{O}$  at 15.5 GPa, and for a temperature range from 1360 to 1600°C. Inoue et al. (1995) have reported water contents in iron-free wadsleyite at 15.5 GPa between 1.1 wt%  $\text{H}_2\text{O}$  and 3.1 wt %  $\text{H}_2\text{O}$ , for a temperature range from 1200 to 1300°C.

##### *Temperature dependence of water solubility*

The effect of temperature on water solubility at a constant pressure of  $15 \pm 1$  GPa is illustrated in Figure 4.4.3. The water content apparently decreases with increasing temperature. The minimum value is around 0.93 wt%  $\text{H}_2\text{O}$  at a temperature of 1400 °C. The water content is relatively constant between 900 to 1200°C with an average value of  $\sim 2.3 \pm 0.3$  wt%  $\text{H}_2\text{O}$ . However, above 1200°C the water content starts to decrease and drops to  $\sim 0.93$  wt%  $\text{H}_2\text{O}$  at 1400°C. The Mg/Si atomic ratio is also relatively stable between 900°C and 1200°C but then increases with increasing temperature. Figure 4.4.3.C shows a relatively good correlation of wadsleyite compositions with the solid line corresponding to the theoretical mechanism of hydroxyl incorporation charged balanced by magnesium vacancies,  $\text{Mg}=2\text{H}$  or  $([V_{\text{Mg}} 2(\text{OH})_O]^x)$  the associated defect in Kröger-Vink (1956) notation. This observation confirms the hypothesis from Smyth (1987) and Inoue (1994).

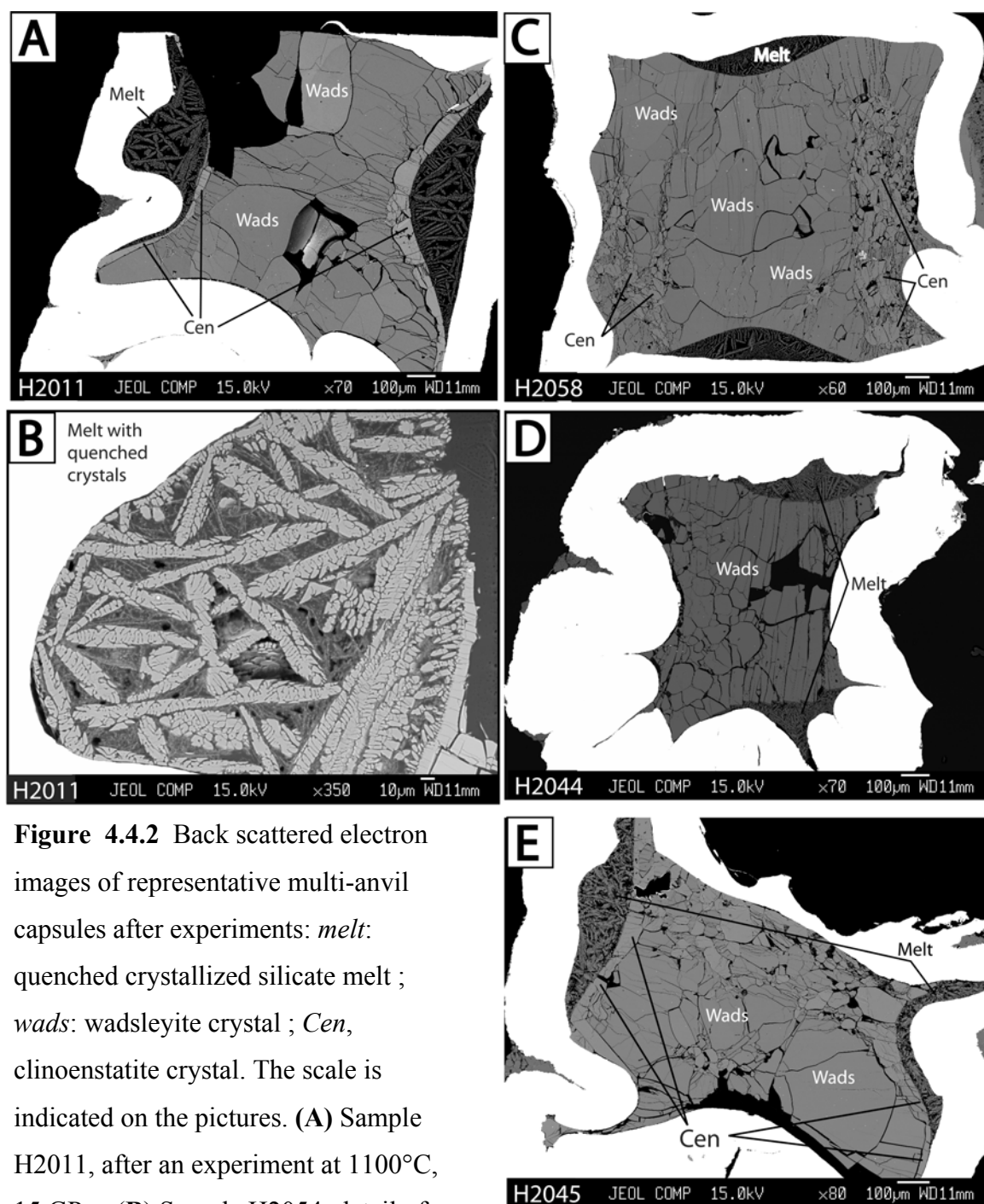


**Figure 4.4.2** Back scattered electron images of representative multi-anvil capsules after experiments: *melt*: quenched crystallized silicate melt ; *wads*: wadsleyite crystal ; *Cen*, clinoenstatite crystal. The scale is indicated on the pictures. **(A)** Sample H2011, after an experiment at 1100°C, 15 GPa ; **(B)** Sample H2054, detail of the quenched crystallized silicate melt.

**(C)** Sample H2058, after an experiment at 1200°C, 15 GPa ; **(D)** Sample H2044, after an experiment at 1300°C, 15 GPa ; and **(E)** Sample H2045, after an experiment ; at 1400°C, 15 GPa.

#### 4.4. Results: Temperature and pressure-dependence of water solubility in wadsleyite

**Table 4.4.2** Representative electron microprobe analyses of iron-free wadsleyite

Element (wt.%)	H2011	H2039	H2044	H2045	H2050	H2053
	<i>wadsleyite</i>	<i>wadsleyite</i>	<i>wadsleyite</i>	<i>wadsleyite</i>	<i>wadsleyite</i>	<i>wadsleyite</i>
Mg	31.98 (0.15)	31.56 (0.16)	33.57 (0.04)	33.17 (0.19)	31.64(0.25)	32.08 (0.04)
Si	20.18 (0.17)	20.16 (0.1)	20.14 (0.08)	20.17 (0.09)	20.14(0.11)	20.36 (0.05)
Fe	< DL	0.13 (0.08)	0.03 (0.01)	0.34 (0.13)	0.004(0.02)	0.01 (0.01)
Pt	< DL	< DL	< DL	0.01 (0.01)	0.05(0.02)	< DL
Al	0.10 (0.08)	0.14 (0.13)	0.12 (0.01)	0.11 (0.01)	0.12(0.02)	0.08 (0.01)
O	44.17 (0.12)	43.81 (0.05)	45.05 (0.07)	44.92 (0.13)	43.09(0.3)	44.39 (0.07)
Sum	96.36 (0.51)	95.59 (0.39)	99.08 (0.29)	98.72 (0.49)	95.89 (0.72)	96.93 (0.3)
SiO <sub>2</sub>	43.52 (0.37)	43.14 (0.18)	43.09 (0.18)	43.15 (0.2)	43.03(0.24)	43.55 (0.1)
Mg/Si*	1.83 (0.02)	1.80 (0.02)	1.91 (0.02)	1.90 (0.02)	1.80 (0.02)	1.82(0.02)

Element (wt.%)	H2054	H2058	H2059	H2060	H2061	H2065
	<i>wadsleyite</i>	<i>wadsleyite</i>	<i>wadsleyite</i>	<i>wadsleyite</i>	<i>wadsleyite</i>	<i>wadsleyite</i>
Mg	31.43 (0.23)	32.61 (0.03)	32.25 (0.1)	31.67 (0.15)	31.51 (0.13)	32.25 (0.37)
Si	20.33 (0.04)	20.03 (0.18)	20.21 (0.13)	20.27 (0.06)	19.90 (0.18)	20.07 (0.16)
Fe	0.02 (0.01)	< DL	0.03 (0.02)	0.02 (0.01)	0.05 (0.01)	0.03 (0.01)
Pt	< DL	< DL	0.03 (0.03)	0.01 (0.01)	< DL	< DL
Al	0.16 (0.02)	0.07 (0.02)	0.09 (0.01)	0.08 (0.01)	0.14 (0.02)	0.15 (0.02)
O	44.01 (0.16)	44.35 (0.19)	44.36 (0.10)	44.02 (0.09)	43.55 (0.27)	44.25 (0.25)
Sum	95.96 (0.41)	97.06 (0.44)	96.99 (0.40)	96.07 (0.32)	95.15 (0.6)	96.75 (0.5)
SiO <sub>2</sub>	42.94 (0.08)	42.84 (0.39)	43.39 (0.28)	43.39 (0.12)	42.57 (0.39)	42.94 (0.35)
Mg/Si*	1.79(0.02)	1.88 (0.02)	1.84 (0.01)	1.81 (0.01)	1.83 (0.02)	1.86 (0.02)

\* atomic ratio, <DL = below detection limit.

#### 4.4. Results: Temperature and pressure-dependence of water solubility in wadsleyite

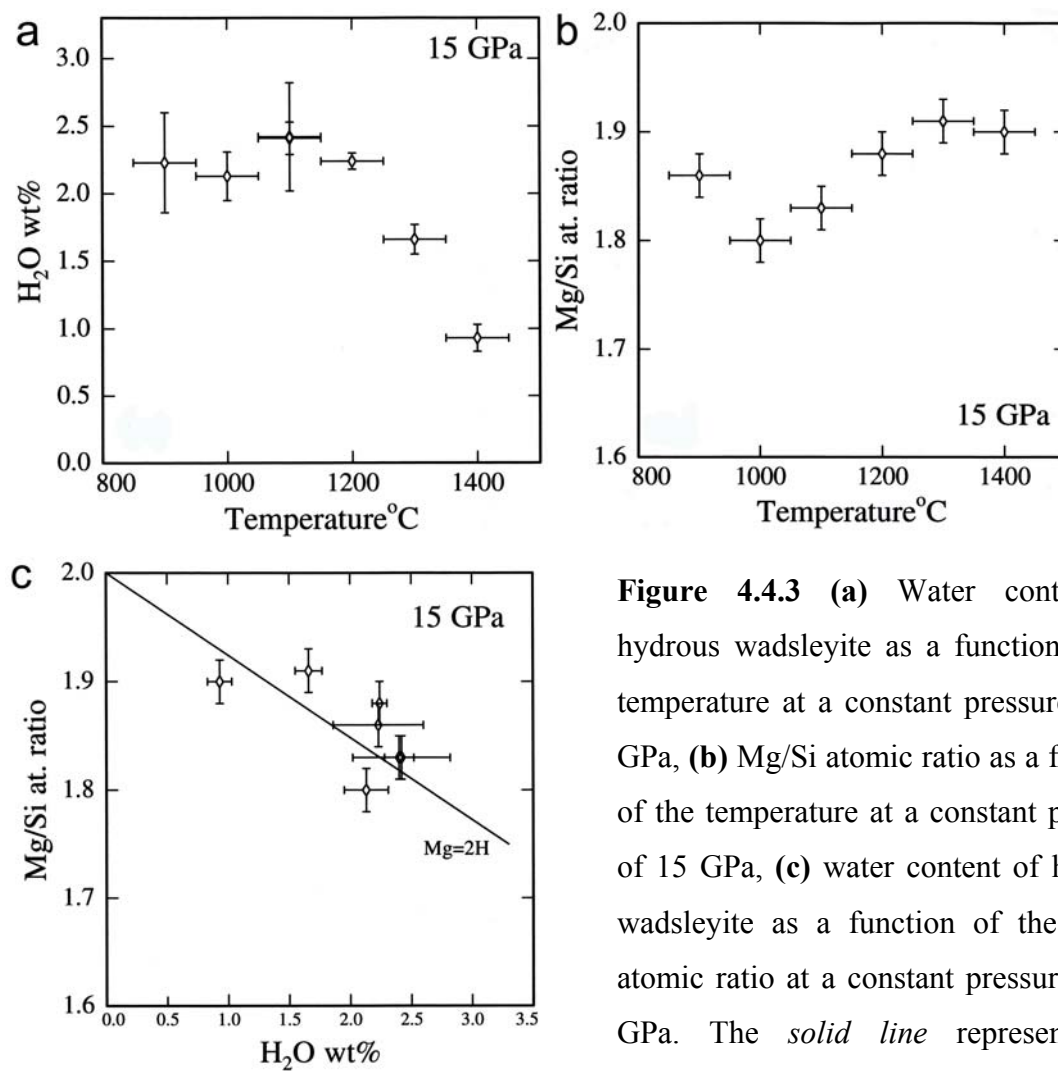
**Table 4.4.3** Representative electron microprobe analyses of clinoenstatite and silicate melt co-existing with hydrous wadsleyite.

Element	H2011	H2058	H2045	
(wt.%)	<i>Clinoenstatite</i>	<i>Clinoenstatite</i>	<i>Clinoenstatite</i>	
Mg	23.99(0.75)	24.39(0.25)	24.31(0.09)	
Si	27.12(0.64)	27.39(0.09)	27.72(0.08)	
Fe	0.01(0.02)	0.02(0.02)	0.02(0.01)	
Pt	0.09(0.12)	0.22(0.15)	0.12(0.13)	
Al	0.04(0.01)	0.12(0.01)	0.04(0.01)	
O	46.73(1.21)	47.40(0.24)	47.61(0.1)	
Sum	97.98(2.49)	99.57(0.44)	99.80(0.31)	
SiO <sub>2</sub>	58.02(1.36)	58.59(0.53)	59.29(0.17)	
Mg/Si*	1.02(0.04)	1.03(0.01)	1.013 (0.005)	
Element	H2011	H2058	H2044	H2045
(wt.%)	<i>melt</i>	<i>melt</i>	<i>melt</i>	<i>melt</i>
Mg	27.96 (2.21)	26.11 (4.97)	30.59 (4.38)	30.35 (1.73)
Si	16.39 (2.09)	11.86 (3.51)	13.64 (2.37)	18.29 (2.53)
Fe	0.04 (0.02)	0.02 (0.02)	0.02 (0.02)	0.03 (0.03)
Pt	0.25(0.21)	0.27(0.37)	0.24(0.21)	0.46(0.29)
Al	0.32 (0.05)	0.45 (0.12)	0.35 (0.16)	0.28 (0.03)
O	37.39 (3.81)	31.13 (7.29)	36.01 (5.16)	41.1 (3.99)
Sum	82.35 (7.89)	69.84 (15.6)	80.86 (11.3)	90.51 (8.07)
SiO <sub>2</sub>	35.05 (4.46)	25.38 (7.5)	29.18 (5.07)	39.12(5.42)
Mg/Si*	1.97(0.3)	2.54 (0.9)	2.59 (0.58)	1.92 (0.3)

\* atomic ratio.

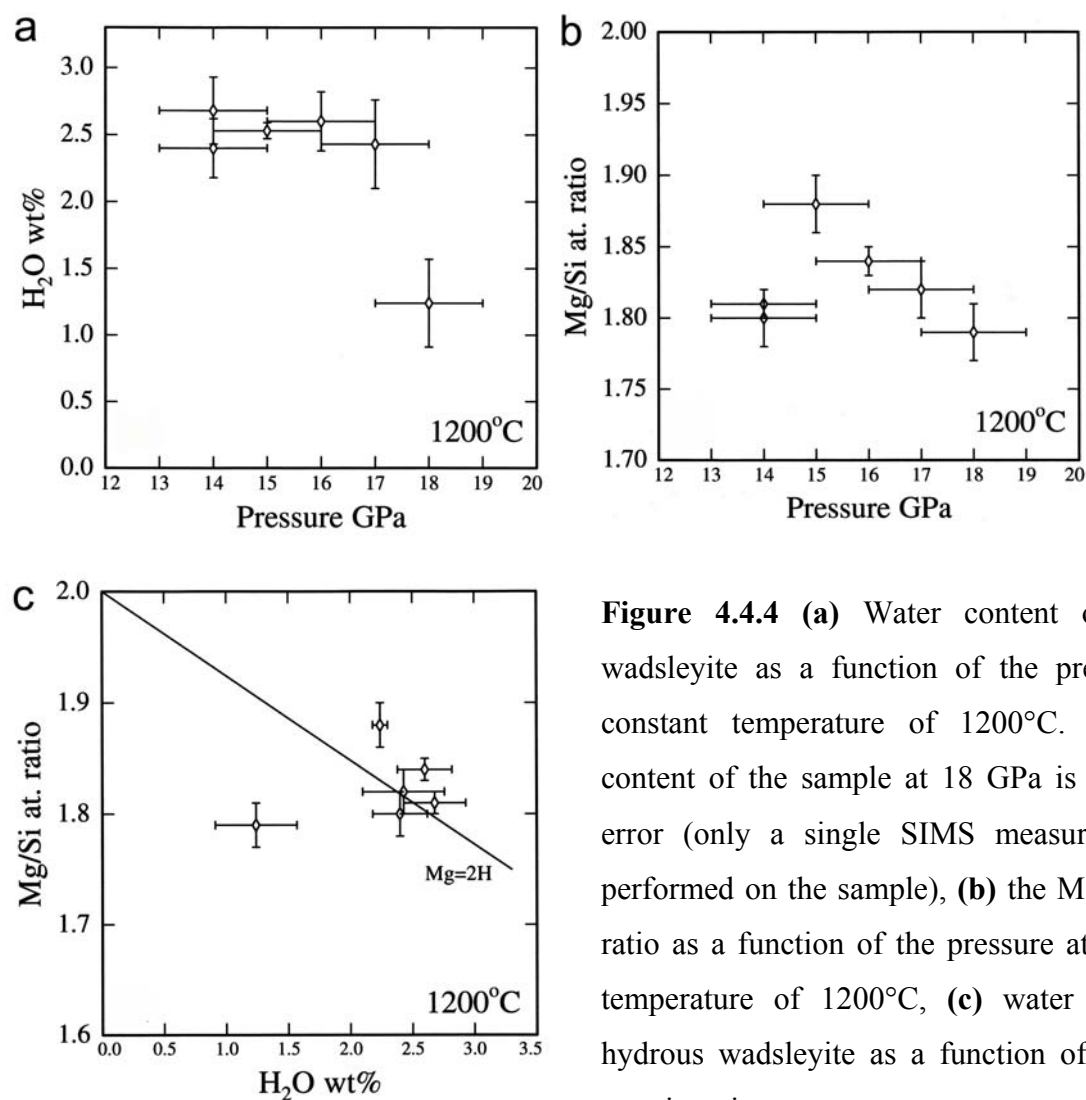
*Pressure dependence of water solubility*

Figure 4.4.4 shows that there is no significant effect of pressure on the water content or the Mg/Si ratio of wadsleyite, with the exception of one data point at  $18 \pm 1$  GPa. This experiment is anomalous in its water content was derived from a single SIMS measurement. This data point is possible in error and therefore considered to be unreliable.



**Figure 4.4.3** (a) Water content of hydrous wadsleyite as a function of the temperature at a constant pressure of 15 GPa, (b) Mg/Si atomic ratio as a function of the temperature at a constant pressure of 15 GPa, (c) water content of hydrous wadsleyite as a function of the Mg/Si atomic ratio at a constant pressure of 15 GPa. The *solid line* represents the theoretical substitution mechanism  $\text{Mg} = 2\text{H}$ .

#### 4.4. Results: Temperature and pressure-dependence of water solubility in wadsleyite



**Figure 4.4.4** (a) Water content of hydrous wadsleyite as a function of the pressure at a constant temperature of 1200°C. The water content of the sample at 18 GPa is possibly in error (only a single SIMS measurement was performed on the sample), (b) the Mg/Si atomic ratio as a function of the pressure at a constant temperature of 1200°C, (c) water content of hydrous wadsleyite as a function of the Mg/Si atomic ratio at a constant temperature of 1200°C. The *solid line* represents the theoretical substitution mechanism  $Mg = 2H$ .

#### 4.4.3. Discussion

##### *Thermodynamics of water distribution between wadsleyite and melt in the system MgO-SiO<sub>2</sub>-H<sub>2</sub>O*

During the experiments carried out in this study wadsleyite coexisted with clinoenstatite and a hydrous melt. Although clinoenstatite was not detected in all run products, this is probably only due to its low abundance; the presence of some small amount of clinoenstatite in all runs can be reasonably assumed. This means that in the three-component system MgO-SiO<sub>2</sub>-H<sub>2</sub>O three phases coexisted and according to the

#### 4.4. Results: Temperature and pressure-dependence of water solubility in wadsleyite

phase rule, there are two degrees of freedom for this phase assemblage. Since pressure and temperature were fixed during the experiments, there is no additional degree of freedom left, implying that the compositions of all phases in equilibrium are fixed and are only functions of pressure and temperature. Thus the water contents analyzed in various run products do not depend on the absolute percentage of water loaded into the capsule. Rather any experimentalist doing experiments in the same system should observe (within experimental error) the same phase compositions at the same P and T, as long as all three phases wadsleyite, clinoenstatite and melt are present. As long as these phases coexist, the phase rule implies that changes in bulk composition can only change the proportions of the phases, but not their compositions. An increase in bulk water content in the capsule, for example, would only increase melt fraction, without changing the melt composition or the water content in wadsleyite.

In order to fully characterize the coexisting phases, the mass fractions of wadsleyite, clinoenstatite and melt were calculated using the mass balance for MgO and SiO<sub>2</sub>. These mass fractions were then used to estimate the water content in the melt by mass balancing the total water content of the starting composition and assuming that no water was lost during the experiment. Results of the mass balance calculations are reported in Table 4.4.4. The calculated melt compositions yield a Mg/Si ratio between 1.92 and 2.59. The water content decreases with increasing temperature from ~31.5 wt% H<sub>2</sub>O at 1100°C to ~12.0 wt% H<sub>2</sub>O at 1400°C. In contrast to this, the melt fraction increases with increasing temperature from 7.5 % to 37 % by weight.

**Table 4.4.4** Mass balance calculations, water partition coefficients and apparent equilibrium constant.

Sample-Temp °C	MgO wt%	SiO <sub>2</sub> wt%	H <sub>2</sub> O wt%	Mg/Si ratio	Fraction %	$D_{\text{wadsleyite/melt}}^{\text{water}}$	K*
H2011 1100°C						0.076(0.017)	0.056(0.014)
wadsleyite	53.0 (0.4)	43.2 (0.3)	2.41(0.12)	1.83	84		
melt <sup>#</sup>	39.08	29.38	31.52(7)	1.98	7.5		
clinoenstatite	39.77(1.24)	58.02(1.36)	0.05(0.02)	1.02	8.5		
H2058 1200°C						0.078(0.04)	0.063(0.021)
wadsleyite	53.92(0.62)	42.75(0.52)	2.24(0.06)	1.88	74		
melt <sup>#</sup>	43.33	25.34	28.62(16)	2.54	12		
clinoenstatite	40.50(0.15)	58.59(0.53)	0.05(0.02)	1.03	14		
H2044 1300°C						0.083(0.037)	0.076(0.015)
wadsleyite	54.81(0.22)	42.67(0.04)	1.66(0.44)	1.91	71		
melt <sup>#</sup>	50.74	29.16	20.1(6)	2.59	17.5		
clinoenstatite*	40	60	0.05(0.02)	1	7.5		
H2045 1400°C						0.078(0.018)	0.070(0.013)
wadsleyite	55.09(0.11)	43.12(0.15)	0.93(0.1)	1.90	50		
melt <sup>#</sup>	49.57	38.43	12.0(2.5)	1.92	37		
clinoenstatite	40.31(0.14)	59.29(0.17)	0.05(0.02)	1.01	12		

Composition of wadsleyite and clinoenstatite correspond strictly to electron microprobe analyses except for \*, which is a theoretical composition. Melt composition (#) was allowed to vary within error to yield a better mass balance on SiO<sub>2</sub>, MgO and H<sub>2</sub>O. K\* is the apparent equilibrium constant for the exchange equilibrium between wadsleyite and melt. See text for details. Water content in clinoenstatite estimated from Rauch and Keppler (2002).

#### 4.4. Results: Temperature and pressure-dependence of water solubility in wadsleyite

The Nernst partition coefficient of water between wadsleyite and melt is close to 0.08 and appears to be virtually independent of temperature.

Assuming that the dominant substitution mechanism for water incorporation in wadsleyite is the replacement of one magnesium by two hydrogens, the exchange equilibrium between wadsleyite and melt can be described by the equation



with the equilibrium constant

$$K = (a_{\text{MgO,melt}} a_{\text{H}_2\text{O,wadsleyite}}) / (a_{\text{MgO,wadsleyite}} a_{\text{H}_2\text{O,melt}}) \quad \text{Eq. 25}$$

where  $a$  denotes the activity of MgO or water in melt or wadsleyite, respectively.  $K$  is related to the standard state Gibbs free enthalpy of the exchange equilibrium according to

$$\ln K = - \Delta G^\circ / RT = \Delta S^\circ / R - \Delta H^\circ / RT \quad \text{Eq. 26}$$

with  $\Delta G^\circ$  being the Gibbs free enthalpy,  $\Delta S^\circ$  the entropy and  $\Delta H^\circ$  the enthalpy of the reaction and  $R$  being the gas constant. If one assumes the activity coefficients of MgO and H<sub>2</sub>O in wadsleyite and melt to be constant over the concentration range studied, a plot of the apparent equilibrium constant  $K^*$ , (where  $X_{i,j}$  is the molar fraction of the component  $i$  in the phase  $j$ ),

$$K^* = (X_{\text{MgO,melt}} X_{\text{H}_2\text{O,wadsleyite}}) / (X_{\text{MgO,wadsleyite}} X_{\text{H}_2\text{O,melt}}) \quad \text{Eq. 27}$$

versus  $1/T$  yields the enthalpy of the reaction. This plot is shown in Figure 4.4.5 and yields a very low reaction enthalpy of  $\Delta H = - 16.8 \pm 7.1$  kJ/mol. Values for  $K^*$  are given in Table 4.4.4. The negligible pressure effect on the water content of wadsleyite coexisting with melt suggests that the volume change associated with the exchange reaction is also negligible.

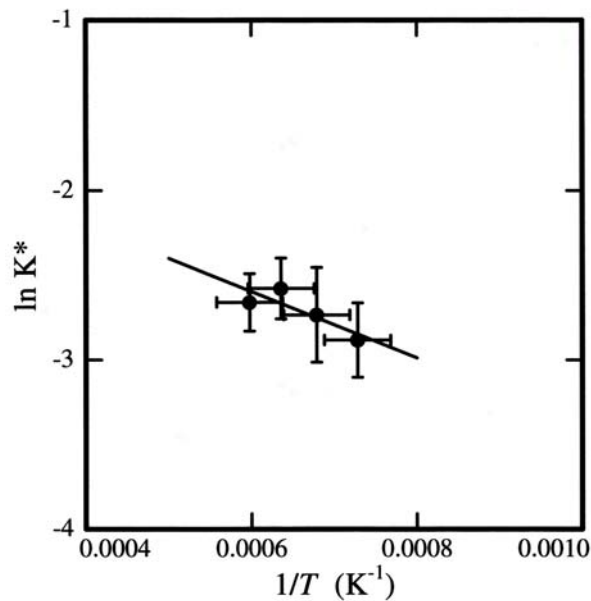


**Figure 4.4.5** The apparent equilibrium constant,  $K^*$ , as a function of  $1/T$  with the temperature in Kelvin.

#### *Comparison with previous work*

The partition coefficients of water between wadsleyite and melt obtained in this study are very close to the value of  $0.1 \pm 0.04$  reported by Kawamoto et al. (1996) for a KLB-1 peridotite system. However, Kawamoto et al. (1996) cautioned that their data should only be considered as lower limits of the actual partition coefficients because of uncertainties in their mass balance calculation. Indeed, in their study, the calculated water content in the silicate melt at 15.5 GPa decreases first from 38 % at 1360 °C to 11 % at 1450 °C but then increases to 26 % at 1500 °C, which is difficult to understand. Nevertheless, if the data from Kawamoto et al. (1996) are compared to those of the present study, it appears that the composition of the silicate melt has little effect on the partition coefficient of water between wadsleyite and melt, which is an important observation.

Figure 4.4.6 compares water contents in wadsleyite in equilibrium with hydrous melts from this study with results from Inoue et al. (1995) and Kawamoto et al. (1996). All three data sets overlap, but the data by the other two studies show much more variation in water contents over a narrow interval of temperature. Moreover, it is obvious that the data from this study fall close to the lower limit of the range of data

#### 4.4. Results: Temperature and pressure-dependence of water solubility in wadsleyite

from the two previous studies. The data by Inoue et al. (1995) were obtained in the MgO-SiO<sub>2</sub>-H<sub>2</sub>O system, where an effect of bulk composition can be ruled out. The difference between the new data and those of Kawamoto et al. (1996) could be due to bulk compositional effects, because the presence of additional components in the system may affect the activity coefficients of MgO and H<sub>2</sub>O in the silicate melt and could therefore change the amount of water incorporated in wadsleyite. However, such an effect would be difficult to reconcile with the observation that Kawamoto et al. (1996) measured partition coefficients of water very close to those determined in this study. It is therefore possible that those data points by Inoue et al. (1995) and Kawamoto et al. (1996), which suggest much higher water contents in wadsleyite than found in the present study under similar conditions, may have been affected by the presence of melt inclusions or other hydrous impurities in the crystals analysed by ion probe.

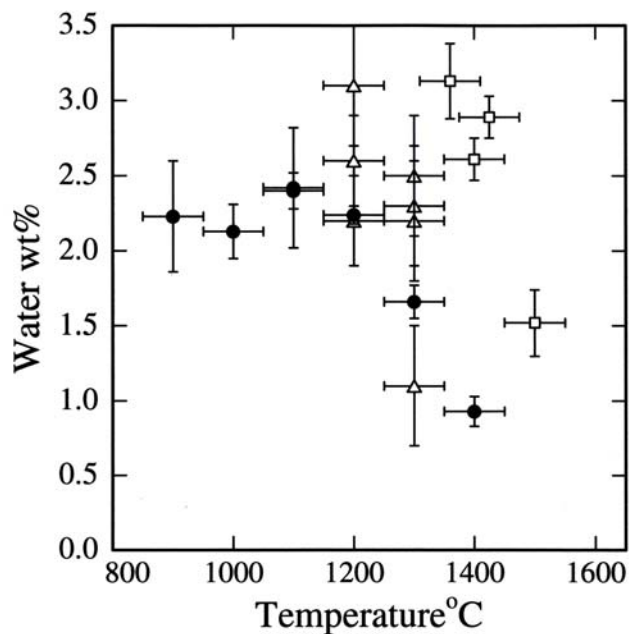


**Figure 4.4.6** Water content in wadsleyite as a function of temperature according to the present study and previous work. The *filled dots* are the results from this study, the *open triangles* are for iron-free wadsleyite from Inoue et al. (1995); and the *open squares* are for iron-bearing wadsleyite from Kawamoto et al. (1996).

##### *Implications for water storage in the transition zone*

If the water solubility in wadsleyite under realistic transition zone conditions is up to three lower than previously suggested, the maximum amount of water that could be stored in the upper part of the transition zone is obviously much lower than the four ocean masses originally suggested by Smyth (1994). However, from all available geophysical and geochemical evidence (e.g. Wood 1995, Bolfan-Casanova et al. 2000), it is clear that the present day transition zone is far from water saturation and was, most likely, never saturated with water in the history of the Earth. For this reason, it is much more important to exploit the consequences of the water solubility data in wadsleyite for the partitioning of water between mantle phases. Ohtani et al. (2000) estimated partition coefficients of water between ringwoodite and a coexisting fluid or silicate melt. In contrast to all studies on wadsleyite, they observe a strong temperature dependence of  $D_{\text{ringwoodite/melt}}^{\text{water}}$ , with an increase from 0.021-0.024 at 1300°C up to 0.04-0.044 at 1450°C. From these data, the water partitioning coefficient between wadsleyite and ringwoodite can be estimated according to  $D_{\text{wadsleyite/ringwoodite}}^{\text{water}} = D_{\text{wadsleyite/melt}}^{\text{water}} / D_{\text{ringwoodite/melt}}^{\text{water}}$ . This calculation suggests that  $D_{\text{wadsleyite/ringwoodite}}^{\text{water}}$  decreases from a value close to 4 at 1300 °C to a value close to 2 at 1450 °C. If it was possible to extrapolate these limited data, they would imply that around 1600 °C, water does not fractionate anymore between wadsleyite and ringwoodite and, at even higher temperatures, water preferentially enters ringwoodite.

Given the above prediction of the temperature dependence of water partitioning between ringwoodite and wadsleyite holds, there are two important consequences: (i) While a strong fractionation of water between ringwoodite and wadsleyite will tend to smear out the wadsleyite-ringwoodite transition over a significant interval of pressure, the transition will become sharper at temperatures where the fractionation vanishes. It is therefore possible that the presence or absence of a detectable 520 km seismic discontinuity is related to the effect of temperature on the fractionation of water between ringwoodite and wadsleyite. (ii) During the formation of the transition zone in the Hadean (i.e., before Archean), most of the water would have entered ringwoodite. During subsequent cooling, more and more

water would partition from the ringwoodite phase of the lower transition zone into the wadsleyite phase of the upper transition zone. This continuous replenishment of the water reservoir in the upper transition zone could be very important for sustaining the formation of hydrous komatiite melts over a long periods of Earth history (Kawamoto et al. 1996). However, this assumes that these reservoirs are not homogenized by mantle convection. This may be possible if hydrogen diffusion along grain boundaries significantly exceeds expected convection rates (Richard et al. 2002).

#### 4.4.4. Conclusion

These series of experiments at water saturated conditions in the system MgO-SiO<sub>2</sub>-H<sub>2</sub>O suggest the following:

1. The water solubility in iron-free wadsleyite is relatively stable from 900°C up to 1200°C, with an average water content around  $2.3 \pm 0.3$  wt%. Above 1200°C, the water content decreases, falling to  $0.93 \pm 0.1$  wt% at 1400°C. Furthermore the partition coefficient of water between wadsleyite and coexisting silicate melt is nearly independent of temperature with,

$$D_{\text{wadsleyite/melt}}^{\text{water}} \approx 0.08$$

2. Mg/Si ratios are correlated to the water content, and increase as a function of increasing temperature. These observations confirm that hydrogen absorption is mostly controlled at high temperature by the substitution mechanism of two hydrogens for one magnesium (the associated defect,  $[V_{\text{Mg}} 2(\text{OH})_o]^x$ ).
3. From 14 GPa and to 18 GPa, water content does not show clear pressure dependence.
4. The results suggest that the water storage capacity of wadsleyite in the transition zone is much lower than previously suggested.
5. The data imply a strong decrease of the water partition coefficient,  $D_{\text{wadsleyite/ringwoodite}}^{\text{water}}$ , between wadsleyite and ringwoodite with temperature.

#### 4.4. Results: Temperature and pressure-dependence of water solubility in wadsleyite

## 4.5. Computer simulation of hydrous defects in iron-free wadsleyite

### 4.5.1. Introduction

Complementing the experiments on hydrous wadsleyite, hydrous defects in the structure of wadsleyite were simulated by computer calculations. The program GULP (General Utility Lattice Program), which is based on a semi-empirical model, was used to simulate the formation of various point defects in wadsleyite. Particular attention was paid to hydrogen incorporation linked to vacancies and their corresponding infrared frequencies. The computer calculations were performed at the Royal Institution (Davy Faraday Research Laboratory), in London, during July 2003 under the direction of Dr. Kate Wright and Andrew Walker, with the authorization of Prof. Dr. R. Catlow. A brief review of the different computer simulation techniques and the main methodological points are given below.

### 4.5.2. Modelling solids and simulation of defects

The computer modelling methods for solids can be separated into two main groups:

- (1) The interatomic potential method, which is a semi-empirical approach based on the description of interaction energies between atoms as a function of their distances and structures,
- (2) The *ab-initio* method, which is based on solving the Schrödinger equation to obtain the energy of the mineral at a given pressure and temperature. The Hartree-Fock (and post Hartree-Fock) method and the density functional theory (DFT) are the most used *ab-initio* methods.

At present time the interatomic potential and DFT methods are used for modelling solids and possible associated point defects. The main difference between them is that a DFT calculation is extremely time-consuming compared to a potential-based calculation. To give a time-scale, for a system of the same size, a DFT calculation requires around 10 to 100 times more time than a potential-based calculation.

The aim of my short scientific visit to the Royal Institution was to become familiar with the computer modelling and to produce data for point defects in wadsleyite. Calculations using the GULP code, based on the interatomic potentials method, were chosen because of the limited time available.

Figure 4.5.1 presents a simple diagram showing the different methods for modelling solids with examples of well-known programs available on the market, and possible approaches for defect simulation. The following sections provide a short description of the GULP and important methodological points.

##### *The General Utility Lattice Program (GULP)*

The GULP is able to calculate various physical and chemical properties of a 3-dimensional lattice (Gale, 1997; Gale and Rohl, 2003), for example, lattice parameter at given pressure, elastic constants, bulk moduli, piezoelectric constants, phonon frequencies, heat capacities, entropies at constant volume, Helmholtz and Gibbs free energies, and defect energies. A complete list is available in Gale (1997) and also in the user manual (<http://www.ch.ic.ac.uk/gale/Research/gulp.html>).

As mentioned above, GULP is a semi-empirical method and uses force fields based on the Born model of atoms. The force fields include pseudo-interatomic potentials for two- and three-body interactions:

- Two-body interaction: using first, the Buckingham potentials, which describe the short-range potential (repulsion-attraction) and second, the Morse potentials, which describe the O-H covalent bond,
- The three-body interactions, which represent here the repulsion between two bonds.

The functional forms of these potentials are given in detail in Gale and Rohl (2003) (Table I, page 297). See Catlow and Mackrodt (1982) for details of the potentials and for quantitative values of the potentials.

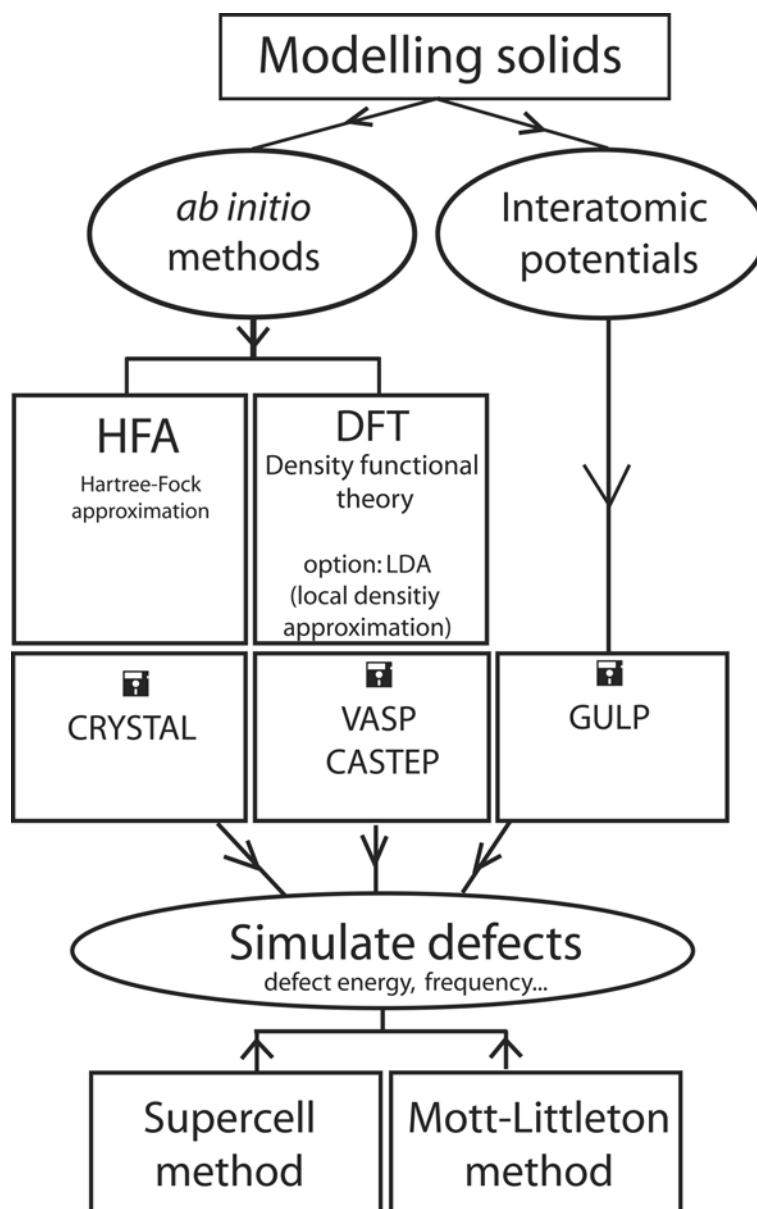


**Figure 4.5.1** Possible methods for computer modelling of solids and defects. (abbreviation: VASP: Vienna *Ab-initio* Simulation Package and GULP: General Utility Lattice Program).

*Shell model*

In addition to these potentials, GULP also includes the shell model (Dick and Overhauser 1958) for the polarization of anions. This classical model (Figure 4.5.2) presents ions as systems divided into a shell (electronic cloud with a charge Y) and a core (charge X) both linked by a harmonic spring with force constant, k. The polarity of the system is then given by:

$$\alpha_i = \sum_i \frac{(Y_i e)^2}{k_i^S} \quad \text{Eq. 28}$$

Where,  $k_i$  is the force constant,  $Y_i$  the charge of the shell.

As above, complementary functional forms are given in detail in Gale and Rohl (2003) and Vocádko (1993).

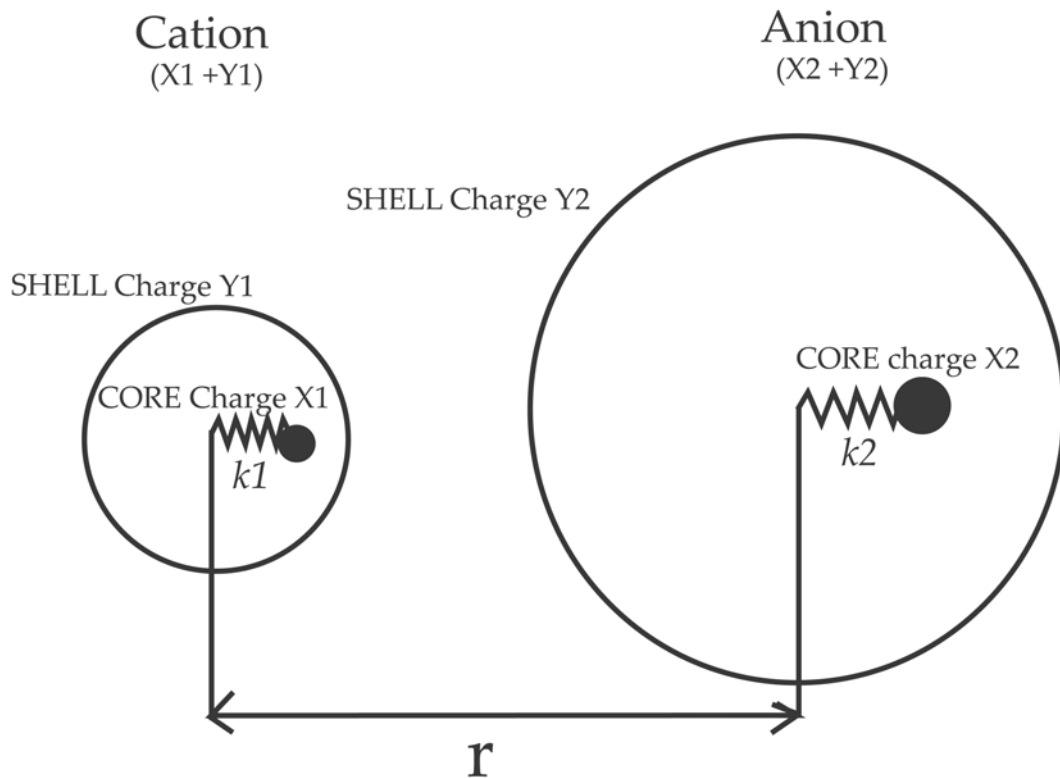


**Figure 4.5.2** Ionic interactions in the shell model, where k is the spring constant, r is the core-shell distance; x, the core charge, and y, the shell charge (redrawn from Vocádko, 1993).

To simulate defects inside a calculated structure, two methods are currently used: the Supercell method and the Mott-Littleton method. GULP can simulate defects using both functions. The Mott-Littleton method was chosen because it is particularly suitable to simulate energies of isolated defects in a perfect crystal. The Supercell approach is more dedicated to the use of the plane-wave code and the temperature-pressure effects on many cells. However both the Supercell and Mott-Littleton methods can be used for simulation of vibrational energies.

*Mott-Littleton method*

The Mott-Littleton method (1938) considers that the defect is embedded in an infinite dielectric continuum, with atoms close to the defect considered explicitly. The defective crystal is therefore described using 3 spheres (Figure 4.5.3). The first one, close to the defect is called region I where the energies are calculated for a relaxed and modified lattice. The sphere far way from the defect and extending to infinity is called region II. Finally, the intermediate sphere is called IIa, which links region II and I. The total interactions energy between region I and II is given by:

$$U_{tot}(x, \xi) = U_{I,I}(x) + U_{I,II}(x, \xi) + U_{II,II}(\xi) \quad \text{Eq. 29}$$

where  $U_{I,I}(x)$ , represents the energy of all atoms in region I as a function of the Cartesian coordinates  $x$ ,  $U_{II,II}(\xi)$  represent the energy of region II as a function of the Cartesian displacement  $\xi$  of all atoms in region I. The atomic displacements into region II are considered as negligible, so that  $U_{II,II}(\xi)$  does not need to be calculated.  $U_{I,II}(x, \xi)$  represents the energy of interaction between the two regions.

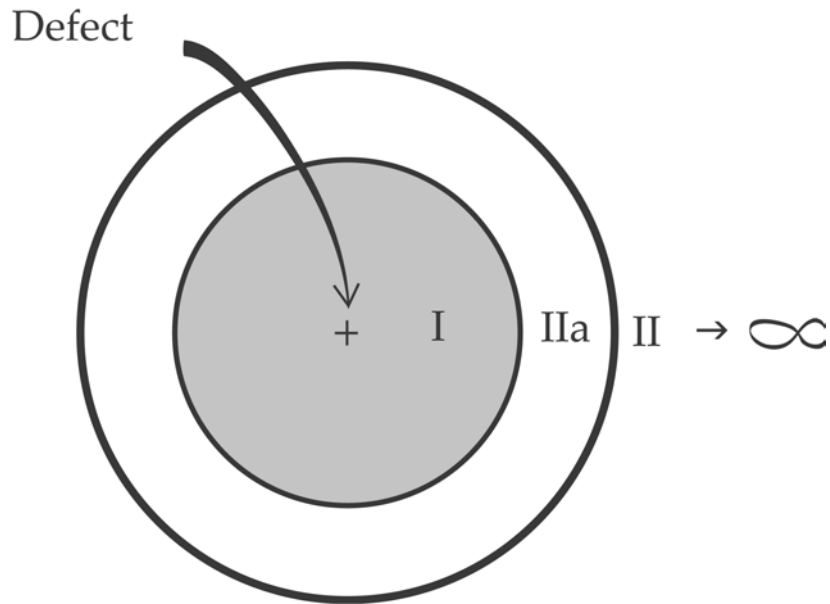


**Figure 4.5.3** The Mott-Littleton embedded defect model

The calculations are performed at constant volume and at zero Kelvin. Corrections could be made for a lattice stable at high-temperature by recalculating the energy for a volume corresponding to the new temperature. The Mott-Littleton method gives results in general agreement with experimental data and with defect energies calculated with DFT or using a Supercell method (*e.g.*, using the PARAPOCS program, Richmond, 1999).

One of the first steps during the calculation is to “calibrate” the Mott-Littleton sphere radius (region I and IIa) to attain a minimum energy for a given sphere size and a given defect (*i.e.*, magnesium vacancy, oxygen vacancy or silicon vacancy). For that we calculate the energies for different radii of region I only (the diameter of region IIa is assumed to be twice the diameter of region I). Figure 4.5.4 shows that a common minimum energy is achieved with a radius of 12 Å for region I, and therefore 24 Å for region IIa for the three main types of defects studied in iron-free wadsleyite. A region I with a radius of 12 Å is composed of around 1200 atoms and region IIa with a radius of 24 Å spans 8,000 atoms.

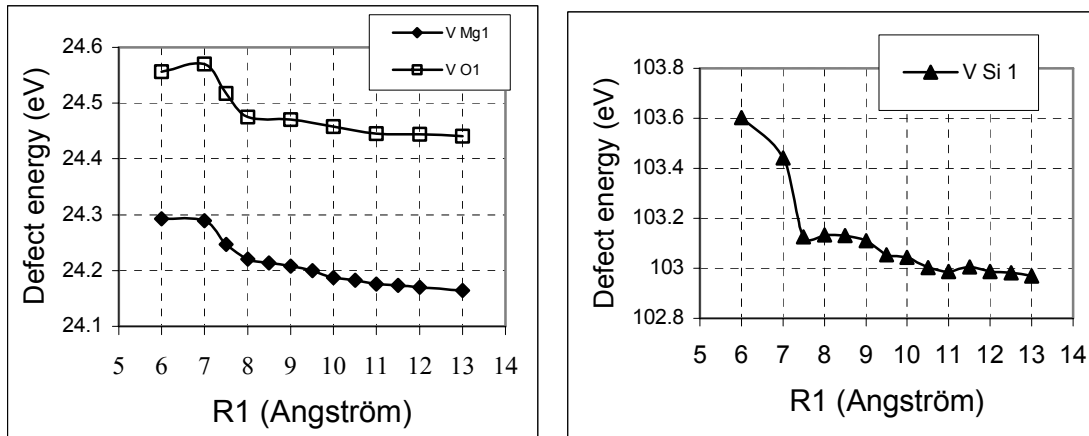


**Figure 4.5.4** “Radius calibration” of the region I in the Mott-Littleton defect embedded model. A radius of 12 Å gives a satisfying energy minimization for the three kinds of vacancy investigated.

#### *Practice procedure*

GULP is running on a PC-cluster, which is linked to a UNIX station, where the *input files* are prepared and where the *output files* are collected, both using an editor, (*e.g.*, Vi).

An input file contains:

- The key words, especially the algorithms used for energy minimization: BFGS (Brogden-Fletcher-Goldfarb-Shannon method) or/and RFO (rational function optimizer)
- The lattice parameters of the starting structure, (*i.e.*, iron-free dry, orthorhombic wadsleyite, Finger et al., 1993),
- The different interatomic potentials: Buckingham, Morse, three-body interactions for the various core and shell interactions involved with the defect
- The type of defect (*i.g.*, cation vacancy, interstitial hydrogen, incorporation of 1, 2, 3 or 4 hydroxyl groups) and its size; in this study calibrated at 12 Å.

The energy minimization and the simulations are considered to be valid when the resulting stretching frequency is positive. Obtaining positive frequencies confirms that the structure achieves a stable state, which requires a minimum of energy. Negative frequencies imply that the structure is not stable (the minimization is not

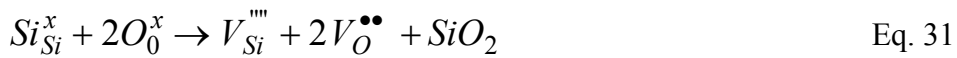
achieved). If this problem occurred, it was solved by choosing a different algorithm for energy minimization for a given defect (BFGS or RFO or both). Obtaining a positive frequency validates the simulation and give the corresponding infrared frequencies for the hydrated defect studied.

### 4.5.3. Hydrous defects

Various intrinsic defects were under consideration in this simulation of iron-free orthorhombic wadsleyite:

- $V_O^{\bullet\bullet}$ , oxygen vacancy for each oxygen, O<sub>1</sub>, O<sub>2</sub>, O<sub>3</sub> and O<sub>4</sub>
- $V_{Mg}^{\bullet\bullet}$ , magnesium vacancy for Mg<sub>1</sub>, Mg<sub>2</sub> and Mg<sub>3</sub>
- $V_{Si}^{\bullet\bullet\bullet\bullet}$ , silicon vacancy

The formation of intrinsic vacancies can be described by the following reactions:



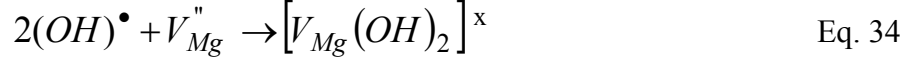
Wright and Catlow (1996) already calculated such simple vacancy defect energies but not for specific cation sites and only the lower calculated energies were reported (Wright and Catlow, 1996). As in Wright and Catlow (1996), calculations on hydrous defect were performed within oxygen vacancies but also for Mg vacancies and for the first time, the defect energy for a partially and fully hydrated silicon vacancy was calculated. For each calculation, numerous different starting positions for the proton were considered.

The associated defects investigated can be described by the following reactions:

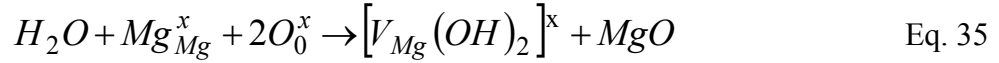
- Proton incorporation as an interstitial,



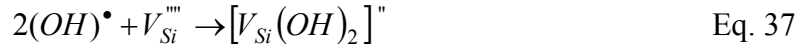
- One and two hydroxyl group(s) associated with a Mg vacancy and bonded to different  $O_x$ ,



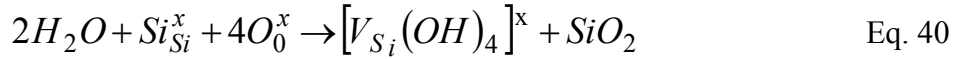
or



- One, two, three and four hydroxyl group(s) associated with a silicon vacancy and bonded to different  $O_x$ .



or



For all of the defects involving hydroxyl groups, various orientations of the OH dipole were tested. The present approach considers only isolated defects (or small clusters) and not large clusters as in the study of Braithwaite et al. (2002).

#### 4.5.4. Results

##### *Intrinsic defects*

Tables 4.5.1 and 4.5.2 present the calculated energies for intrinsic defects in iron-free wadsleyite. In an anhydrous system (Table 4.5.1), O1 is the most favorable oxygen site for vacancy formation with an energy of 24.44 eV ( $\sim 2358 \text{ kJ.mol}^{-1}$ ) but the Mg1 site is slightly more favourable with a vacancy energy of 24.17 eV. Notice that the Mg3 vacancy and O1 vacancy are very similar in terms of energy. Potential errors on

energies due to the model are very difficult to evaluate (Wright and Walker, person. comm.). However, errors due to the region I calibration (“radius calibration”) are around 0.01eV. Vacancies on O1, Mg1 or Mg3 are then considered as energetically favourable and therefore as potential sites for hydrogen incorporation.

**Table 4.5.1** Energies of vacancies in wadsleyite.

Defect	Defect energy (eV)
$V_{\text{Mg1}}''$	24.17
$V_{\text{Mg2}}''$	25.15
$V_{\text{Mg3}}''$	24.48
$V_{\text{O1}}^{\bullet\bullet}$	24.44
$V_{\text{O2}}^{\bullet\bullet}$	26.17
$V_{\text{O3}}^{\bullet\bullet}$	25.35
$V_{\text{O4}}^{\bullet\bullet}$	25.11
$V_{\text{Si}}^{\bullet\bullet\bullet}$	102.98

Table 4.5.2 presents the calculated defect energies for hydrogen incorporation (embedded proton) into the structure. Here again, O1 is the most favorable oxygen site for hydroxyl with an energy of 15.33 eV (1479 kJ.mol<sup>-1</sup>), followed by O4. These energies are used later to calculate reaction energies as discussed in the previous section. The corresponding infrared frequencies for such embedded hydrogen atoms are also given but they do not correspond exactly to frequencies previously observed by FTIR on experimentally synthesized hydrous iron-free wadsleyite (Bolfan-Casanova et al. 2000, Kohn et al. 2002, Jacobsen et al. 2004). All the frequencies presented here are too high by at least 40 cm<sup>-1</sup>.

**Table 4.5.2** Embedded protons bonded to oxygen within defect-free wadsleyite with corresponding energies and IR frequencies.

Defect	Energy (eV)	Frequency (cm <sup>-1</sup> )
$(OH)_{(01)}^{\bullet}$	15.33	3848
$(OH)_{(02)}^{\bullet}$	17.31	3903
$(OH)_{(03)}^{\bullet}$	16.87	3658
$(OH)_{(04)}^{\bullet}$	16.74	3753

*Associated defects and IR frequencies*

Table 4.5.3 presents the results of simulations for hydrous defects associated with cationic vacancies. O1 is still the most favorable site to fix hydrogen in association with a vacancy on Mg3 or on Mg2. Contrary to a dry vacancy; Mg1 is no longer the favorable site. Incorporation of a second proton reveals that O1 and O3 (located on the median plane of the Mg3 octahedron) are the most favorable oxygen atoms to fix hydroxyl groups. Notice that the difference in energy between the three associated defects  $[V_{Mg1} \cdot (OH)_{(04)} \cdot (OH)_{(04)}]^X$ ,  $[V_{Mg2} \cdot (OH)_{(01)} \cdot (OH)_{(02)}]^X$ , and  $[V_{Mg3} \cdot (OH)_{(01)} \cdot (OH)_{(03)}]^X$  is very low, with a variation of only 1.2 %.

The energies of hydroxyl incorporation associated with a silicon vacancy (Table 4.5.3) are calculated here for the first time. The energies are very high and the FTIR frequencies do not correspond to experimental IR measurements of iron-free wadsleyite. Despite the fact that such high energies were expected for hydrated silicon vacancies, it is important to quantify and verify these high energies associated with this type of defect.

All of the oxygen and hydrogen coordinates, O-H distances and the orientation of the hydroxyl dipoles are reported in appendix 4.

### 4.5.5. Discussion

As Smyth predicted (1987) and as other computer simulations including the present study show, O1 is the most favorable site for hydrogen incorporation in iron-free wadsleyite (charge balanced by Mg vacancies). As shown in Table 4.5.4, our computer simulation with GULP is in fair agreement with the *ab-initio* (DFT) calculation from Haiber et al. (1997) and permits to improve the calculation from Wright and Catlow (1996), which yielded the same defect energy for O3 and O4.

Furthermore, this study shows that a doubly-protonated Mg<sub>3</sub> vacancy, involving two O1 and two O3 on the median plane of the octahedral is the most favourable hydrous defect in iron-free wadsleyite. Such details were not considered in the study of Wright and Catlow (1996) and Haiber et al. (1997) due to computational limitations at the time. Logically, the infrared spectra must reflect this hydration configuration. Obviously, associated IR frequencies calculated together with the defect energies do not correspond well with experimental hydroxyl stretching frequencies within wadsleyite.

#### *IR frequencies simulations*

Interpreting IR spectra and assigning IR bands to specific hydrous point defects is difficult for hydrous wadsleyite. Figure 4.5.5 presents unpublished polarized IR spectra of iron-free wadsleyite (Jacobsen et al. 2004) containing various amount of water: sample WH388 contains around 2800 wt ppm H<sub>2</sub>O and WH304 around 120 wt ppm H<sub>2</sub>O. These values were obtained using the calibration of Paterson for polarized spectra.

The calculated frequencies for hydroxyl groups do not correspond to the experimental observations, certainly due to the high error on the calculated IR frequencies. GULP has the same disadvantage as the DFT method, which yields IR frequencies with an error of more than  $\pm 10\%$ . However, Braithwaite et al. (2003) have performed DFT calculations on hydroxyl in forsterite using a cluster approach, which gives IR frequencies closer to experimental observations within  $\pm 10\%$ .

#### 4.5. Results: Computer simulation of hydrous defects in iron-free wadsleyite

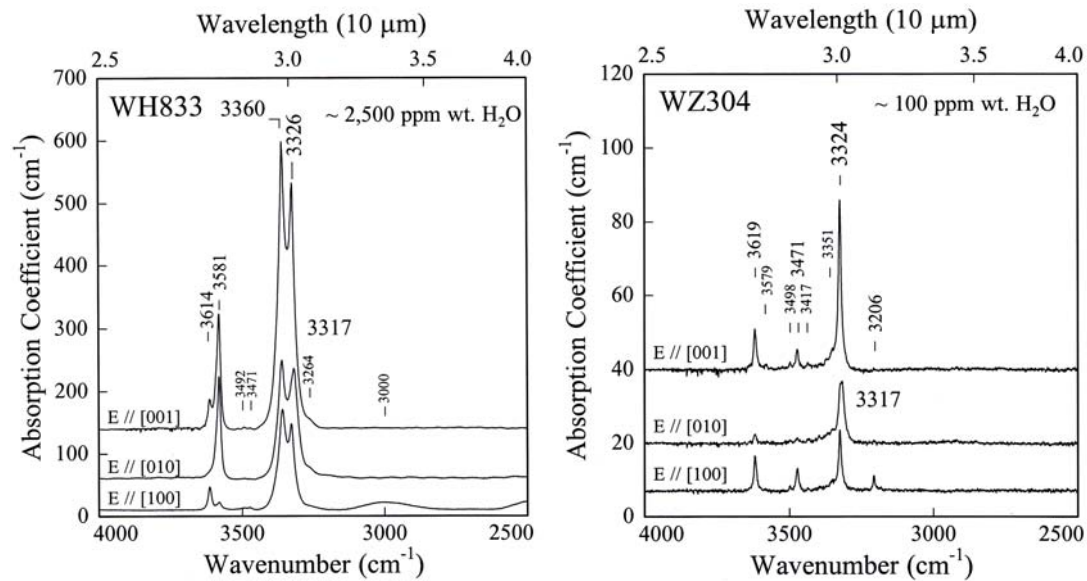
Nevertheless, in these calculations, errors in the IR frequencies do not correspond to similar errors in calculated energies, because these energies were determined using an electrostatic model.

**Table 4.5.3** Proton defects with calculated energies, reaction energies and IR frequencies

Defect	Defect energy (eV)	Energy of reaction (eV)	Frequency (cm <sup>-1</sup> )
$[V_{Mg1} \cdot (OH)_{(04)}]'$	38.72	-2.5	3708
$[V_{Mg2} \cdot (OH)_{(01)}]'$	38.21	-2.47	3751
$[V_{Mg3} \cdot (OH)_{(01)}]'$	37.98	-2.05	3728
$[V_{Mg1} \cdot (OH)_{(04)} \cdot (OH)_{(04)}]^x$	53.64	-4.01	3761-3740
$[V_{Mg2} \cdot (OH)_{(01)} \cdot (OH)_{(02)}]^x$	53.83	-4.17	3833-3743
$[V_{Mg3} \cdot (OH)_{(01)} \cdot (OH)_{(03)}]^x$	53.17	-3.71	3768-3735
$[V_{Si} \cdot (OH)_{(03)}]'''$	112.80	-7.05	3983
$[V_{Si} \cdot (OH)_{(04)} \cdot (OH)_{(04)}]''$	123.80	-12.59	3860-3809
$[V_{Si} \cdot (OH)_{(04)} \cdot (OH)_{(04)} \cdot (OH)_{(03)}]'$	135.56	-17.77	3864-3708-3907
$[V_{Si} \cdot (OH)_{(04)} \cdot (OH)_{(04)} \cdot (OH)_{(03)} \cdot (OH)_{(02)}]^x$	175.18	4.54	3519-3719- 3394-2201

**Table 4.5.4** Defect energies from Mott-Littleton simulation and absorption energy from DFT simulation for equivalent oxygen sites.

	Defect energy (eV)		Absorption energy (eV)	
	This study GULP	Wright and Catlow, 1996, CASCADE	O1	Haiber et al. 1997 <i>ab-initio</i> DFT
$(OH)_{(01)}^\bullet$	15.33	15.77	O1	13.5
$(OH)_{(02)}^\bullet$	17.31	17.31	O2	12.5
$(OH)_{(03)}^\bullet$	16.87	17.21	O3	12.8
$(OH)_{(04)}^\bullet$	16.74	17.21	O4	13.0

**Figure 4.5.5** Polarized IR spectra of two samples of hydrous iron-free wadsleyite (WH833 and WH304) (reproduced from Jacobsen et al., 2004 - *with the courtesy of S.D. Jacobsen.*).

Regardless of the values of the IR frequencies, one could still consider the orientation of the dipole as valid and one could try to assign IR bands using recent polarized IR spectra of wadsleyite from Jacobsen et al. (2004). However, this was not possible due to an error in the program that leads to orientation, making difficult the assignment of IR bands to hydrous defects.

#### **4.5.6. Conclusion**

The computer simulations reported in this chapter provide further insights into the structure of hydrous wadsleyite but they do not resolve completely the hydration process in iron-free wadsleyite. GULP allows a rapid evaluation of defect energies in dry and hydrous wadsleyite. The model gives relatively good agreement with DFT results. Unfortunately, simulations do not yet provide satisfactory infrared frequencies for a given hydroxyl dipole within a silicate. Computer simulations are definitively helpful in studying hydrous structures but they are not yet powerful enough to allow a rapid, easy and valid simulation of full infrared spectra. However, the continuing improvement in simulation methods and computer capabilities should allow such calculations in a few years.



## 5. Conclusion

This thesis consists of a series of studies intended to improve our understanding of water storage within the Earth's mantle and its role in mantle processes. Two minerals were studied,  $\alpha$ -(Mg<sub>x</sub>,Fe<sub>1-x</sub>)<sub>2</sub>SiO<sub>4</sub> (olivine), the main constituent of the upper mantle and  $\beta$ -Mg<sub>2</sub>SiO<sub>4</sub> (wadsleyite) which is present in the upper part of the transition zone.

In particular, I have measured the rates at which water-derived species diffuse within natural olivine ( $\alpha$ -(Mg<sub>0.9</sub>Fe<sub>0.1</sub>)<sub>2</sub>SiO<sub>4</sub>) and synthetic forsterite ( $\alpha$ -Mg<sub>2</sub>SiO<sub>4</sub>) single crystals, and determined in detail the mechanisms of transport. Two processes of incorporation were characterized: (1) a lower temperature / shorter time scale redox-exchange process (where protons diffuse within the olivine structure through cooperative diffusion with electron holes). The measurement of the anisotropy of diffusion shows that the [100] axis is the fastest direction of diffusion and [001] the slowest. In iron-free forsterite, this mechanism does not occur; (2) a higher temperature / longer time scale process involving the associated diffusion of protons and metal vacancies. The measurement of the anisotropy of diffusion for this second process shows that the [001] axis is the fastest direction of diffusion and that diffusion parallel to the [100] and [010] axes occurs at a similar rate and is slower than parallel to the [001] axis. Significant amounts of hydrogen can be incorporated into the olivine structure by this second mechanism, which occurs in both natural iron-bearing olivine and iron-free forsterite. The rate of diffusion appears to be only weakly dependent on iron content. At 1000°C and for the respective fastest diffusion directions, the second process is about two orders of magnitude slower than the redox exchange process, with a diffusion coefficient around  $1.6 \cdot 10^{-12} \text{ m}^2\text{s}^{-1}$  ([001] axis). The new diffusivity laws obtained for iron-bearing olivine and forsterite are also of great interest for interpretation of magneto-telluric measurements of the Earth, as an active role for hydrogen diffusion has been suggested to explain the observed anisotropy in electrical behavior. The diffusivity laws given in this thesis will permit accurate 3D modelling of the combined electrical and seismic anisotropy datasets to include the effect of water diffusion.

For the first time, dehydration profiles have been observed in untreated mantle-derived olivine crystals. These olivine grains occur within garnet-bearing peridotite xenoliths from the basalt plateau Pali-Aike in southernmost South America (Patagonia). These dehydration profiles show that previous determinations of the amount of water stored in the upper mantle based on measurements of olivine within mantle xenoliths underestimate the true amount of water at depth. Furthermore, I have been able to interpret the signature of these dehydration profiles in olivine using the new diffusion laws presented in this study to constrain the ascent rate of the xenoliths from the deep mantle source to the surface. The resulting durations of diffusion yield ascent rates between  $\sim 4$  m/s and  $\sim 7$  m/s. These results suggest an extremely rapid ascent toward the surface, which was already anticipated from the very fresh appearance of the peridotite xenoliths. Thus, dehydration profiles in mantle-derived olivine provide an innovative tool to quantify ascent rate for xenoliths and their entraining basalts that formed recent basalt plateau. This opens up the ground for many further studies.

Going deeper in the Earth's mantle, the temperature and pressure dependencies of water solubility in iron-free wadsleyite were investigated experimentally. The results show no clear effect of pressure, but that the water solubility decreases significantly with increasing temperature, suggesting a strong fractionation of water between wadsleyite in the upper transition zone and the ringwoodite in the lower transition zone. This new result would suggest that, since the Hadean, water has been progressively transferred from the lower to the upper transition zone. Moreover, the presence or absence of a detectable 520 km seismic discontinuity may be related to the effect of temperature on the fractionation of water between ringwoodite and wadsleyite.

Finally, computer simulations were performed in order to calculate infrared frequencies for very well defined hydroxyl defects within the structure of iron-free wadsleyite. Using GULP, I calculated precise defect energies for hydrous wadsleyite. However, this method needs to be improved in order to be able to accurately predict infrared frequencies.

## 6. References

- Aines R. D. and Rossman G. R. (1984) Water in minerals? A peak in the infrared. *J. Geophys. Res. (B6)* **89**:4059-4071.
- Anderson K., Borchart G., Scherrer S. and Weber S. (1989) Self-diffusion in Mg<sub>2</sub>SiO<sub>4</sub> at high pressure: a model case study for SIMS analyses on ceramic surfaces. *Fesenius Z. Anal. Chem.* **333**:383-385.
- Arndt N.T., Ginibre C., Chauvel C., Albarède F., Cheadle M., Herzberg C., Jenner G. and Lahaye Y. (1998) Were Komatiites wet? *Geology* **26**:739-742.
- Bahr K. and Simpson F. (2002) Electrical anisotropy below low- and fast- plates: palaeoflow in the upper mantle? *Science*, **295**:1270-1272.
- Bai Q. and Kohlstedt D.L. (1992) Substantial hydrogen solubility in olivine and implications for water storage in the mantle, *Nature*, **357**:672-674.
- Bai Q. and Kohlstedt D.L. (1993) Effects of chemical environment on the solubility and incorporation mechanism for hydrogen in olivine. *Phys. Chem. Minerals*, **19**:460-471.
- Bai Q., Mackwell S.J. and Kohlstedt D.L. (1991) High-temperature creep of olivine single crystals. 1. Mechanical results for buffered samples. *J. Geophys. Res.*, **96**:2441-2463.
- Béjina F. and Jaoul O. (1997) Silicon diffusion in silicate minerals. *Earth Planet. Sci. Lett.*, **153**:229-238.
- Bell D.R. and Rossman G.R. (1992) Water in Earth's mantle: The role of nominally anhydrous minerals. *Science*, **255**:1391-1397.
- Bell D.R., Ihinger P.D. and Rossman G.R. (1995) Quantitative analysis of trace OH in garnet and pyroxenes. *Am. Mineral.*, **80**:465-474.
- Bell D.R., Rossman G.R., Maldener J., Endisch D. and Rauch F. (2003) Hydroxide in olivine: a quantitative determination of the absolute amount and calibration of the IR spectrum. *J. Geophys. Res.*, **108**: doi : 1029/2001JB000679.
- Beran A. and Putnis A. (1983) A model of the OH position in olivine derived from infrared-spectroscopy investigations. *Phys. Chem. Minerals*, **9**:57-60.
- Beran A. and Zemman J. (1969) Über OH-gruppen in Olivin. *Österreich Akademie des Wissenschaften*, **3**:73-74.

- Bercovici D. and Karato S.-I. (2003) Whole-mantle convection and the transition-zone water filter. *Nature*, **425**: 39-44.
- Binns R.A., Davis R.J. and Reed S.J.B. (1969) Ringwoodite, natural (Mg, Fe)<sub>2</sub>SiO<sub>4</sub> spinel in the Tenham meteorite. *Nature*, **211**: 943-944.
- Blanchard M. and Ingrin J. (2004) Hydrogen diffusion in Dora Maira pyrope. *Phys. Chem. Mineral*. In press.
- Bohlen S. R. (1984) Equilibria for precise pressure calibration and frictionless furnace assembly for the piston-cylinder apparatus. *N. Jh. Mineral Mt.*, **9**:404-412.
- Bolfan-Casanova N. (2000) The distribution of water in the Earth's mantle: an experimental and infrared study. Ph.D. thesis, Bayerisches Geoinstitut, Universität Bayreuth: pp 169.
- Bolfan-Casanova N., Keppler H. and Rubie D. C. (2003) Water partitioning at 660 km depth and evidence for very low water solubility in magnesium silicate perovskite. *Geophys. Res. Lett.*, **30**:doi:1029/2003GL017182.
- Bolfan-Casanova N., Keppler H. and Rubie D.C. (2002) Hydroxyl in MgSiO<sub>3</sub> akimotoite: A polarized and high-pressure IR study. *Am. Mineral.* **87**:603-608.
- Bolfan-Casanova N., Mackwell S.J., Keppler H., McCammon C.A. and Rubie D.C. (2002) Pressure dependence of H solubility in magnesiowüstite up to 25 GPa: Implications for the storage of water in the Earth's lower mantle. *Geophys. Res. Lett.*, **29**:89/1-89/4.
- Boyd F.R. and England J.L. (1960) Apparatus for phase-equilibrium measurements at pressures up to 50 kilobars and temperature up to 1,750°C. *J. Geophys. Res.*, **65**:741-748.
- Braithwaite J.S., Wright K. and Catlow C.R.A. (2003) A theoretical study of energetics and IR frequencies of hydroxyl defects in forsterite. *J. Geophys. Res.* **108**:doi: 10.1029/2002JB002126.
- Brodholt J. and Refson K. (2000) An *ab initio* study of hydrogen in forsterite and a possible mechanism for hydrolytic weakening. *J. Geophys. Res.*, **105**:18,977-18,982.
- Bromiley G.D. and Keppler H. (2004) An experimental investigation of hydroxyl solubility in jadeite and Na-rich clinopyroxenes. *Contrib. Mineral. Petrol.*, **147**: doi: 1029/2001JB000679.

- Bromiley G.D., Keppler H., McCammon C., Bromiley F. and Jacobsen S.D. (2004) Hydrogen solubility and speciation in natural, gem-quality Cr-Diopside. *Am. Mineral*, in press.
- Cande S.C. and Leslie R.B. (1986) Late Cenozoic tectonics of the Southern Chile Trench. *J. Geophys. Res.*, **91**:471-496.
- Canil D. (1994) Stability of clinopyroxene at pressure-temperature conditions of the transition region. *Phys. Earth Planet. Inter.*, **86**: 25-34.
- Carpenter-Wood S. (2001) The kinetics of hydrogen diffusion in single crystal orthopyroxene. Ph.D thesis. Dept. Geosciences, Penn State University: pp 210.
- Carpenter-Woods S., Mackwell S.J. and Dyar D. (2000) Hydrogen in diopside: Diffusion profiles. *Am. Mineral.*, **85**:480-487.
- Carslaw H.S. and Jaeger J.C. (1959) Conduction of heat in solids, 2nd ed. Clarendon, Oxford: pp 510.
- Catlow C.R.A and Mackrodt W.C. (1982) Theory of simulation methods for lattice and defect energy calculations in crystal. *Lect. Notes Phys.*, **166**:3-20.
- Chakraborty S., Farver J.R., Yund R.A. and Rubie D.C. (1994) Mg tracer diffusion in synthetic forsterite and San Carlos olivine as a function of P, T and  $fO_2$ . *Phys. Chem. Minerals*, **21**: 489-500.
- Chopra P.N. and Paterson M.S. (1984) The role of water in the deformation of dunite. *J. Geophys. Res.*, **89**:7861-7876.
- Constable S. and Duba A. (2002) Diffusion and mobility of electrically conducting defects in olivine. *Phys. Chem. Minerals*, **29**:446-454.
- Crank J. (1956) The mathematics of diffusion, Oxford Science Publication, Oxford: pp 414.
- d'Acremont E., Leroy S. and Burov E.B. (2003) Numerical modelling of a mantle plume: the plume head-lithosphere interaction in the formation of an oceanic large igneous province. *Earth Planet. Sci. Lett.* **206**:379-396.
- Deer W.A., Howie R.A. and Zussman J. (1997) Rock-forming minerals, orthosilicates, Volume 1A. The Geological Society, London: pp 919.
- Deloule E., Albarède F. and Sheppard M.F. (1991) Hydrogen isotope heterogeneities in the mantle from ion probe analysis of amphiboles from ultramafic rocks. *Earth Planet. Sci. Lett.*, **105**:543-553.
- Deloule E., Paillat O., Pichavant M. and Scaillet B. (1995) Ion probe determination of water in silicate glasses: methods and applications. *Chem. Geol.*, **125**:19-28.

- Dick B.G. and Overhauser A.W. (1958) Theory of the dielectric constants of alkali halide crystals. *Phys. Rev.*, **112**:90.
- Dohmen R., Becker H.W., Meißner E., Etzel T. and Chakraborty S. (2002) Production of silicate thin films using pulsed laser deposit (PLD) and applications to studies in mineral kinetics. *Eur. J. Minerals*, **14**:1155-1168.
- D'Orazio M., Agostini S., Innocenti F., Haller M.J., Manetti P. and Mazzarini F. (2001) Slab-window-related magmatism from southernmost South America: the Late Miocene mafic volcanics from the Estancia Glencross Area (~ 52°S, Argentina-Chile). *Lithos*, **57**:67-89.
- D'Orazio M., Agostini S., Mazzarini F., Innocenti F., Manetti P., Haller M.J. and Lahsen A. (2000) The Pali-Aike Volcanic Field, Patagonia: slab-window magmatism near the tip of South America. *Tectonophysics*, **321**:407-427.
- Dyar M.D., Martin S.V., Mackwell S.J., Carpenter S., Grant C.A. and McGuire A.V. (1996) Crystal chemistry of Fe<sup>3+</sup>, H<sup>+</sup>, and D/H in mantle-derived augite from Dish Hill: Implications for alteration during transport. In: Dyar D, McCammon CA and Schaefer MW Mineral Spectroscopy: A Tribute to Roger G. Burns, The Geochemical Society, pp 289-304.
- Fick A. (1855). Über Diffusion. *Annln. Phys.*, Leipzig, **170**: 59.
- Finger L.W., Hazen R.M., Zhang J., Ko J. and Navrotsky A. (1993) The effect of Fe on the crystal structure of wadsleyite  $\beta$ -(Mg<sub>1-x</sub>,Fe<sub>x</sub>)<sub>2</sub>SiO<sub>4</sub>, 0.00 ≤ x ≤ 0.40. *Phys. Chem. Minerals*, **19**: 391-368.
- Freund F. and Oberheuser G. (1986) Water dissolved in olivine. *J. Geophys. Res.*, **91**:745-761.
- Frey F. and Prinz M. (1978) Ultramafic inclusions from San Carlos, Arizona: Petrologic and geochemical data bearing on their petrogenesis. *Earth Planet. Sci. Lett.*, **38**: 129-176.
- Gaetani G.A. and Grove T.L. (1998) The influence of water on melting of mantle peridotite. *Contrib. Mineral. Petrol.* **131**:323-346.
- Gale J. D. (1997) GULP: a computer program for the symmetry-adapted simulation of solids. *J. Chem. Soc. Faraday Trans.*, **1**:629-637.
- Gale J. and Rohl A. L. (2003) the general utility lattice program (GULP). *Mol. Simul.* **29**:291-341.

- Ganguly J, Yang H and Gkose S (1994) Thermal history of mesosiderites: Quantitative constrains from compositional zoning and Fe-Mg ordering in orthopyroxene, *Geochim. Cosmochim. Acta*, **58**:2711-2723.
- Ganguly J., Chakraborty S., Sharp T. and Rumble D. (1996) Constrain on the time scale of biotite-grade metamorphism during Acadian orogeny from a natural garnet-garnet diffusion couple. *Am. Mineral.*, **81**:1208-1216
- Ganguly J., and Tirone M. (2001) Relationship between cooling rate and cooling age of a mineral: Theory and applications to meteorites. *Meteoritics and Planetary Science*, **36**: 67 – 176.
- Gasparik T. (1993) The role of volatiles in the transition zone. *J. Geophys. Res.*, **98**:4287-4299.
- Gatzemeier A. and Bahr K. (2003) How electrical conductivity measurement can contribute to identify water in the upper mantle. *Geophys. Res. Abstract*, **5**: 09941.
- Gérard O. and Jaoul O. (1989) Oxygen diffusion in San Carlos olivine. *J. Geophys. Res.* **94**(B4): 4119-4128.
- Green D.H. and Fallon T.J. (1998) Pyrolite: A Ringwood concept and its current expression, In: *The Earth's mantle, composition, structure and evolution*, ed. I. Jackson, Cambridge university press, Cambridge: pp 311-380.
- Haiber M., Ballone P. and Parrinello M. (1997) Structure and dynamics of protonated Mg<sub>2</sub>SiO<sub>4</sub>: An ab-initio molecular dynamics study. *Am. Mineral.*, **82**:913-922.
- Hauri E., Wang J., Dixon J. E., King P. L., Mandeville C. and Newman S. (2002). SIMS analysis of volatiles in silicate glasses 1. Calibration, matrix effects and comparisons with FTIR. *Chem. Geol.*, **183**:99-114.
- Hercule S. and Ingrin J. (1999) Hydrogen in diopside: Diffusion, kinetics of extraction-incorporation, and solubility. *Am. Mineral.*, **84**:1577-1587.
- Hirsch, L., and Shankland, T.J. (1993) Quantitative olivine-defect chemical model: insights on electrical conduction, diffusion, and the role of Fe content. *Geophys. J. Int.*, **114**, 21-35.
- Hirsch, L., Shankland, T.J., and Duba, A. (1993) Electrical conduction and polaron mobility in Fe-bearing olivine. *Geophys. J. Int.*, **114**, 36-44.
- Hirth G. and Kohlstedt D.L. (1996) Water in the oceanic upper mantle: implications for rheology, melt extraction and the evolution of the lithosphere. *Earth Planet. Sci. Lett.*, **144**:93-108.

- Holloway J.R., Dixon J.E. and Pawley A.L. (1992) An internally heated, rapid-quench, high-pressure vessel. *Am. Mineral.* **77**: 643-646.
- Houlier B., Cheraghmakani M. and Jaoul O. (1990) Silicon diffusion in San Carlos olivine. *Phys. Earth. Planet. Inter.*, **62**:329-340.
- Houlier B., Jaoul O., Abel F. and Liebermann R. C. (1988) Oxygen and silicon self-diffusion in natural olivine at T = 1300°C. *Phys. Earth. Planet. Inter.*, **50**:240-250.
- Hudson P., Baker D.R. and Toft P.B. (1994) A high-temperature assembly for 1.91 cm (3/4-in) piston-cylinder apparatus. *Am. Mineral.*, **79**:145-147.
- Ihinger P.D., Hervig R. and Mcmillan P.F. (1994) Analytical methods for volatiles in glasses. In: Volatiles in Magmas, eds. M.R. Carroll and J.R. Holloway, Mineralogical Society of America, Vol.30, Washington D.C.: pp 67-121.
- Ingrin J. and Skogby H. (2000) Hydrogen in nominally anhydrous upper-mantle minerals: concentration levels and implications. *Eur. J. Minerals*, **12**:543-570.
- Ingrin J., Hercule S. and Charton T. (1995) Diffusion of hydrogen in diopside: Results of dehydration experiments. *J. Geophys. Res.*, **100**:15,489-15,499.
- Inoue T. (1994) Effect of water on the melting phase relation and melt composition in the system Mg<sub>2</sub>SiO<sub>4</sub>-MgSiO<sub>3</sub>-H<sub>2</sub>O up to 15 GPa. *Phys. Earth Planet. Inter.*, **85**: 237-263.
- Inoue T., Yurimoto H. and Kudoh Y. (1995) Hydrous modified spinel, Mg<sub>1.75</sub>SiH<sub>0.5</sub>O<sub>4</sub>: a new water reservoir in the mantle transition region. *Geophys. Res. Lett.*, **22**(2): 117-120.
- Jacobsen S.D., Demouchy S., Frost D., Ballaran, T.B. and Kung, J. (2004) A Systematic study of OH in hydrous wadsleyite from polarized FTIR spectroscopy and single-crystal X-ray diffraction: oxygen sites for hydrogen storage in Earth's interior, *American Mineralogist*, **89**, in press.
- Johannes W.P., Bell P.M., Mao H.K., Boettcher A.L., Chipman D.W., Hays J.F., Newton R.C. and Seifert F. (1971) An interlaboratory comparison of piston-cylinder pressure calibration using the albite breakdown reaction. *Contrib. Mineral. Petrol.*, **32**:24-38.
- Johnson E.A. (2003) Hydrogen in nominally anhydrous crystal minerals. Ph.D Thesis, California Institut of Technology: pp 305.

- Jurewicz A.J.G. and Watson E.B. (1988) Cations in olivine, Part 2: Diffusion in olivine xenocrysts, with application to petrology and mineral physics. *Contrib. Mineral. Petrol.* **99**:186-201.
- Karato S.-I. (1990) The role of hydrogen diffusivity in the electrical conductivity of the upper mantle. *Nature*, **347**:272-273.
- Karato S.-I. and Jung H. (1998) Water, partial melting and the origin of the seismic low velocity and high attenuation zone in the upper mantle. *Earth. Planet. Sci. Lett.*, **157**:193-207.
- Karato S.-I., Paterson M.S. and Fitzgerald J.D. (1986) Rheology of synthetic olivine aggregates: influence of grain size and water. *J. Geophys. Res.*, **91**:8151-8176.
- Kawamoto T., Hervig R.L. and Holloway J.R. (1996) Experimental evidence for a hydrous transition zone in the early Earth's mantle. *Earth Planet. Sci. Lett.*, **142**:587-592.
- Kilian R. and Stern C.R. (2002) Constraints on the interaction between slab melts and the mantle wedge from adakitic glass in peridotite xenoliths. *Eur. J. Minerals*, **14**:25-36.
- Koga K., Hauri E., Hirschmann M. and Bell D.R. (2003) Hydrogen concentration analysis using SIMS and FTIR: Comparison and calibration for nominally anhydrous minerals. *Geochem. Geophys. Geosys.*, **4**(2): 1019, doi: 10.1029/2002GC000378.
- Kohlstedt D.L. and Mackwell S.J. (1987) High-temperature stability of San Carlos olivine. *Contrib. Mineral. Petrol.*, **95**:226-230.
- Kohlstedt D.L. and Mackwell S.J. (1998) Diffusion of hydrogen and intrinsic point defects in olivine. *Z. Phys. Chem.*, **207**:147-162.
- Kohlstedt D.L. and Mackwell S.J. (1999) Solubility and diffusion of "water" in silicate minerals. In: *Microscopic Properties and Processes in Minerals*, eds. K. Wright and R. Catlow, Kluwer Academic Publishers, Netherlands: pp 539-559.
- Kohlstedt D.L., Keppler H. and Rubie D. C. (1996) Solubility of water in the  $\alpha$ ,  $\beta$  and  $\gamma$  phases of  $(\text{Mg,Fe})_2\text{SiO}_4$ . *Contrib. Mineral. Petrol.*, **123**:345-357.
- Kohn S.C., Brooker R., Frost D.J., Slesinger A.E. and Wood B.J. (2002) Ordering of hydroxyl defects in hydrous wadsleyite ( $\beta$ - $\text{Mg}_2\text{SiO}_4$ ). *Am. Mineral.*, **87**:293-301.

- Kröger, F.A. and Vink, H.J. (1956) Relation between the concentration of imperfections in crystalline solids. In: Solid State Physics 3, eds. F. Seitz, D. Turnhall, Academic Press, New York, pp 367-435.
- Lastovickova M. (1987) Electrical conductivity of some minerals at high temperature and for extended times. *Phys. Earth Planet. Inter.*, **45**:204-208.
- Lastovickova M. (1991) A review of laboratory measurements of electrical conductivity of rocks and minerals. *Phys. Earth Planet. Inter.*, **66**:1-11.
- Leeman W.P. and Scheidegger K. (1977) Olivine/liquid distribution coefficients and a test for crystal-liquid equilibrium. *Earth Planet. Sci. Lett.*, **35**:247-257.
- Lemaire C., Kohn S.C., and Brooker R.A. (2004) The effect of silica activity on the incorporation mechanisms of water in synthetic forsterite: a polarised infrared spectroscopic study. *Contrib. Mineral. Petrol.*, **147**:48-57.
- Libowitzky E. and Beran A. (1995) OH defects in forsterite. *Phys. Chem. Minerals*, **22**:387-392.
- Libowitzky E. and Rossman G.R. (1996) Principles of quantitative absorbance measurements in anisotropic crystals. *Phys. Chem. Minerals*, **23**:319-327.
- Litasov, K., Ohtani, E., Langenhorst, F., Yurimoto, H., Kubo, T., and Kondo, T. (2003) Water solubility in Mg-perovskites and water storage capacity in the lower mantle. *Earth Planet. Sci. Lett.*, **211**, 189-203.
- Locke J.R., Holloway J.R., Leinenweber K. and Hervig R. (2001) Effect of MgO/SiO<sub>2</sub> activity ratio on H<sub>2</sub>O solubility in forsterite. *Eos. Trans. AGU* 82 (47), Fall Meet. Suppl.:Abstract T21B-0890.
- Lu R. and Keppler H. (1997) Water solubility in pyrope to 100 kbar. *Contrib. Mineral. Petrol.*, **129**:35-42.
- Mackwell S.J. and Kohlstedt D.L. (1990) Diffusion of hydrogen in olivine: Implications for water in the mantle. *J. Geophys. Res.*, **95**:5079-5088.
- Mackwell S.J, Dimos D. and Kohlstedt D.L. (1988) Transient creep of olivine: Point-defect relaxation times. *Philos. Mag. A.*, **57**:779-789.
- Mackwell S.J., Kohlstedt D.L. and Paterson M.S. (1985) The role of water in the deformation of olivine single crystals. *J. Geophys. Res.*, **90**:11,319-11,333.
- Mackwell S. J. and Rubie D. C. (2000) Earth under strain. *Science*, **290**:1514-1515.
- Matveev S., O'Neill H. St.C, Ballaus C., Taylor W.R. and Green D.H. (2001) Effect of silica activity on OH<sup>-</sup> IR spectra of olivine: Implications for Low-*a*SiO<sub>2</sub> mantle metasomatism. *J. Petrol.*, **42**:721-729.

- McCammon, C.A. (1994) A Mössbauer milliprobe: Practical considerations, *Hyper Inter* 92, 1235-1239.
- McCammon C.A., Chaspar V. and Richards G.G. (1991) A technique for spatially resolved Mössbauer spectroscopy applied to quenched metallurgical slags, *Meas. Sci. Tech.*, **2**:657.
- McMillan P.F., Akaogi M., Sato R.K., Poe B. and Foley J. (1991) Hydroxyl groups in  $\beta$ -Mg<sub>2</sub>SiO<sub>4</sub>. *Am. Mineral.*, **76**:354-360.
- McMillan P.F., Hemley R.J. and Gillet P. (1996) Vibrational spectroscopy of mantle minerals. In: Mineral Spectroscopy: a tribute to Roger G. Burns, eds. M. D. Dyar, C. McCammon and M. W. Schaefer, The Geological Society, Houston : pp 175-213.
- Mercier J.-C.C. and Nicholas A. (1975) Textures and fabrics of the upper mantle peridotites as illustrated by xenoliths from basalts. *J. Petrol.*, **16**:454-487.
- Mierdel, K., and Keppler, H. (2004) The temperature dependence of water solubility in enstatite. *Contrib. Mineral. Petrol.*, in press.
- Miller G.H., Rossman G.R. and Harlow G.E. (1987) The natural occurrence of hydroxide in olivine. *Phys. Chem. Minerals*, **14**:461-472.
- Moore P.B. and Smith J.V. (1970) Crystal structure of  $\beta$ -Mg<sub>2</sub>SiO<sub>4</sub>: crystal-chemical and geophysical implications. *Phys. Earth Planet. Inter.*, **3**:166-177.
- Mott N.F. and Littleton M.J. (1938) Conduction in polar crystals. 1. Electrolytic conduction in solid salts. *Trans. Faraday Soc.*, **34**:485.
- Murakami M., Hirose K., Yurimoto H., Nakashima S. and Takafuji N. (2002) Water in the Earth's lower mantle. *Science*, **295**:1885-1887.
- Nakamura A. and Schmalzried H. (1983) On the nonstoichiometry and point defects of olivine. *Phys. Chem. Minerals*, **10**:27-37.
- Newman S., Epstein S., Stolper E., (1988) Water, carbon dioxide, and hydrogen isotopes in glasses from ca. 1340 A.D. eruption of the Mono craters, California: constraints on degassing phenomena and initial volatile content. *J. Volcano. Geotherm. Res.* **35**, 75-96.
- O'Neill H. St.C. (1987b) Free energies of formation of NiO, CoO, Ni<sub>2</sub>SiO<sub>4</sub>, and Co<sub>2</sub>SiO<sub>4</sub>. *Am. Mineral.*, **72**:280-291.

- O'Neill H. St.C. and Wall V.J. (1987a) The olivine-orthopyroxene-spinel oxygen geobarometer, the nickel precipitation curve, and the oxygen fugacity of Earth's upper mantle. *J. Petrol.*, **28**:1169-1191.
- Ohtani E., Mizobata H. and Yurimoto H., (2000) Stability of dense hydrous magnesium silicate phases in the systems  $Mg_2SiO_4-H_2O$  and  $MgSiO_3-H_2O$  at pressure up to 27 GPa. *Phys. Chem. Minerals*, **27**:533-544.
- Paterson M.S. (1982) The determination of hydroxyl by infrared absorption in quartz, silicate glasses and similar materials. *Bull. Minéral.*, **105**:20-29.
- Philibert J. (1991) Atom movements, diffusion and mass transport in solids, Les éditions de physiques, les Ullis, France: pp 577.
- Price G.D., Putnis A., Agrell S.O. and Smith D.G.W. (1983) Wadsleyite, natural  $\beta$ - $(Mg,Fe)_2SiO_4$  from the Peace River meteorite. *Can. Mineral.*, **21**: 29-35.
- Putnis A. (1992) Introduction to mineral sciences. Cambridge University Press, Cambridge: pp 457.
- Raterron P., Chopra P. and Doukhan J.C. (2000)  $SiO_2$  precipitation in olivine: ATEM investigation of two dunites annealed at 300 MPa in hydrous conditions. *Earth. Planet. Sci. Lett.* **180**:415-423.
- Rauch M. (2000) Der Einbau von Wasser in Pyroxene. Ph.D. thesis, Bayerisches Geoinstitut, Universität Bayreuth: pp 141.
- Rauch M. and Keppler H. (2002) Water solubility in orthopyroxene. *Contrib. Mineral. Petrol.*, **143**:525-536.
- Richmond N.C. (1999) Computer simulation study of iron, aluminium and manganese in mantle silicates. Ph.D. thesis. University College London: pp 150.
- Ringwood A.E. (1962a) A model for the upper mantle, *J. Geophys. Res.*, **67**:857-66
- Ringwood A.E. (1962b) A model for the upper mantle. 2, *J. Geophys. Res.*, **67**:4473-7
- Ringwood A.E. and Major A. (1966) Synthesis of diamonds. *Aust. J. Chem.*, **19**:1955-1969.
- Rubie D.C., (1999) Characterising the sample environment in the multi-anvil high-pressure experiments. *Phase Transitions*. **68**: 431-451.
- Rutherford M.J. and Devine J.D. (2003) Magmatic conditions and magma ascent as indicated by hornblende phase equilibria and reactions in the 1995-2002 Soufrière Hills magma. *J. Petrol.*, **44**:1433-1454.

- Ryerson F.J., Durham W.B., Cherniak D.J. and Lanford W.A. (1989) Oxygen diffusion in olivine: Effect of oxygen fugacity and implications for creep. *J. Geophys. Res.* **94**(B4):4105-4118.
- Sato H. (1986) High temperature a.c. electrical properties of olivine single crystal with varying oxygen partial pressure: Implications for the point defect chemistry. *Earth Planet. Inter.*, **41**:269-282.
- Schmalzried H. (1981) Solid State Reactions, 2nd ed. Verlag Chemie, Weinheim: pp 254.
- Selverstone J. and Stern C.R. (1983) Petrochemistry and recrystallization history of granulite xenoliths from the Pali-Aike field, Chile. *Am. Mineral.* **68**:1102-1112.
- Serway R A., Moses C. J. and Moyer C. A. (1997) Moderns Physics, 2<sup>nd</sup> ed. Saunders Colle: pp 580.
- Shaw C. (2004) The temporal evolution of three magmatic systems in the west Eifel volcanic field, Germany. *J. Volcanol. Geotherm. Res.* **131**:213-240.
- Siesler H.M., Ozaki Y., Kawata S. and Heise H.M., (2002) Near-infrared spectroscopy, principles, instruments, applications. Publishing Wiley-VCH, Weinheim: pp 360.
- Simpson F. (2002a) Intensity and direction of lattice-preferred orientation of olivine: are electrical and seismic anisotropies of the Australian mantle reconcilable? *Earth Planet. Sci. Lett.*, **203**:535-547.
- Simpson F. (2002b) A comparison of electromagnetic distortion and resolution of upper mantle conductivities beneath continental Europe and the Mediterranean using islands as windows. *Phys. Earth Planet. Inter.*, **129**:117-130.
- Skewes M.A. and Stern C.R. (1979) Petrology and geochemistry of alkali basalts and ultramafic inclusions from the Pali-Aike volcanic field in southern Chile and the origin of the Patagonian plateau lavas. *J. Volcanol. Geotherm. Res.*, **6**:3-25.
- Skogby H. (1994) OH incorporation in synthetic clinopyroxene. *Am. Mineral.*, **79**:240-249.
- Skogby H., Bell D.R. and Rossman G.R. (1990) Hydroxide in pyroxene: Variations in the natural environment. *Am. Mineral.*, **75**:764-774.
- Smyth J.R. (1987)  $\beta$ -Mg<sub>2</sub>SiO<sub>4</sub>: A potential host for water in the mantle? *Am. Mineral.*, **72**:1051-1055.

- Smyth J.R. (1994) A crystallographic model for hydrous wadsleyite ( $\beta$ - $\text{Mg}_2\text{SiO}_4$ ): An ocean in the Earth's interior? *Am. Mineral.*, **79**:1021-1024.
- Smyth J.R., Kawamoto T., Jacobsen S.D., Swope R.J., Hervig R.L. and Holloway J.R. (1997) Crystal structure of monoclinic hydrous wadsleyite  $\beta$ - $(\text{Mg}, \text{Fe})_2\text{SiO}_4$ . *Am. Mineral.*, **82**:270-275.
- Smyth D.M. and Stocker R.L. (1975) Point defects and non-stoichiometry in forsterite. *Phys. Earth Planet. Inter.*, **10**:183-192.
- Sobolev A. and Chaussidon M. (1996)  $\text{H}_2\text{O}$  concentrations in primary melts from supra-subduction zones and mid-ocean ridges: implications for  $\text{H}_2\text{O}$  storage and recycling in the mantle. *Earth. Planet. Sci. Lett.*, **137**:45-55.
- Spera F.J. (1980) Aspects of magma transport. In: Physics of Magmatic processes, ed. R.B. Hargraves, Princeton University Press, New Jersey: pp 265-323.
- Stalder R. and Skogby H. (2003) Hydrogen diffusion in natural and synthetic orthopyroxene. *Phys. Chem. Minerals*, **30**:12-19.
- Stern C.R., Frey F.A., Futa K., Zartman R.E., Peng Z. and Kurtis Kyser T. (1990) Trace-element and Sr, Nd, Pb, and O isotopic composition of Pliocene and Quaternary alkali basalts of Patagonia Plateau lavas of southernmost South America. *Contrib. Mineral. Petrol.*, **104**:294-308.
- Stern C.R., Saul S., Skewes M.A. and Futa K. (1989) Garnet peridotite xenoliths from the Pali-aike alkali basalts of southernmost South America. In: 14 GSoASP Kimberlites and Related Rocks, Blackwell, Carlton, Australia: pp 735-744.
- Stern C.R., Kilian R., Olker B., Hauri E.H. and Kurtis Kyser T. (1999) Evidence from mantle xenoliths for relatively thin (<100 km) continental lithosphere below the Phanerozoic crust of southernmost South America. *Lithos*, **48**:217-235.
- Stolper E. and Newman S. (1994) The role of water in the petrogenesis of Mariana Trough magmas. *Earth Planet. Sci. Lett.* **121**, 293-325.
- Stocker R.L. (1978) point defect formation parameters in olivine. *Phys. Earth Planet. Inter.* **17**:108-117.
- Sykes D., Rossman G.R., Veblen D.R. and Grew E.S. (1994) Enhanced H and F incorporation in borian olivine. *Am. Mineral.*, **79**:904-908.
- Thompson A.B. (1992) Water in the Earth's upper mantle. *Nature*, **358**:295-302.
- Tsai T.-L. and Dieckmann R. (1997) Point defect and transport of matter and charge in olivines  $(\text{Fe}_x\text{Mg}_{1-x})_2\text{SiO}_4$ . *Mat. Sci. Forums Vols.*, **239**:399-402.

- Tsai T.-L. and Dieckmann R. (2002) Variation of oxygen content and point defects in olivines,  $(\text{Fe}_x\text{Mg}_{1-x})_2\text{SiO}_4$ ,  $0.2 < x < 1.0$ . *Phys. Chem. Minerals*, **29**:680-694.
- Vocadlo L. N. (1993) The role of lattice dynamics in determining the Grüneisen parameter and diffusion processes in minerals and their analogues, Ph.D thesis, University College London: pp 202.
- Wanamaker B.J. and Duba A. (1993) Electrical conductivity of San Carlos olivine along [001] under oxygen-and pyroxene-buffered conditions and implications for defect equilibria. *J. Geophys. Res.*, **98**:489-500.
- Wang L., Zhang Y. and Essene E.J. (1996) Diffusion of the hydrous component in pyrope. *Am. Mineral.* **81**:706-718.
- Wang Z. and Li S. (1999) Hydrogen-enhanced electrical conductivity of diopside crystals. *Geophys. Res. Lett.*, **26**:799-802.
- Walker A.M., Wright K. and Slater B. (2003) A computational study of oxygen diffusion in olivine. *Phys. Chem. Minerals*, **30**:356-545.
- Wilkins R.W.T. and Sabine W. (1973) Water content of some nominally anhydrous silicates. *Am. Mineral.*, **58**:508-516.
- Williams D.W. (1968) Improved cold seal pressure vessels to operate at 1100°C at 3 kilobars. *Am. Mineral.*, **53**:1765-1769.
- Williams Q. and Hemley R. (2001) Hydrogen in the deep Earth. *Annu. Rev. Planet. Sci.*, **29**:365-418.
- Withers A.C, Wood B.J and Carroll M.R. (1998) The OH content of pyrope at high pressure. *Chemical Geol.*, **147**: 161-171.
- Wood B. J. (1995) The effect of H<sub>2</sub>O on the 140-kilometer seismic discontinuity. *Science* **268**: 74-76.
- Wright K. and Catlow C.R.A. (1996) Calculations on the energetics of water dissolution in wadsleyite. *Phys. Chem. Minerals*, **23**:38-41.
- Xia Q., Chen D., Carpenter S., Zhi X., Wang R. and Cheng H. (2000) Hydrogen diffusion in clinopyroxene: dehydration experiments. *Science in China*, **43**:561-568.
- Xu Y., Poe B.T., Shankland T.J. and Rubie D.C. (1998) Electrical conductivity of olivine, wadsleyite and ringwoodite under upper-mantle conditions. *Science*, **280**:1415-1418.
- Xu Y., Shankland T. J. and Duba A.G. (2000) Pressure effect on electrical conductivity of mantle olivine. *Phys. Earth Planet. Inter.* **118**:149-161.

Zhao Y.-H., Ginsberg S. and Kohlstedt D. (2001) Experimental investigation on water solubility in olivine single crystal with different Fe content. *Contrib. Mineral. Petrol.*, **147(2)**, 155-161.

# Appendix

## Appendix 1: Kröger-Vink notation used for point defects

In this thesis, the Kröger-Vink notation is used to describe point defects (Kröger F. A. and Vink H. J. (1956) *Solid State Physics, Volume 3, p. 307*). The basics of the notation is outlined below:

**The symbol is the name of the species.**

*i.e.*

- a silicon atom is written as Si,
- a vacant site V (*nota*: V is not vanadium).
- an interstitial is denoted by the subscript “i”. Thus a silicon interstitial would be written Si<sub>i</sub>.

**The site occupancy of the species is written as the subscript.**

*i.e.*

- a silicon in a silicon site is written Si<sub>Si</sub>,
- an iron in a silicon site as Fe<sub>Si</sub>,
- and a vacant silicon site V<sub>Si</sub>.

**The net excess charge on the site is written in the superscript**

*as*

- No excess charge on a site is indicated by an x
- One excess plus charge on a site is indicated by a •
- One excess minus charge on a site is indicated by a ‘

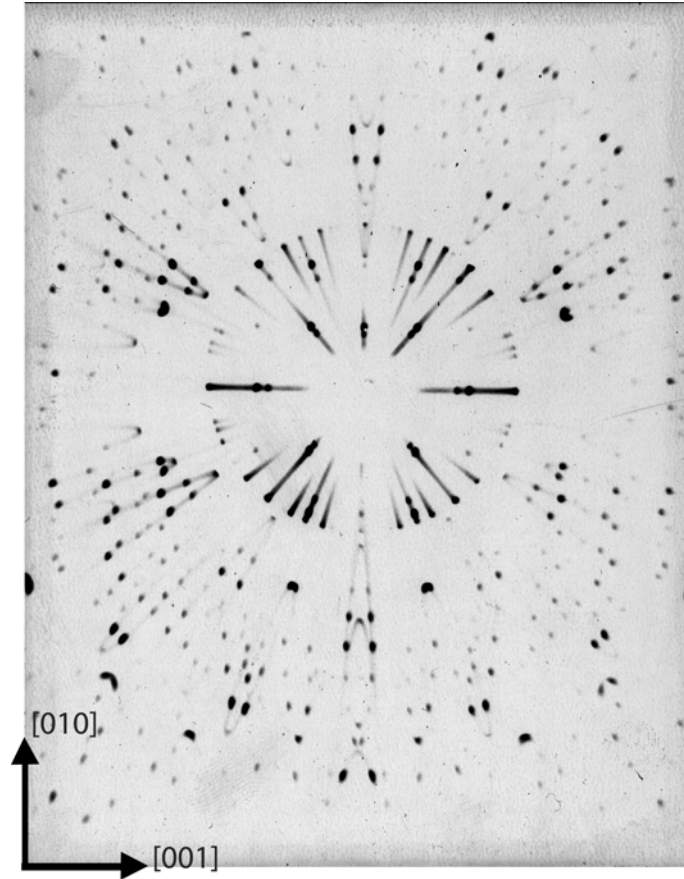
The reason for this notation instead of +, -, and 0 is that these are charges on sites and reflect the balance of the charge of the atom and the charge required by the site. An interstitial will always have the same charge as the atom.

- $\text{Si}_i^{\bullet\bullet\bullet}$ , is an interstitial silicon (4+) atom.
- $\text{Al}'_{\text{Si}}$ , is an aluminum (3+) atom in an silicon (4+) site. There is a net charge of (-1) on the site.
- $\text{V}_O^{\bullet\bullet}$ , is an vacant oxygen site, then the charge on the site is (+2).
- $\text{Fe}^{\bullet}_{\text{Mg}}$ , is a ferric iron ( $\text{Fe}^{3+}$ ) in a magnesium site.
- $\text{Fe}^x_{\text{Mg}}$ , is a ferrous iron ( $\text{Fe}^{2+}$ ) in a magnesium site.

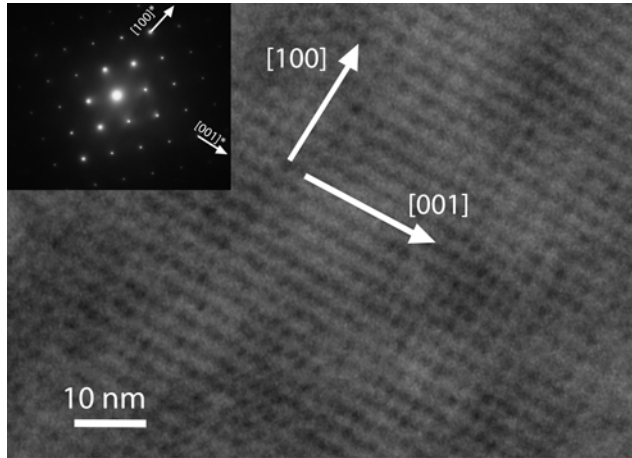
Afterwards, the rules to write point defect equations are relatively simple:

1. Charge conservation - electroneutrality: the total charge on the left side of the equation must be the same as on the right side of the equation.
2. Conservation of atomic species: there must be the same number of each atomic species on the left side and right side of the reaction.
3. Conservation of atomic sites: this is the most difficult aspect, there must be the same number of atomic sites on both sides of the equation so that sites are not created or destroyed.

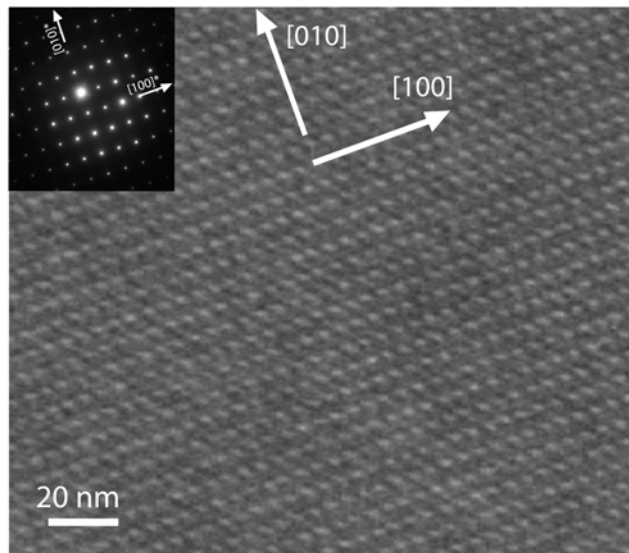
**Appendix 2: X-ray diffraction patterns of forsterite single crystal, taken using a precession camera and Mo K $\alpha$  radiation (with the help of F. Bromiley).**



### Appendix 3: TEM documentation



TEM high-resolution picture of forsterite Fo 2-10.



TEM high-resolution picture of olivine PA-5.

# Appendix 4: Gulp results

Defect	O position			H position			O-H distance (Angstrom)	E (eV)	Ec (eV)	frequency (cm-1)	Reaction $\Delta E(eV)$	OH vector polarization (Angstrom)		
	x	y	z	x	y	z						x	y	z
(OH1) involving O1, position 1	-0.00023	2.847565	1.947718	-0.000141	2.847673	2.933271	0.9856	8.48	15.53	3848	0.000118	0.000108	0.965553	
(OH1) involving O1, position 2	0.142524	8.543006	6.65163	0.975184	8.542919	7.229221	1.0134	9.1	16.15	3715	0.83266	0.000087	0.577591	
(OH1) involving O2	0.175075	2.84766	5.90758	1.126286	2.847685	6.180785	0.9897	10.26	17.31	3903	0.951211	0.000025	0.273205	
(OH2) involving O3, position 1	0.000059	11.29527	2.308633	0.000977	11.99678	2.997337	0.9831	10.09	17.14	3910	0.000918	0.701507	0.668704	
(OH2) involving O3, position 2	0.120023	11.13693	2.127125	0.969315	10.97469	1.661761	0.9819	9.82	16.87	3658	0.849292	0.162236	0.465364	
(OH2) involving O4	1.62308	1.599927	8.234321	1.714084	2.398131	8.706679	0.9925	9.69	16.74	3753	0.090476	0.868204	0.472358	
specific position: O1a-H...O1b	2.825785	8.543084	6.084868	2.9836	8.543146	7.070474	0.986	8.49	15.54	3843	0.027815	0.0000621	0.985606	
specific position: O1a...H-O3	-0.000027	8.543082	6.327009	0.000207	8.543052	5.341424	0.9856	8.49	15.54	3842	0.000234	0.00003	0.985585	
specific position: O1-H...O3	2.968343	8.543007	5.71649	3.801208	8.542647	5.71649	0.9856	9.1	15.54	3715	0.832865	0.00036	0	
specific position: O1-H...O4	2.945821	5.441593	6.264266	3.794706	5.278667	5.798461	0.9819	9.82	16.87	3958	0.848885	0.162926	0.465805	
specific position: O1-H...O4	2.825749	8.543084	6.084908	2.825711	8.543032	7.070473	0.9856	8.49	15.54	3843	0.000038	0.000052	0.985565	
specific position: O1...H-O4	1.6238	9.860732	8.315033	1.714467	8.992455	7.842902	0.9925	9.7	16.75	3753	0.0906689	0.868277	0.472131	
specific position: O3a-H...O3b	2.945752	5.441507	6.264382	3.795225	5.279748	5.7991	0.982	9.82	16.87	3957	0.849473	0.161759	0.465282	
specific position: O3a...H-O3b	5.531507	5.441498	6.147459	4.682241	5.279303	6.612897	0.9819	9.82	16.87	3957	0.849286	0.162195	0.465438	
(Mg3, OH) with O1a-H...O1b	2.862679	8.52165	5.868492	3.595224	9.107156	6.193463	0.9925	30.93	37.98	3728	0.732545	0.585506	0.324971	
(Mg3, OH) with O1a...H-O1b	-0.036945	8.521663	6.543449	-0.76929	9.107188	6.218969	0.9922	30.93	37.98	3729	0.732345	0.585525	0.32448	
(Mg3, OH) with O1-H...O3	2.862697	8.521643	5.868477	3.595358	9.10724	6.193287	0.9926	30.93	37.98	3727	0.732661	0.585597	0.32481	
(Mg3, OH) with O1...H-O3	2.929691	5.480634	6.33985	3.754518	6.042588	6.334075	0.9981	32.29	39.34	3698	0.824827	0.561954	0.005775	
(Mg3, OH) with O1-H...O4	2.862708	8.521642	5.868533	3.595318	9.167161	6.19334	1.029	30.93	37.98	3728	0.73261	0.645519	0.324807	
(Mg3, OH) with O1...H-O4	1.628577	9.860952	8.346459	1.724908	8.98638	7.8859	0.9931	33.49	40.54	3735	0.096331	0.874572	0.460559	
(Mg3, OH) with O3a-H...O3b	2.92968	5.480681	6.339901	3.754226	6.043073	6.334487	0.9981	32.29	39.34	3698	0.824546	0.562392	0.005414	
(Mg3, OH) with O3a...H-O3b	5.547558	5.480668	6.072	4.722807	6.042713	6.077695	0.9902	32.29	39.34	3698	0.728453	0.568202	0.356224	
(Mg3, OH) involving O1a and O1b	0.038424	8.517064	6.534485	0.766877	9.085266	6.178245	0.9902	39.72	53.82	3735	0.848489	0.020148	0.026426	
(Mg3, OH) involving O1a and O3	2.710682	1.106936	6.338875	1.862193	11.08951	6.312449	0.8491	39.72	53.82	3735	0.728371	0.577194	0.356383	
(Mg3, OH) involving O4a and O4b	0.039416	2.812648	1.740122	0.766787	3.389842	2.096505	0.9953	39.07	53.17	3768	0.84843	0.519967	0.02629	
(Mg3, OH) involving O3 and O1a	2.710702	5.913839	1.93565	1.862212	5.393906	1.961987	0.9954	40.33	54.43	3735	0.00388	0.255382	0.961533	
(Mg3, OH) involving O3 and O1a	1.591999	4.277951	-0.074201	1.603524	4.021932	0.887131	0.9948	40.33	54.43	3732	0.004025	0.256019	0.961332	
(Mg3, OH) involving O3 and O1a	0.038384	2.821651	1.740211	0.766521	3.389704	2.097082	0.9901	39.07	53.17	3769	0.728137	0.568053	0.356871	
(Mg3, OH) involving O3 and O1a	2.710702	5.913839	1.93565	1.862212	5.393906	1.961987	0.9954	39.07	53.17	3735	0.84849	0.519854	0.026426	
(Mg3, OH) involving O3 and O1a	1.591195	1.25965	-0.147982	0.994978	0.452258	-0.154604	1.0037	31.67	38.72	3708	0.596217	0.8007392	0.006622	
(Mg3, OH) involving O3 and O1a	1.234618	6.948423	3.989389	1.830863	6.147725	3.982743	0.9983	31.67	38.72	3708	0.596245	0.800698	0.006646	
(Mg3, OH) involving O3 and O1a	4.41694	4.442386	4.285209	3.820811	5.243226	4.291885	0.9984	31.67	38.72	3708	0.596129	0.80084	0.006676	
(Mg3, OH) involving O3 and O1a	1.234562	4.442405	4.285199	1.830848	5.243044	4.291904	0.9983	31.67	38.72	3708	0.596286	0.800639	0.006705	
(Mg3, OH) involving O3, position 1	2.86564	5.985124	1.998936	2.824818	6.606767	2.99302	1.1732	31.84	38.89	3699	0.040822	0.6216429	0.994084	
(Mg3, OH) involving O3, position 2	2.825915	5.405558	6.2756	2.826751	5.322862	5.281618	0.9974	31.84	38.89	3701	0.000836	0.082696	0.993982	

Note: E = defect energy; Ec = corrected energy; defect energy + energy of bonding between O and H for i number of hydrogen present in the defect, which is equal to Ec=(E + (i x 7.05)) in eV.

# Appendix 4: Gulp results

Defect	O position			H position			O-H distance (Angstrom)		E(eV)	Eg(eV)	frequency (cm <sup>-1</sup> )	OH vector polarization (Angstrom)		
	X	Y	Z	X	Y	Z	ΔE(eV)	X				Y	Z	
[VMG1, 2(OH)] involving both O4 in the median plan and // to [100]	1.23332	6.945512	3.991165	1.804683	6.130294	3.98158	0.9956	39.54	53.64	3761	-1.59	0.571363	0.815218	0.009585
[VMG1, 2(OH)] involving both O4 in the median plan	4.41817	4.445244	4.28342	3.846784	5.260476	4.293124	0.9956	37.40	53.64	3740	-1.59	0.571386	0.815232	0.009704
[VMG1, 2(OH)] involving both O4 in the median plan and // to [010]	4.18129	6.945534	3.991146	3.846846	6.130288	3.981579	0.9955	39.54	53.64	3761	-1.59	0.571283	0.815266	0.009567
[VMG1, 2(OH)] pointing to O3	1.233369	4.445241	4.28342	1.804546	5.260609	4.292786	0.9956	37.40	53.64	3740	-1.59	0.571177	0.815368	0.009366
[VMG1, 2(OH)] pointing to O3	1.233323	4.445297	4.283516	1.804503	5.260652	4.292726	0.9957	39.54	53.64	3760	-1.59	0.571182	0.815385	0.009221
[VMG1, 2(OH)] pointing to O3	4.41824	6.94549	3.991232	3.847558	6.129663	3.982715	0.9957	37.40	53.64	3740	-1.59	0.570882	0.815827	0.008517
[VMG1, 2(OH)] pointing to O3	4.441817	4.445281	4.283391	3.847107	5.260721	4.292496	1.0093	39.54	53.64	3761	-1.59	0.571285	0.815323	0.009417
[VMG1, 2(OH)] pointing to both O3 and // to [001]	2.82568	4.404817	6.266601	2.825255	5.311113	5.27566	1.3429	39.81	53.91	3722	-1.33	0.000425	0.906296	0.990941
[VMG1, 2(OH)] pointing to both O3 and // to [001]	2.825841	5.985927	2.007959	2.826265	6.079444	2.99897	0.9954	39.54	53.64	3742	-1.59	0.000424	0.093517	0.991011
[VMG1, 2(OH)] pointing to both O3 and // to [001]	1.233451	6.945559	3.991183	1.804366	6.130309	3.982123	0.9955	39.54	53.64	3761	-1.59	0.570915	0.815469	0.009066
[VMG1, 2(OH)] pointing to both O3 and // to [001]	4.418052	4.445202	4.283452	3.846476	5.260553	4.292883	1.3163	32.73	39.78	3741	-0.9	1.033377	0.815351	0.009431
[VMG1, 2(OH)] pointing to both O3 and // to [001]	1.240999	1.475062	4.201029	1.784558	2.317198	4.1576	1.0039	32.73	39.78	3626	-0.9	0.543861	0.842132	0.035353
[VMG1, 2(OH)] pointing to both O3 and // to [001]	4.410506	4.22038	4.21112	3.866845	3.378248	4.15759	1.0039	32.73	39.78	3626	-0.9	0.543861	0.842132	0.035353
[VMG2, (OH)] involving O4	2.825977	2.847691	6.5127	2.826822	2.847754	5.511763	1.0009	33.37	40.42	3671	-0.26	0.000845	0.000063	1.000937
[VMG2, (OH)] involving O4	2.825835	2.847722	2.48166	2.826722	2.847646	3.476365	0.9947	31.16	38.21	3751	-2.47	0.000887	0.000076	0.994715
[VMG2, (OH)] involving O4	4.412958	4.215174	4.201999	3.888776	3.362925	4.155345	1.0016	40.61	54.71	3662	-1.51	0.524182	0.852249	0.046654
[VMG2, 2(OH)] involving both O4 in the median plan and // to [100]	1.238562	1.480232	4.20197	1.762668	2.332506	4.155167	1.0016	40.61	54.71	3645	-1.51	0.524106	0.852274	0.046803
[VMG2, 2(OH)] pointing to O2 and O1 and // to [001]	2.825434	2.847648	2.465199	2.823195	2.84817	3.452941	0.9877	39.73	53.83	3833	-2.39	0.002239	0.000522	0.987742
[VMG2, 2(OH)] pointing to O2 and O1 and // to [001]	0.00075	8.782646	2.311083	0.00021	7.85685	2.717051	0.9961	108.4	115.45	3743	-3.06	0.015426	0.000015	0.996028
[VMG2, 2(OH)] pointing to O2 and O1 and // to [001]	1.555479	7.08585	4.242662	0.7068	7.068734	3.727577	0.9777	105.75	112.8	3983	-5.72	0.00054	0.925796	0.405968
[VMG2, 2(OH)] pointing to O2 and O1 and // to [001]	-1.558497	7.08589	4.242652	-0.706744	7.06889	3.727682	0.9955	106	113.05	3711	-5.46	0.851679	0.017116	0.515085
[VMG2, 2(OH)] involving O4b	-1.581889	7.07293	4.208578	-0.874859	7.007184	3.523441	0.9867	109.77	123.87	3860	-10.17	0.70701	0.065674	0.688137
[VMG2, 2(OH)] involving O4 and O4b	-1.581769	7.072969	4.208509	0.87545	7.007859	3.522685	0.9867	109.73	123.83	3809	-10.21	0.706319	0.06511	0.688824
[VMG2, 2(OH)] involving O4 and O4b	-0.032499	5.482636	1.881549	-0.20516	6.239575	2.490891	0.9869	109.73	123.83	3833	-10.21	0.172661	0.756939	0.609342
[VMG2, 2(OH)] involving O4 and O4b	1.539769	7.100128	4.263696	0.633577	7.216068	3.882995	0.9897	109.77	123.87	3778	-10.17	0.906192	0.11594	0.380701
[VMG2, 2(OH)] involving O4 and O4b	-0.00146	5.466469	1.889307	-0.000693	6.141166	2.610372	0.9875	112.06	126.16	3823	-7.89	0.000547	0.674697	0.721065
[VMG2, 2(OH)] involving O2 and O3	0.001683	8.796667	2.319166	0.004703	7.926057	2.818405	1.0036	127.2	148.35	3560	-1.23	0.03032	0.87061	0.499239
[VMG2, 2(OH)] involving O2 and O3	-1.213887	7.086096	4.332942	-0.221838	7.338894	4.294759	1.0244	127.2	148.35	3654	-1.23	0.992019	0.252498	0.038183
[VMG2, 2(OH)] involving O2 and O3	0.217886	8.809453	2.32189	0.460212	7.946865	2.792682	1.0122	114.41	135.56	3654	-14.02	0.667717	0.563858	0.500228
[VMG2, 2(OH)] involving O2 and O3	0.79071	7.220757	4.089693	0.122993	6.656899	3.589465	1.007	114.41	135.56	4427	-14.02	0.667717	0.563858	0.500228
[VMG2, 2(OH)] involving O2 and O3	-1.575726	7.126948	4.207704	-0.848676	7.395642	3.612242	0.9774	114.41	135.56	4033	-14.02	0.992019	0.252498	0.038183
[VMG2, 2(OH)] involving O2 and O3	-0.00085	5.481347	1.862164	-0.000778	6.311697	2.372446	0.9746	114.41	135.56	4975	-14.02	0.000693	0.83035	0.510282
[VMG2, 2(OH)] involving O2 and O3	1.575808	7.126911	4.207704	0.849075	7.395382	3.611653	0.9775	114.41	135.56	3939	-12.02	0.726733	0.268471	0.596051
[VMG2, 2(OH)] involving O2 and O3	-1.543734	8.099585	4.27581	-0.60372	7.119416	3.98818	0.9831	114.41	135.56	3708	-12.02	0.94002	0.101831	0.287633
[VMG2, 2(OH)] involving O2, O4a and O3	0.144483	8.801252	2.305405	0.510836	7.973874	2.725739	0.9877	116.41	137.56	3708	-12.02	0.386353	0.827378	0.420334
[VMG2, 2(OH)] involving O2, O4a and O3	0.042796	5.473319	1.896815	0.266589	6.145537	2.576905	0.9821	116.41	137.56	3907	-12.02	0.223793	0.672318	0.68009
[VMG2, 2(OH)] involving O2, O4b and O3	0.04288	5.473338	1.896817	-0.266595	6.145538	2.57691	1.0051	116.41	137.56	3708	-12.02	0.309475	0.672315	0.680093
[VMG2, 2(OH)] involving O2, O4b and O3	-0.144479	8.801278	2.30541	-0.510834	7.9739	2.725741	0.9977	116.41	137.56	3864	-12.02	0.386355	0.827378	0.420331
[VMG2, 2(OH)] involving O2, O4b and O3	1.545738	7.099595	4.275803	0.603723	7.110447	3.98816	0.9831	144.34	172.54	3907	7.43	0.940015	0.101882	0.287633
[VMG2, 2(OH)] involving O2, O4b and O3	1.188669	5.670226	2.092565	0.902248	5.957078	2.694885	0.726	144.34	172.54	3120	7.43	0.286421	0.101882	0.602232
[VMG2, 2(OH)] involving O2, O4b and O3	-0.078329	8.723908	2.416537	-0.625283	7.963656	2.866387	1.039	144.34	172.54	3486	7.43	0.546954	0.760282	0.44985
[VMG2, 2(OH)] involving O2, O4b and O3	1.399325	6.991947	3.842086	0.752317	7.532249	3.282214	1.0119	144.34	172.54	3883	7.43	0.647008	0.540302	0.559872
[VMG2, 2(OH)] involving O2, O4b and O3	-1.518003	7.091374	4.236267	-0.695729	6.756754	3.83044	0.9761	144.34	172.54	3974	7.43	0.822274	0.333462	0.405827

Nota: E = defect energy; Ec = corrected energy; defect energy + energy of bonding between O and H for i number of hydrogen present in the defect, which is equal to Ec = (E + (i x 7.05)) in eV.

# Erklärung

Hiermit erkläre ich, dass ich die vorliegende Arbeit selbständig verfasst und keine anderen als die von mir angegebenen Quellen und Hilfsmittel benutzt habe.

Ferner erkläre ich, dass ich nicht anderweitig versucht habe, mit oder ohne Erfolg, eine Dissertation einzureichen und auch keine gleichartige Doktorprüfung an einer anderen Hochschule endgültig nicht bestanden habe.

Bayreuth, im Juni 2004

Sylvie Demouchy



